ABSTRACT

**DNA-Origami Templated Formation of Liposomes and Related Structures**

Jing Wang

2014

We have developed novel techniques for manufacturing vesicles with predefined attachments to scaffolds of DNA, and have studied the underlying mechanism(s) of this DNA directed vesicle formation by capturing intermediates. These DNA scaffolds are self-assembled by the origami method, which can use DNA as a programmable building block to form diverse structures: two-dimensional crystals, nanotubes, and three-dimensional wireframe nanopolyhedra [1-5].

Nano-templated vesicles are prepared using rigid rings of bundled DNA. Single phosphatidyl ethanolamine (PE) lipids are coupled to these rings first by covalent conjugation with an oligonucleotide (oligo) "anti-handle", then by that oligo's sequence-specific hybridization to one of several (0, 1, 2, ..., 16) single-stranded "handles" on the DNA ring, designed to protrude from its interior. Vesicles are then formed in a solution of these ring complexes, excess phospholipid and detergent as the detergent is dialyzed away over several hours. Micelles preferentially nucleate around the alkyl chain of each PE inside the ring, and their growth during dialysis determines the volume of lipid in the final structures formed. Ring-PE lipid-

vesicles bear exactly one ring per vesicle in characteristic transmission electron micrographs, with a size close to the inner diameter of its ring template.

Chapter 1 provides an overview of the significance and roles of engineering membranes in vitro. Biological membranes are incredibly complex, which in turn makes studying structure and function of membrane protein difficult in the absence of an artificial bilayer. Even more so, current limitations of producing high quality liposomes with reproducible techniques are placing more strain on elucidating the mechanisms of reconstitution. However, the emergence of the field of DNA Origami in 2006 truly revolutionized the limitless abilities to create 2D and 3D structures with function. We took advantage of this field by developing geometries to facilitate membrane growth.

Chapter 2 reports a new method for templating vesicles with a uniform size and shape using DNA origami rings bearing inner handles facing 0° to the center. DNA origami rings of varying diameters can be designed with functional handles for templating the "Saturn" structure. Once the method was established, rings of varying handle angles were synthesized to determine their effects on the final vesicle structures.

Chapter 3 explores the parameters that affect the quantity of lipids assembling inside the template. These include ultracentrifugation time, detergent to lipid ratio, and dialysis conditions. In order to elucidate the mechanism of formation of our final templated structures, we performed mechanistic studies on 60-nm rings, systematically varying the initial number of lipid molecules anchored inside each ring. The capture of crucial intermediates: circular thin lipidic membrane, lipid bilayer torus, continuous outer bilayer, and seeded small unilamellar vesicles helped us understand how the vesicles are formed.

Chapter 4 summarizes the main results of the thesis and provides future prospectives on the potential expansion of DNA origami technology. A handful of new opportunities are presented based on control in the organization of DNA materials. Taking advantage of this machinery and applying it to the central problems in engineering, biology, chemistry, physics, and medicine will allow the field to elevate to the next level with promises of becoming a vital area of research.

# DNA-Origami Templated Formation of Liposomes and Related Structures

A Dissertation

Presented to the Faculty of the Graduate School

of

Yale University

In Candidacy for the Degree of

Doctor of Philosophy

By

Jing Wang

Dissertation Director: James Rothman

December 2014

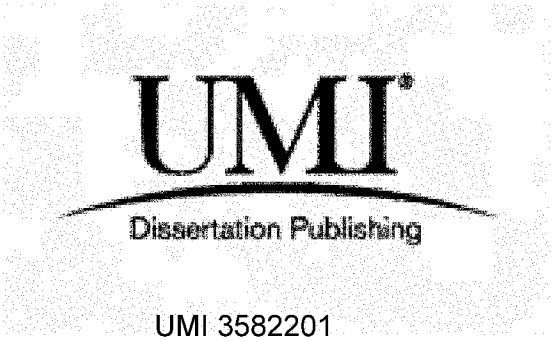





ProQuest LLC
789 East Eisenhower Parkway
P.O. Box 1346
Ann Arbor, MI 48106-1346

**Acknowledgements**

I would first like to thank my Ph.D thesis advisor, Professor James Rothman, for his support and mentorship during the five years I have been in his laboratory. He has inspired me to look at science in a completely different light. Never would I have imagined a more perfect thesis project in the field of chemical biology as that presented here. And so much of it is because of Dr. Rothman's brilliant mind. The freedom of ideas and exchange of knowledge in his wonderful lab has given me the passion and love for my project. I would also like to thank Professor Chenxiang Lin for his hands on involvement in the lab and his brilliant guidance during the course of this project. Furthermore, I would like to thank Professor Alanna Schepartz and Professor Elsa Yan for their science and career related advice and guidance. The contributions of my committee members have inspired me bring my project to unimaginable territories.

I am grateful to the members of the Rothman laboratory, who have been amazing teachers in my graduate studies. Dr. Weiming Xu has taught me valuable skills in the lab and challenged me to think analytically and critically. Dr. Yang Yang has been an amazing collaborator who has participated in scholarly conversations, which in turn has helped us understand the project in a new light. Additionally, I am fortunate to have been graced with the talents and intelligence of Dr. Frederic Pincet, who have

contributed to my development as a graduate student when I first joined the lab. And I will always owe many thanks to the members of the Rothman Biophysics subgroup: Dr. Shyam Krishnakumar, Dr. Jeff Coleman, Dr. Feng Li, Dr. Oscar Bello, Dr. Sarah Auclair, Dr. Ouardane Jouannot, Dr. Jie Zhu, and past members. The lab would not exist without the hard work of Iris Douglas, Willa Bellamy, Pat Sullivan, Leslie Gourlay, and Jen Armstrong, whom I am very grateful to.

Graduate school became more complete with the life long friends I made here at Yale and for that I feel so blessed to have met Pam, Miho, Kyle, Chris, Andrew, Christina, Curren, Yifei, and Freddy. But most importantly, I would like to thank my boyfriend of 6 years, who has been by my side before we even moved to Yale. Michael made a huge commitment to my Ph.D thesis by providing the love and support during my toughest times and sharing in the happiest and most rewarding times. And for that, when I think of my successful accomplishments at Yale, he will always be a huge part of that memory.

Last but not least, I would like to thank my family for their unprecedented dedication and constant support. The goal of my parents has always been to provide my siblings and I with the best education possible throughout our lives. And they would never allow me to settle on second best. My father is the inspiration for my science career and the knowledge he

has taught and his guidance is beyond words. He will always be the one I look up to and admire the most.

**Contents:**

**Figures and Tables:**

## Chapter 1 - Introduction:

The biological membrane plays critical roles in mediating the cellular processes and functions. Cell membranes are tremendously complex with anchored proteins that control the transport of matter (chemicals and energy) with the extracellular environment or within the cytosol. In general, cells are enclosed within a membrane composed of phospholipids that isolates its internal behaving from the outside environment. This protective cell membrane contains a variety of components, including phospholipids, proteins, and macromolecules (i.e. sugars). The phospholipids are comprised of a hydrophilic head group and two hydrophobic alkyl chains. These amphiphilic lipids can assemble into two-dimensional (2D) sheets called a bilayer, which is measured to be 5 nm in thickness. This arrangement allows the hydrophobic tails to pack in a manner that separates them from the surrounding aqueous atmosphere.

Inside cells, the membrane coats define compartmental organization, formation, and fusion of organelles and thus are critical in the cellular processes. The principal model illustrates the budding of a vesicle containing cargo from one compartment to the fusion of that same vesicle with membrane of the target compartment with release of the delivered cargo. One biological example is the import of genomes in viruses into cells. Another example is the membrane fusion of sperm and egg cells so

fertilization occurs. Intermolecular coiled-coil fusion proteins initiate these fusion processes by bringing two membranes into close proximity [6, 7]. As a result of that, the lipids in proximity are disrupted and a fusion pore appears that results in fusion of the membranes [8].

The liposomes have been used extensively in vitro in studying the formation and fusion of intracellular vesicles. Thus, in the following sections, we will review the mechanism of vesicle fusion and the formation and application of liposomes.

### 1.1- Lipid Bilayer Fusion Models:

In general, the membrane fusion can be classified into two major categories: 1) the lipid bilayer fusion without the involvement of proteins or protein-free lipid bilayer fusion, and 2) the lipid bilayer fusion facilitated by proteins [8, 9]. The process of protein free lipid bilayer fusion requires the formation of two crucial intermediates: hemifusion structures and fusion pores [10-12]. Based on the types of proteins involved, the protein facilitated lipid bilayer fusion can be further sorted into three subclasses: 1) the SNARE (soluble NSF-attachment protein receptor) facilitated lipid bilayer fusion, 2) the protein trans-membrane domain facilitated lipid bilayer fusion, and 3) the viral fusion protein facilitated lipid bilayer fusion [9]. This study is to investigate the roles of the DNA origami ring structure in templating vesicle

formation in a protein-free system, and we will next describe the protein free lipid bilayer fusion in detail.

### *1.1 a - Protein Free Lipid Bilayer Fusion*

The protein free lipid bilayer fusion is mediated by two crucial intermediates: hemifusion structures and fusion pores. As shown in figure 1.1, the hemifusion intermediate can be seen with mixing of outer leaflets of two opposing membranes while the inner leaflets remain intact. Here, the strictly lipid mixing occurs without content mixing of vesicles. If further lipid mixing takes place, it will lead to the opening of a fusion pore. Otherwise two distinct membranes will be formed again [11, 13]. When a fusion pore is formed, both the outer and inner leaflets of the membrane are disrupted and content previously protected by the two apposing membranes is transferred. Further, the pore can be closed and lipid polar heads surrounds the pore edge. These processes have been shown by electrophysiological experiments and by fluorescence assays [13, 14].

The formation of hemifusion structures and fusion pores is dependent on the lipid composition of lipid bilayers in the absence of proteins [10]. The effective spontaneous curvature of a lipid is highly defined by its molecular

structure and behavior among other lipids in a monolayer, and affects directly the creation of various fusion intermediates. Figure 1.1 shows positive, negative, and zero effective curvatures of various lipids. Lysophosphatidylcholine (LPC) and polyphosphoinositides both are capable of forming curved monolayers whose surface bends in the direction of polar heads resulting in a positive effective spontaneous curvature. These structures tend to have an effective shape of an inverted cone. Another type of lipids is unsaturated phosphatidylethanolamine and diacylglycerol, which bends in the direction of the hydrocarbon chains. These cone-like shapes have a negative effective spontaneous curvature. The last structure is demonstrated by phosphatidylcholine as it forms flat monolayers with a cylindrical shape showing almost zero spontaneous curvature [10].

The effective spontaneous curvature and the close inter bilayer contact determine whether two apposed membranes will fuse. Positive and negative curvature can either promote or inhibit formation of an intermediate as both already supports bending to a certain curvature. The cone-shaped PE tends to promote hemifusion indicating that intermediates with negative curvature are required. However, the inverted cone LPC promotes formation of a fusion pore indicating that a net positive curvature is seen along the pore edge [10]. The close inter-bilayer contact of less than 1 nm will promote two membranes to fuse spontaneously. If two membranes are not close enough, direct dehydration can be used to bring the membranes

together [15]. In addition, previous study has also shown that smaller vesicles are more fusogenic [16]. Further, membrane tension plays a large role in accelerating fusion intermediates and pushing hemifusion to full fusion with the opening of a fusion pore [8, 14, 17]

*1.1 b - Protein Facilitated Lipid Bilayer Fusion*:

As discussed above, the close inter-bilayer contact between two membranes is required for fusion. Charged bilayers will always create electrostatic repulsion, and thus in the intracellular compartment, the distances between biological membranes never surpass 10-20 nm. The universal machinery in the cell that brings membranes into close proximity and that drives fusion is the SNARE and SM (Sec1/Munc18) proteins. The first hints of SNAREs mediating membrane fusion came from the finding that two powerful SNAREs-targeted neurotoxins, botulinum and tetanus toxins, block presynaptic membrane fusion. In 1992, tetanus toxin and a few botulinum toxins were found to cleave synaptobrevin/VAMP (vesicle-associated membrane protein), the first of the SNARE proteins [18, 19]. Later, other botulinum toxins were found to cleave at different positions on the SNAP-25 and syntaxin-1 [20, 21]. Studies in the field further suggested that *Caenorhabditis elegans* homologs of these proteins are crucial for the nervous system function [22] and that yeast homologs of them are needed for membrane traffic in the secretory pathway [23].

NSF (N-ethylmaleimide sensitive factor) is a crucial component for membrane trafficking, and its function relies on adapter proteins called "SNAPs" (soluble NSF-attachment proteins) [24]. Rothman and colleagues made a miraculous discovery that synaptobrevin, SNAP-25, and syntaxin form a complex that is critical for fusion. NSF (ATPase, [25]) can break apart this complex, which helps to coin the term SNARE (soluble NSF-attachment protein receptor). This suggested that the *trans*-SNARE complexes could facilitate vesicle docking and targeting specificity during the vesicle and plasma membrane interaction. Since then, several discoveries about the SNARE complex were published. First, SNARE complexes are highly stable because they are tremendously resistant to SDS [26]. Second, the SNARE complex is composed of parallel helical regions of synaptobrevin and syntaxin-1, which are adjacent to the transmembrane region [27]. Third, NSF is not involved in fusion but participates upstream of fusion. The conclusion from these findings is SNARE complex formation (in parallel four-helix bundle) releases energy that in turn is used to bring membranes into close proximity for fusion [28l, 29, 30]. Only in the presence of SM protein partners, can SNAREs drive fusion during physiological conditions and the term "SNARE hypothesis" is coined.

Roles of SNAREs are illustrated in figure 1.2. In this process, first, SNAREs zipper from amino- to carboxyl-terminal to form the *trans*-SNAREs.

Complete zippering can result in placing stress on the membranes and SM proteins are involved in fusion-pore opening. During the opening, both apposed membranes merge fully and the SNARE complex is switched to its *cis*- form where the SNAREs are all on one membrane. Next NSF and SNAPs come into play and dissociates the SNAREs into its monomeric form. We have learned from this that association and dissociation drives fusion. NSF transfers energy to SNARE proteins and through ATP dependent dissociation, the energy of the SNAREs is then converted into use for fusion.

### 1.2 - Membrane Protein Reconstitution into Liposomes:

Most biological membranes are tremendously complex and can make studying the function and structure of membrane proteins difficult. However, the purified proteins from its native membrane can be reconstituted into an artificial membrane in which they are correctly inserted and oriented into a lipid bilayer. Thus, this reconstitution method is heavily implemented to characterize the mechanism of membrane protein in vectorial and transport function [31-33]. Further, through biochemical and biophysical techniques, lipid-protein and protein-protein interactions, and topological and topographical characteristics of various proteins can be studied. And finally, reconstitution has resulted in high-resolution structural information through electron crystallography [34, 35].

Four methods of membrane protein insertion has been made available in creating empty phospholipidic vesicles: 1) mechanical means, 2) freeze-thawing, 3) organic solvents, and 4) detergents [36]. However, techniques to successfully reconstitute membrane proteins were still lacking. Several parameters can affect the activity of the reconstituted protein, such as 1) homogeneity and correct final orientation, 2) morphology and size of the reconstituted proteoliposome, and 3) their residual permeability.

The limitation in this field includes techniques themselves. Sonication (a mechanical method) was frustrating because the use of local probe heating resulted in 1) degradation and denaturation of membrane proteins, and 2) the production of small vesicles (10-20 nm) that barely had enough room to hold ions and solutes of the membrane proteins. Organic solvents, used in solvent injection [37] and reverse phase evaporation [38] to prepare vesicles could denature many membrane proteins [39, 40]. Although detergent [31, 33] tends to obstruct the vesicle formation process, it is the most common method in the field. This is due to the fact that detergent is required to disintegrate the native protein structure of amphiphilic proteins and to maintain a non-denaturing atmosphere throughout purification [41].

Currently, the combination of excess phospholipids and adequate detergent has been used to co-micellize the purified proteins, and this process forms two intermediates: lipid-protein-detergent and lipid-detergent

molecules. Then over time, detergent removal will allow for formation of closed lipid bilayer vesicles with the protein reconstituted. Three models have been proposed to underlie the mechanisms of proteoliposome formation and efficiency of reconstitution. In the 1988, the Lasic's model was proposed [42]. In this model, micelle-micelle interactions occur when detergent is first removed, and then mixed disk-like structures are formed. Then, once they grow past a certain size, at a critical micelle size, bending proceeds and a resultant vesicle is formed after the bilayer is closed. Until detergent is removed the vesicle morphology and size will continuously change. Here, the detergent type will affect micelle size, morphology, and composition of the initial micelles, and the type of detergent and the removal rate will affect the various structures formed during the micelle-bilayer transition [43-45].

Two other opposing models were also elaborated in explaining the mechanism. In the one model, during dialysis, micelle mixtures of lipid-detergent and lipid-detergent-protein combine and the protein participates in liposome formation. In another model, during dialysis, the mixture of micelles dissociates and detergent inserted bilayers form, which then allows proteins to randomly insert. The type of detergents and detergent removal rate affect both models [31, 33, 46].

## 1.3 - The Methods of Detergent Removal

There are four methods of detergent removal: 1) dialysis, 2) gel filtration, 3) dilution, and 4) polystyrene beads. These have been used in our group and in this project. Among the four methods, dialysis is the most commonly used method in which a porous membrane removes the detergent monomers crude mixture of lipid-protein-detergent micelles yielding the purified vesicles and micelles. The typical size of the dialysis membrane pore is no larger than 14 kDa, and scaling down options of microdialysis can accommodate samples of 50 to 100 μL [34, 35]. In general, the higher the critical micelle concentration (CMC) of detergents, the faster they are to remove (1-2 days). Examples of high CMC detergents are octylglucoside, 3-[(cholamidopropyl)-dimethyl-ammonio]-1-propane sulfonate (CHAPS), and ionic detergents (i.e. sodium cholate). In the case of low CMC detergents such as polyoxyethylene glycols dialysis could take 1-2 weeks [47]. The advantages of this method include simplicity, low cost, and generally homogenously sized vesicles. The disadvantages are: irreproducibility, fluctuating rates of dialysis, and loss of products stuck to the dialysis membrane.

To reduce the dialysis time, particularly for low CMC detergent, methods with a flow through dialysis cell and polystyrene beads have been developed [48]. The former precisely monitors the rate of detergent removal

and lower experiment time [49] and the latter maintains constant the buffer environment while keeping the detergent concentration to zero. The two polystyrene beads currently used are: Amberlite XAD and Bio-Beads SM-2. Adding either one of those beads to the protein-lipid-detergent mixture is a great alternative to other methods of reconstitution [49-51]. Radioactive compounds can be used in measuring the adsorptive capacity of beads and rates of detergent removal. Other benefits include the precise control of the detergent removal rate by controlling the amount of beads used and complete removal of detergent resulting in proteoliposome formation with low ionic permeability. Thus, this technique is better than all the other detergent removal methods discussed and has been heavily used for reconstitution using a variety of detergent types [33, 49].

Other two methods, gel filtration and dilution, have been also used to remove the detergents. Gel filtration takes the advantage of the fact that micelles and liposomes will have different accessibility to the pores of the gel. The advantages of this technique are its simplicity, rapidity (5-10min), and wide selection of pore sizes [47]. However, many disadvantages still exist, including low yield of protein reconstitution and wide range of size distribution [52]. These factors put off the use of this method. Dilution results in spontaneous proteoliposome formation using a buffer without detergent to decrease the concentration of the detergent below CMC. One example is a reconstitution involving 0.5% cholate followed by a 25-time

dilution with the detergent free buffer [53]. Another uses the octylglucoside micellar solution [54]. Two advantages of this method include: short experiment time and controlling precisely the rate of dilution using step-by-step syringe pumps or synchronous motors. However, disadvantages include: use of high CMC detergents, and extra purification step to concentrate the diluted product without fully removing the detergent.

### 1.4- New Strategy for Membrane Protein Reconstitution

A new method (Figure 1.3) for membrane protein reconstitution has been developed which starts from pre-formed pure liposome, based on the hypothesis that detergent removal is the mirror image of detergent solubilization of liposomes [33, 55-57]. Many successful proteoliposomes have been created using this method that maintain the original function of the protein as in its native system [45, 58-60]. In this protocol, detergent of varying concentrations is first added to preformed vesicles resulting in mixed micelles. This creates a set of intermediates of lipid-detergent structures during dialysis. Protein is then added during pre-determined solubilization steps. In the next section, we will briefly discuss the four steps in this procedure.

Preformed pure liposomes can be made by reverse phase evaporation in preparing large homogeneous unilamellar liposomes with a mean diameter no larger than 150 nm [36, 40]. In this case, phospholipids are

dried under high vacuum and the resultant white film is dissolved in diethyl ether, creating a second phase and ultimately a water-in-oil emulsion. Then, aqueous buffer, sonication and rotary evaporation are used to remove the organic solvent leaving behind a viscous gel that then collapses into a large multilamellar vesicles suspension with more evaporation. Finally, this mixture is passed through an extruder with polycarbonate filters of pore size 0.4 and 0.2 μm. Other techniques to prepare pure liposomes include dialysis and gel filtration.

Addition of detergent to the preformed aliquoted liposomes can be tracked by turbidity of phospholipid liposome suspension measured between 400-700 nm or by light scattering changes with a flourimeter set at 400 nm. The solubilization has been viewed as a three-step process that is viewed in lipid-detergent suspensions turbidity [45, 55]. In the first step, detergent inserts into lipid bilayers until it's saturated with no dissociation of the liposomes and no changes in turbidity. Step two marks a huge drop in turbidity as further solubilization of vesicles results in little lipid-detergent micelles. Lastly in step three, full solubilization results in lipid-detergent micelles with a physically transparent appearance as shown in figure 1.4 and and Table 1.1.

The protein used in this process must be in a monodisperse detergent protein solution that can be confirmed via gel chromatography or gel

electrophoresis. The concentration of protein and the concentration of detergent carried with the protein are inversely proportional. Thus, a setback in case of low detergent concentration is the possibility of forming premature reconstitution between the membrane protein and other detergents. As discussed above, of all the existing detergent removal methods, Bio-Beads SM-2 is the most effective. To analyze the success for detergent removal, turbidity experiments are a terrific way to track this [56, 60]. The original micellar mixture will be optically transparent but as detergent is removed, the turbidity increases and then plateaus indicating the end of the micelle to detergent saturated liposome transition.

### 1.5 - Other Determinants for Membrane Protein Reconstitution:

There are several parameters described below that affect the efficiency of membrane protein reconstitution. The first one is the type of detergent chosen. A variety of detergents can be used for reconstitution, but a desired detergent will be one that will give the highest yield of protein incorporation. So far, three different models have been proposed to illustrate the association of lipids and membrane proteins (Figure 1.4) [33, 45, 58-60]. The first one involves direct protein insertion into detergent saturated liposomes, and the second one describes direct protein insertion from micellar structures to detergent saturated liposomes. The last one allows for proteoliposomes to form from micellar-to-lamellar transition. To guarantee

unidirectional insertion of the protein, three detergents, octylglucoside, dodecymaltoside, or Triton X-100 detergents have been used in the procedures with preformed liposomes. The second factor is the lipids that will be used. Phosphatidylcholine molecules are the most common phospholipids used because of the low cost, neutral charge, and chemical inertness. In some cases, charged lipids may also be used because the charge repulsion prevents unnecessary vesicle fusion and complete function of proteins relies on negatively charged lipids. Cholesterol can act as a wonderful addition for stability and better impermeability of ions and small polar molecules into the proteoliposomes. Also the pure and high quality lipids should be used to reach high yield of liposomes by avoiding lipid oxidation and eliminating impurities (such as lysoderivative). Lastly, one needs to be very mindful when choosing detergent resistant lipids and lipids that only form monolayers (phosphatidylethanolamine) [61].

Other parameters include: lipid-to-protein ratio and rate of detergent removal. The method outlined so far works wonderfully for lipid-protein ratios of 800 to 10 (w/w) with increasing activity depending on the amount of protein available. However, if the ratio is less than 10, immediately protein aggregation and proteoliposome permeability is increased with a decrease in reconstitution efficiency. Both slow and fast rates have their own advantages in proteoliposome formation. Slow rates help with encouraging micelles homogenous and effective reconstitution. However, fast removal is more

beneficial for proteins that tend to aggregate in case of Ca-ATPase [59], and by avoiding multilamellar structures in case of dodecylmaltoside [45]. The use of Bio-beads could control the rate of detergent removal, depending on the amount of beads added. However, the rate of removal and amount of beads used must be pre-determined with an appropriate temperature [50, 51].

**1.6 - Conclusion**: In order to study the function of membrane proteins, reconstitution into an artificial membrane can provide great knowledge. From past literature, many techniques and protocol have been optimized to obtain desired proteoliposomes. Despite the increasing amount of membrane proteins, the future is still bright and newer techniques are developed in terms of controlling the size, shape, and number of proteins incorporated into a membrane. The next section of the introduction visits the field of DNA nanotechnology and the marriage of this with current liposome formation techniques can revolutionize the methods available on templating vesicles and creating proteoliposomes.

## 1.7 - STRUCTURAL DNA NANOTECHNOLOGY

DNA nanotechnology is a field in which the 2- and 3-dimentional DNA structures in the nano-scale can be made based on the self-association DNA molecules in which two single strands of DNA hybridize to form a double helix. The complementary base pairing properties of A (adenine) - T (thymine) and G (guanine) – C (cytosine) by hydrogen bonds between DNA strands provides "the finest possible level of control over the spatial and temporal structure of matter: Putting what you want, where you want it in three dimensions, when you want it there" [62].

## 1.8 - Development of DNA nanotechnology

In 1982, Nadrian Seeman pioneered this revolutionary field by proposing that DNA could create not only linear duplexes but also immobile junctions. And that this can be combined with sticky end Watson and Crick base pairing to form three-dimensional complex networks [4]. This principle is the crucial inspiration for researchers to investigate the possibility of combining linear DNA via sticky end cohesion without the need of a crystal structure to determine the alignment of the two components [63]. Furthermore, the branched DNA molecules can be synthesized and assembled into more complex structures by in vitro hybridization, which is essential to DNA nanotechnology. In figure 1.5, 4 units of the 4-arm branched

junction base unit can combine to form a quadrilateral from inter-structural association. The use of branched DNA molecules marked the stepping-stone for later developments such as cube and truncated octahedron [64, 65]. The ability to control DNA hybridization, the readily obtainable synthetic DNA, and the capability to pattern structures using branched DNA molecules would later prove momentous in specifically positioning protein, aptamers, metal nanoparticles, and quantum dots [66-71]. However, the problem here is that uniform finite shape and size is still uncontrolled.

Earlier work required interactions between a large numbers of short oligonucleotides to form the final structures in a precise control of stoichiometry (relative ratios between the strands). Thus, multiple reaction and purification steps were required that often times resulted in low yield products. The field of DNA nanotechnology took a monumental turn in 2006, when Rothemund introduced the use of a "scaffold" DNA strand in building aperiodic structures, referred to as DNA origami. Historically, origami is known as the Japanese art of skillfully folding paper into an arbitrary shape. In DNA origami, a long scaffold single strand of DNA (~7,429 nucleotides long from the M13 genome) is guided and folded into distinct two-dimensional (2D) shapes using hundreds of short staple strands. Introduction of short staple strands tremendously impacts and directs the formation of DNA structures. In this case, each of the staple strands serves to bind to different regions of the scaffold strand and helps to bring detached

points into close proximity, thereby determining the exact size and shape of the final compact structure [72]. Figure 1.6 shows that each of the staple strands has a distinct sequence and that the position it binds along the scaffold is determined based on the final design of the product.

In order to transform DNA origami into three-dimensional (3D) structures, three different kinds of strategies have been developed. The first one reported in 2009 involves the connection of planar origami 2D structures at the edges to yield hollow 3D cages with a controllable lid (figure 1.7) [73-76]. Another is described in a method reported by Shih et. al. during the same year in which the parallel arrangement of helices were made into honey comb lattice or square lattice (figure 1.8). As shown in figure 1.9, within these firm 3D blocks, target inclusion and removal of base pairs results in bent and twisted 3D objects [2, 77, 78]. The third method reported is the use of concentric rings of DNA with varying turns that resulted in different circumferences and high curvature from which the objects, such as 2D arrangements of concentric rings, 3D spherical and elliptical shells, and nanoflasks, were then created (figure 1.10) [79].

### 1.9 - Application of DNA nanostructures

The sequence specificity and spatial addressability of DNA nanostructures provide the abundance of structural advances. This unique

spatial addressability has prompted great interests on the functionalization of DNA origami. Some of the first developments include Yan and coworkers' RNA sensor. This RNA sensor releases a signal when one single strand extension from staple strands hybridizes to a target of biological interest, in this case, the targeted RNA molecule [80]. Another interesting development at the single molecule level was to detect single nucleotide polymorphism (SNP) using DNA nanostructures reported by Subramanian et al. in 2011 [81]. A third discovery involves the conjugated DNA origami structures in controlling distance between two lines of aptamers to bind a target protein [82] [83]. This last discovery has made the DNA nanostructures a broad application in different areas by conjugating DNA origami with silver and gold nanoparticles [84-88], carbon nanotubes [89], quantum dots [87], dendrimers [90], virus capsids [91], streptavidin [92-94], and Ni-NTA attached to His-tagged protein [95].

In order for DNA origami to be incorporated into functional systems, the orientation and position the DNA structure must be highly controlled. The first published method described that origami structures (negatively charged) can bind to the hydrophilic patterns etched onto a hydrophobic surface [96, 97]. Figure 1.11 illustrates how the position, orientation, and overall pattern of chemical modifications are controlled. Another method was to use silicon bound gold islands that deposit and adsorb DNA origami in a selective fashion [98, 99]. In other more progressive application, DNA

origami has served as a molecular board in which chemical functionalities were displayed on the surface and with click reactions peptide bond were formed. Biotin-Streptavidin interactions were also utilized for visualization by AFM [100]. Of great interest for the future will be the exploitation of this technique in studying protein binding. Almost 30 years after Seeman's initial discovery, researchers now have to their advantages a horde of designs, patterns, and methods with the power to control and create multifaceted systems for scientific applications.

Taking advantage of spatial addressability of DNA nanostructures, this project will center on designing and producing three-dimensional DNA nanostructures and then to using them to direct formation of liposomes with defined sizes and structures.

### 1.10 - Basic Elements of DNA nanostructures:

There are three basic elements in making DNA nanostructures. The most fundamental design of a branched DNA junction is the double crossover (DX). As shown in figure 1.12, this consists of a double juxtaposed 4 way junctions connected by two double helical domains, commonly observed in 2D arrays. All other motifs are variants of the DX [101]. Another motif is the paranemic crossover (PX), where the same polarity DNA strands are weaved through every possible site between another two neighboring side-by-side

double helices. A third motif is the $JX_2$ motif, which is the topo-isomer of the PX motif. In fig 1.12, one will notice that the relative positions of the ends of PX and $JX_2$ are mirror images of one another. The 180° rotation between the two can be caused by trading two component strands in the motif with other strands [102].

## 1.11 - Principles of DNA origami design and its preparation:

In DNA origami, a long single stranded scaffold (typically 7249-nucleotide-long circular strand of the M13 phage genome) is folded into an arbitrary shape by short single stranded oligonucleotides (typically around 200) called "staples". The staples form crossovers at every (n+0.5) helical turn and hold neighboring portions of the scaffold together. DNA origami when viewed as a whole follows the DX motif rather well.

In designing a DNA origami structure, the first step is to define its final shape and structure. The basic structures of canonical DNA and origami DNA are slightly different. The canonical DNA has a helical turn of 3.4 nm (10.5 nucleotides) with a diameter of 2 nm. However, due to an electrostatic repulsion induced inter-helical gap, the helical turn of origami DNA is increased to 3-3.5 nm in length (10.7 nucleotides), and also its width is

increased to 3.5 nm. The hybridization of the scaffold with staple strands can expand the final origami structure up to 8500 $nm^2$ in size.

Figure 1.6 shows an example in designing DNA origami structure. To avoid the undesired strain on the helices, the crossovers (located at departure points between helices) are strategically placed along the scaffold. When the scaffold transfers from the neighboring helix to a third helix, the distance between crossovers is an odd number of half helical turns. However, if the scaffold proceeds to the initial helix, the distance will be an even number of half helical turns. In this design, the single stranded staple strands can hybridize to three neighboring helices. The geometry of formed structures could be either the S-shaped or Z-shaped. When the space between the crossovers is 1.5-turns, the length will be 32 nt. If the space is increased to 2.5-turns, the length will be up to 52 nt accordingly.

To bring the helices together, with the main 16 nt stretch (of staple strands or of crossovers) binding to one helix, the group of the 8 nt at both ends will hybridize to the adjacent helices. Once the scaffold strand is hybridized to all its staple strands, a pair of helices at every 32 nt is bundled by multiple crossovers, and this pair is linked to a third helix by creating a dihedral angle of 180°. Oftentimes, because the straight edge DNA base pairs are tremendously hydrophobic, they can stack to one another. To solve this issue, single stranded $T_4$ loops has added to the edge staple strands. Further

staple strands extended with dumbbell hairpins will offer "pixels" for surface modeling of locally height different origami structures.

The structural design discussed above can be done on software called CADnano. After obtaining the staple and scaffold strands, the origami structure is immediately formed upon annealing of all the strands in a buffered solution. Typically, each scaffold is accompanied by 2-10 equivalents of staple strands and reacted in a buffer containing Tris (40 mM), acetic acid (20 mM), EDTA (2 mM), and magnesium acetate (12.5 mM, 1x TAE/$Mg^{2+}$ buffer). To denature the DNA strands, the mixture can be heated at 90°C for 10 min and then annealed in a PCR cycler by cooling to room temperature at -1.0°C/min. AFM solution imaging (in 1x TAE/$Mg^{2+}$) on fresh mica or negative stain EM can be used to verify correct folding of the origami structure. The magnesium ion plays a key role in the folding process because at the crossovers, it neutralizes, stabilizes, and brings together the DNA backbone consisting of negatively charged phosphodiesters. It further helps sticking the origami product to the mica surface or FCF400-Cu FORMVAR carbon film grids surface by salt bridging. Figure 1.13 shows a wide variety of 2D nanostructures folded by the DNA origami method [72].

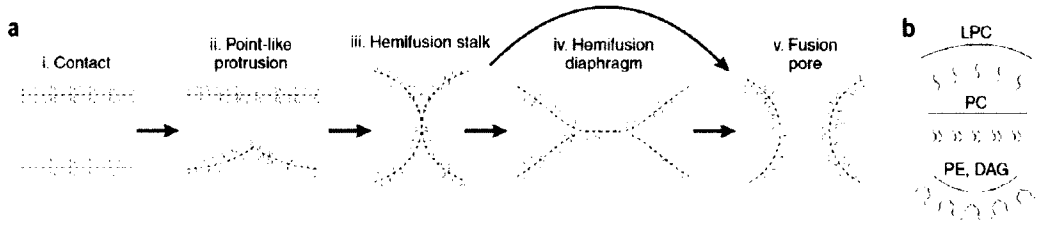


Figure 1.1 – Fusion of protein free lipid bilayer. (a) (i) Membrane contact before fusion. (ii) Hydration repulsion energy between these merging membranes are minimalized by the protrusion. (iii) Hemifusion stalk intermediate with the proximal lipids and distal lipids fused and unfused respectively. (iv) Diaphragm is the result of further stalk fusion. (v) Final fusion pore connects the outer and inner leaflets of the two merging membranes. (b) Different lipids form monolayers of different curvatures. Lysophosphatidylcholine (LPC) is inverted cone shaped and bulges in the direction of the polar head. Phosphatidylethanolamine (PE) and diacylglycerol (DAG) are both cone shaped and bulges in the direction of the hydrocarbon chains. Lastly, phosphatidylcholine is cylindrical and forms a flat monolayer. Reprinted from Chernomordik *et al* [8]. Copyright 2008 Nature Publishing group.

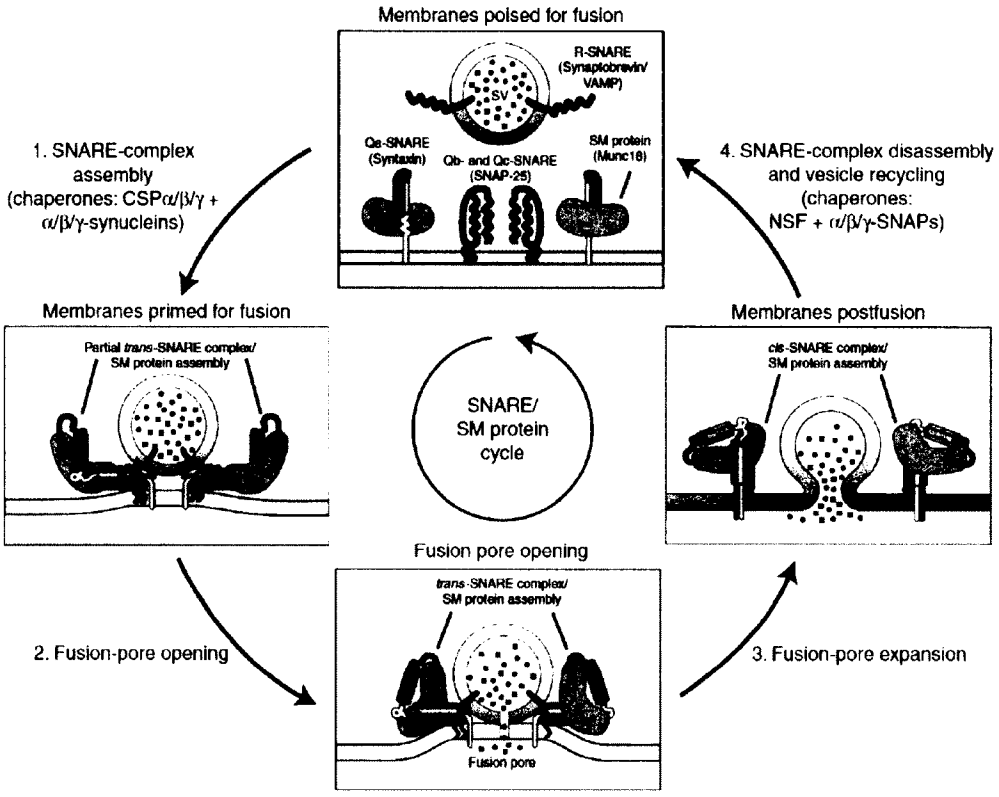


Figure 1.2 – Before fusion begins, SNARE and SM proteins are positioned on the membranes as proteins in their native state or folded in a way independent of the canonical SNARE complexes. During the membrane-priming step (1), SNAREs form partial *trans*-complexes with association to the SM proteins when the latter binds to the syntaxin amino terminus. During the fusion pore opening in step (2) the SNAREs take on the *cis*-formation after the complex pulls the membrane apart and the vesicle membrane mixes into the target membrane during step (3). To finish the cycle, ATPase NSF dissociates the *cis* -SNARE complex with its chaperones

and the components prepare for another round. Reprinted from Sudhof *et al* [121]. Copyright 2011 Cold Spring Harbor Laboratory Press.

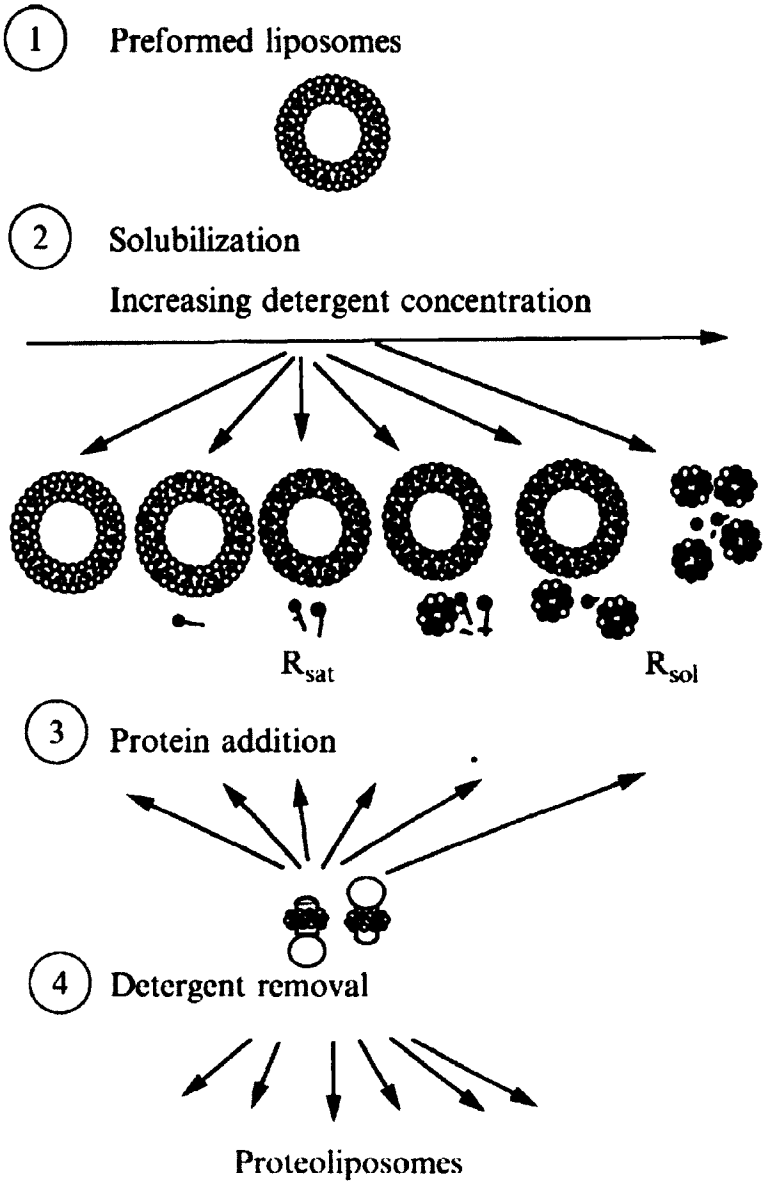


Figure 1.3 - Four-stage protein reconstitution method. (1) Large and homogenous vesicles are produced. (2) During, methodic step-wise addition of detergent to the preformed liposomes, various steps in the solubilization process are depicted. $R_{sol}$ and $R_{sat}$ are the detergent to lipid ratios in liposomes at the onset of solubilization and when total solubilization is complete respectively. The next step (3) is the addition of protein and lastly

during step (4), detergent is removal. Reprinted from Rigaud *et al* [49]. Copyright 2003 Elsevier Inc.

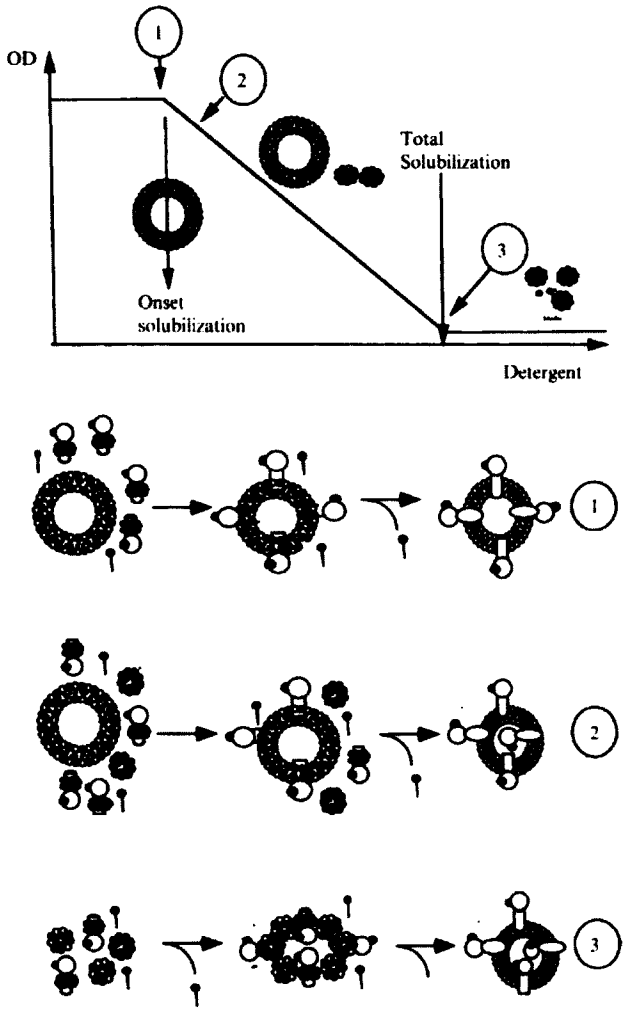


Figure 1.4 - Protein reconstitution mechanisms. The top plot depicts the lamellar to micellar transition, which can be judged by turbidity. In the bottom schemes, three proposals are presented, which affects the orientation of the protein. (1) At the onset of solubilization, proteins can directly insert into detergent saturated vesicles. (2) Proteins can be removed from mixed micelles and deposited into detergent saturated liposomes. (3) Protein can undergo incorporation by micellar coalescence. Reprinted from Rigaud *et al* [49]. Copyright 2003 Elsevier Inc.

TABLE I

PARAMETERS DESCRIBING SOLUBILIZATION OF LIPOSOMES BY VARIOUS DETERGENTS[a]

| | $D_{water}$ | | $R_{sat}$ | | $R_{sol}$ | |
|---|---|---|---|---|---|---|
| Detergent | m*M* | mg/ml | mol/mol | w/w | mol/mol | w/w |
| Triton X-100 | 0.18 | 0.12 | 0.64 | 0.5 | 2.5 | 2.0 |
| $C_{12}E_8$ | 0.20 | 0.11 | 0.66 | 0.45 | 2.2 | 1.5 |
| Octylglucoside | 17 | 4.9 | 1.3 | 0.48 | 3.0 | 1.1 |
| Dodecylmaltoside | 0.3 | 0.15 | 1 | 0.65 | 1.6 | 1.0 |
| Cholate | 3 | 1.29 | 0.3 | 0.16 | 0.9 | 0.5 |
| CHAPS | 3.15 | 1.94 | 0.4 | 0.31 | 1.04 | 0.8 |
| CHAPSO | 1.6 | 1.1 | 0.21 | 0.17 | 0.74 | 0.6 |

*Abbreviations:* CHAPS, 3-[(cholamidopropyl)-dimethyl-ammonio]-1-propanesulfonate; CHAPSO, 3-[(cholamidopropyl)-dimethyl-ammonio]-2-hydroxy-1-propanesulfonate.

[a] The process of solubilization can be described quantitatively by the general equation $D_{total} = D_{water} + R_{eff}$ [lipid], in which $D_{total}$ is the concentration of the detergent to be added to reach any step in the solubilization process; [lipid] is the lipid concentration; $D_{water}$ is the aqueous monomeric detergent concentration, that is, the CMC determined in the presence of lipids; $R_{eff}$ is the effective detergent-to-lipid ratio in mixed lipid–detergent aggregates ($R_{eff} = R_{sat}$ at the onset of solubilization represents the detergent-to-lipid ratio in detergent-saturated liposomes; $R_{eff} = R_{sol}$ at total solubilization represents the detergent-to-lipid ratio in lipid–detergent micelles).

Table 1.1 - Summarizes the results from the solubilization process in Fig 1.3 from various detergents. The parameters include $D_{total}$, $D_{water}$, $R_{eff}$, $R_{sat}$, and $R_{sol}$, which all affect and impact the solubilization of liposomes by the listed detergents. Reprinted from Rigaud *et al* [49]. Copyright 2003 Elsevier Inc.

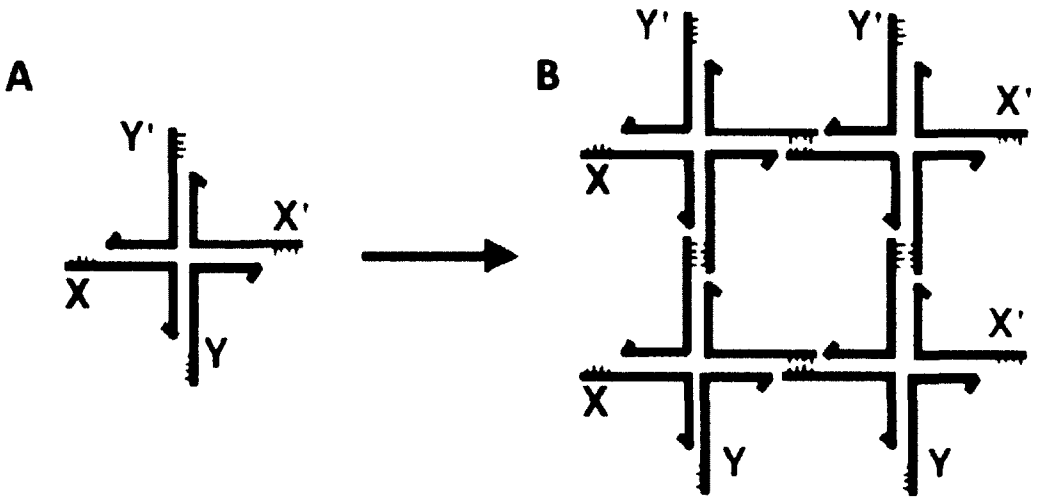


Figure 1.5 - (A) 4-arm branched DNA junction (B) Four copies of the branched junction will form a quadrilateral from the sticky ends, which then gives the structure liberty to form infinite lattice. Reprinted from Seeman[62].

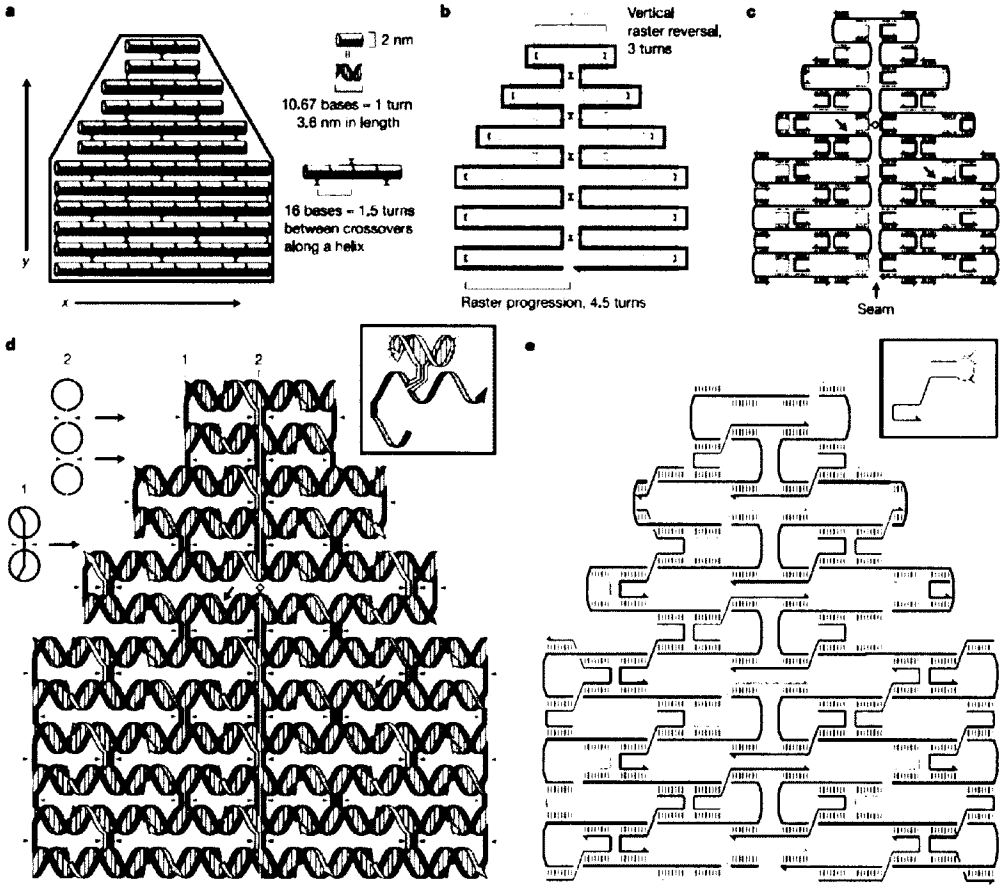


Figure 1.6 - (A) Double helices (cylinders) and crossovers (blue tacks) form the backbone of a shape (red). (B) Extra crossovers are created to fold a long black scaffold into the helices. (C) Multicolor staples fold the scaffold strand and connect two helices. (D) Three types of crossovers are illustrated here with triangles: scaffold cross overs (red triangles), periodic crossovers with minor grooves on top face (black triangles) and with minor grooves on top face (blue triangles). Numbers 1 and 2 are crossover cross-section and represent the location of backbones (in colored lines) and major and minor grooves. The black arrows in **c** represent the green strands in **d**. Positions where staples are cut and resealed are pointed out by the yellow diamonds in **c** and **d**. (E) The final design of the desired shape is seen in **a** with staples

(32mer) connecting through three helices. The inset is a dumbbell hairpin **d** and 4-T loop **e**. Reprinted from Rothemund[72]. Copyright 2006 Nature Publishing Group.

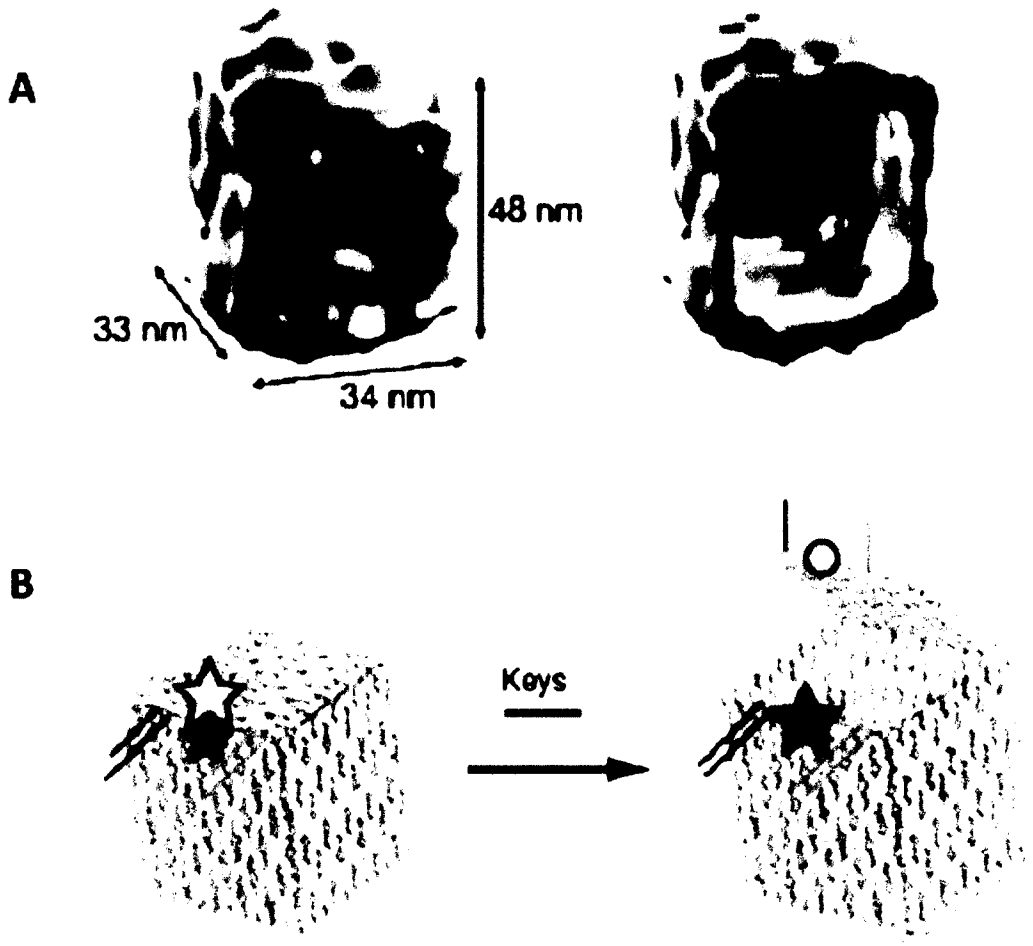


Figure 1.7 - DNA box. (A) This structure is a cryo-TEM reconstruction. (B) Depicts the opening of the lid by DNA keys. Reprinted from Torring *et al* [105]. Copyright 2011 The Royal Society of Chemistry.

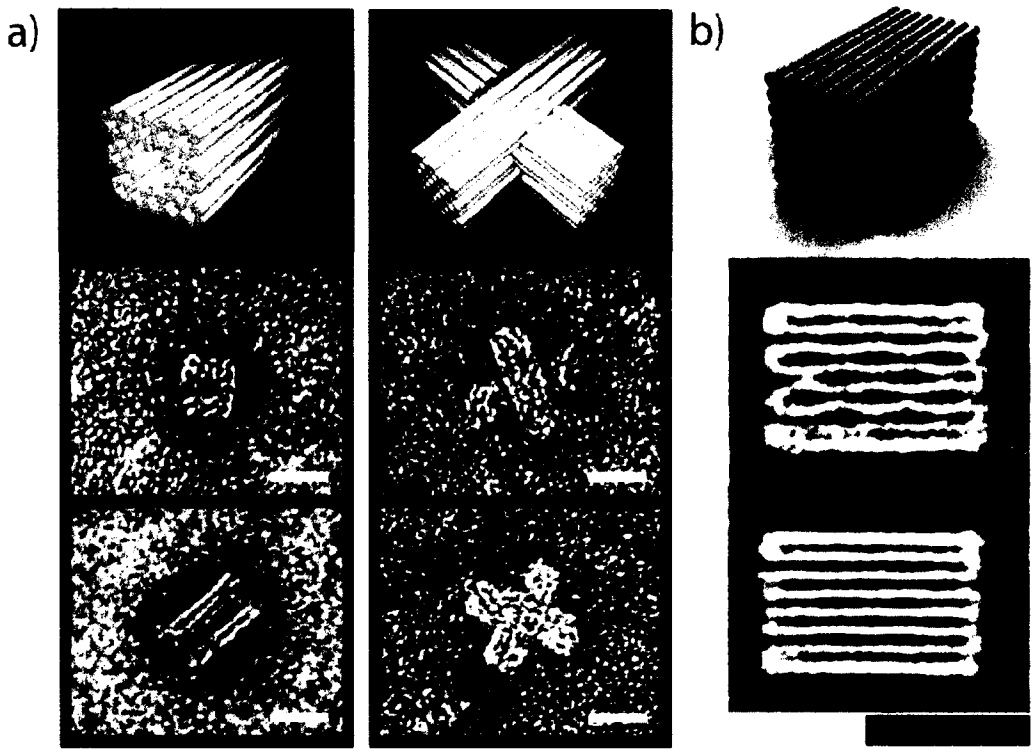


Figure 1.8 - In (a) Two 3D origami structures from honey comb lattice foundation. (b) Formation of a square lattice from layers of helices also generated from DNA origami methods. Reprinted from Torring *et al* [105]. Copyright 2011 The Royal Society of Chemistry.

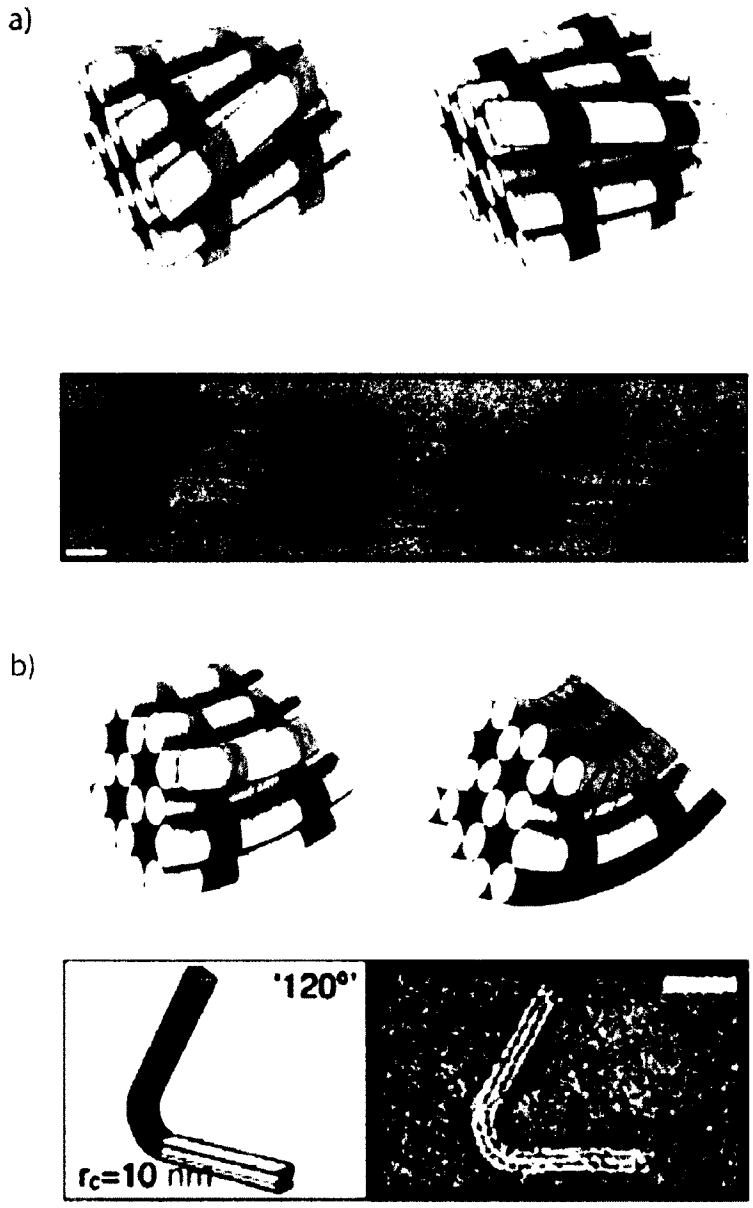


Figure 1.9 – An origami structure that incorporates twists and curvature. When varying the number of base pairs between crossovers (a) left handed and right handed twists are determined by designs with fewer or more than 10.5 bps/turn respectively. (b) The combination of both confirmations depicted in (a) will result in a balanced curvature. Scale bars 20 nm.

Reprinted from Torring *et al* [105]. Copyright 2011 The Royal Society of Chemistry.

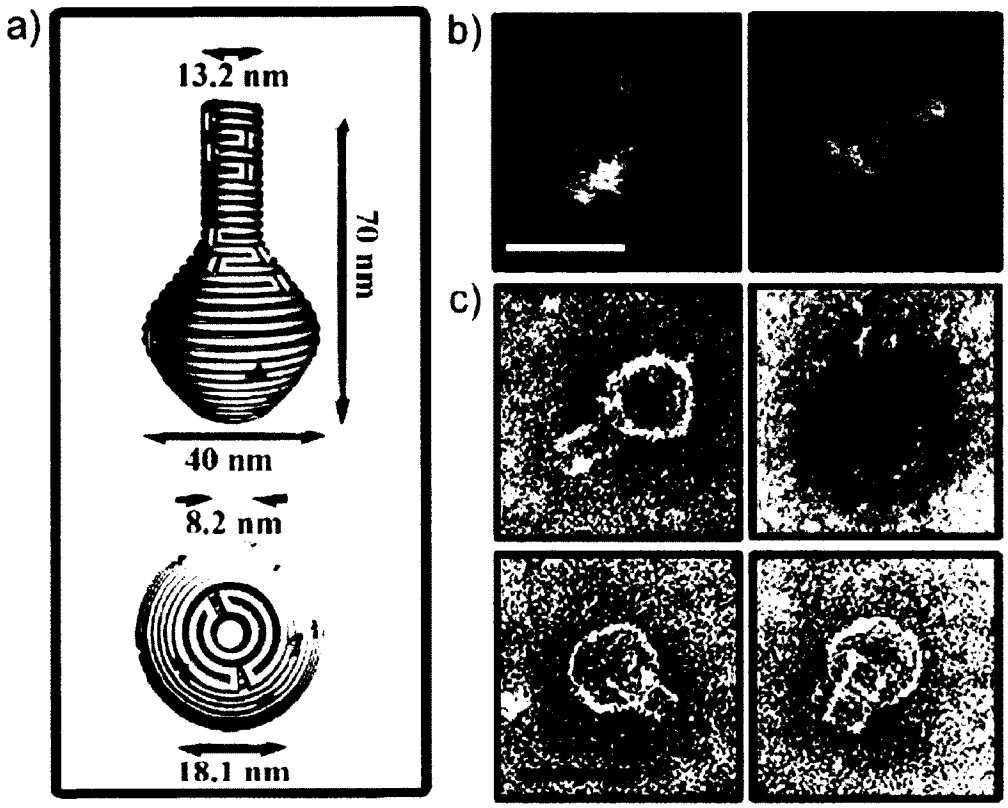


Figure 1.10 – The ability to manipulate and control crossover networks will allow for rounded contours. (a) Design of a nanoflask (b) AFM showing successful formation of the nanoflask (scale bar 75 nm). (c) TEM images of the nanoflask (scale bar 50 nm). Reprinted from Torring *et al* [105]. Copyright 2011 The Royal Society of Chemistry.

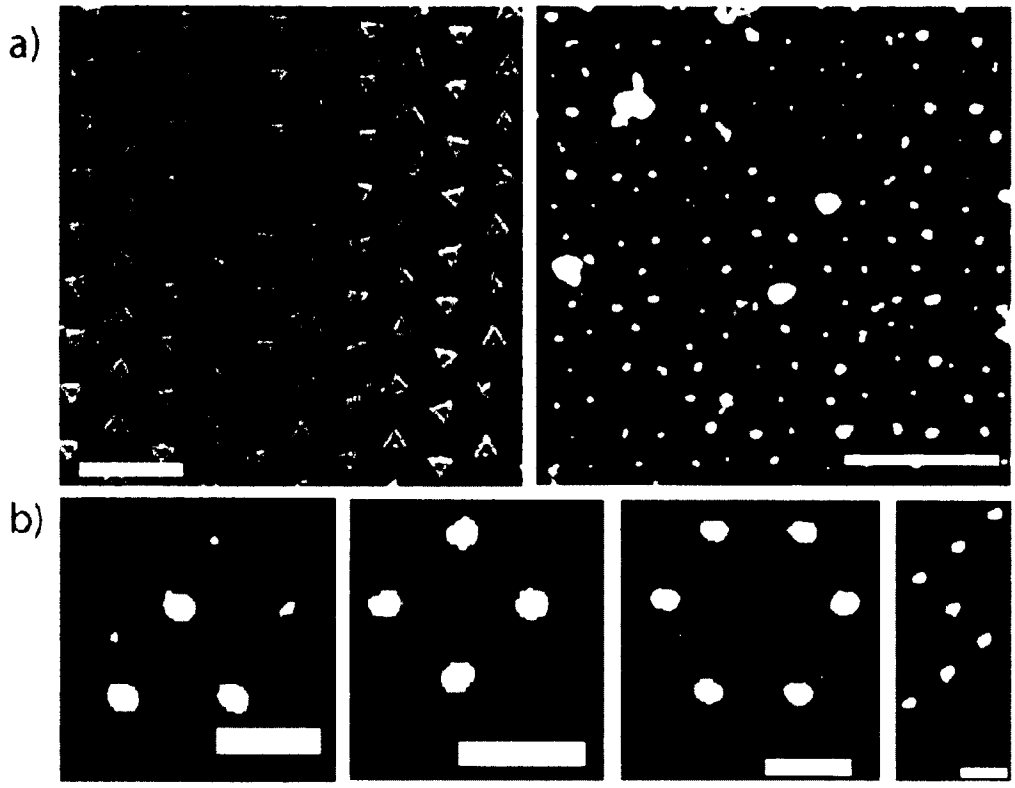


Figure 1.11 – (a) Lithographic patterning depicting position and direction of origami triangles. In the right, gold nanoparticles (AuNP) have been added. (b) DNA origami nanotubes connect gold islands. Reprinted from Torring *et al* [105]. Copyright 2011 The Royal Society of Chemistry.

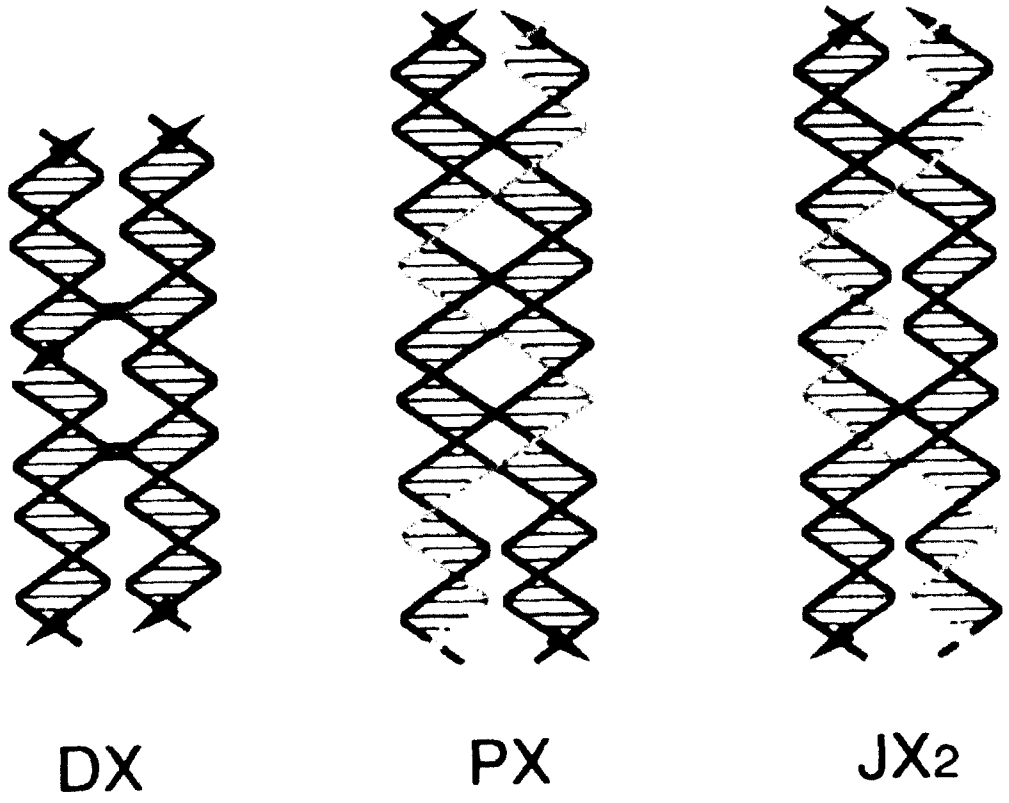


Figure 1.12 – Three critical motifs in DNA nanotechnology. Reprinted from Kuzuya *et al* [122]. Copyright 2010 The Royal Society of Chemistry.

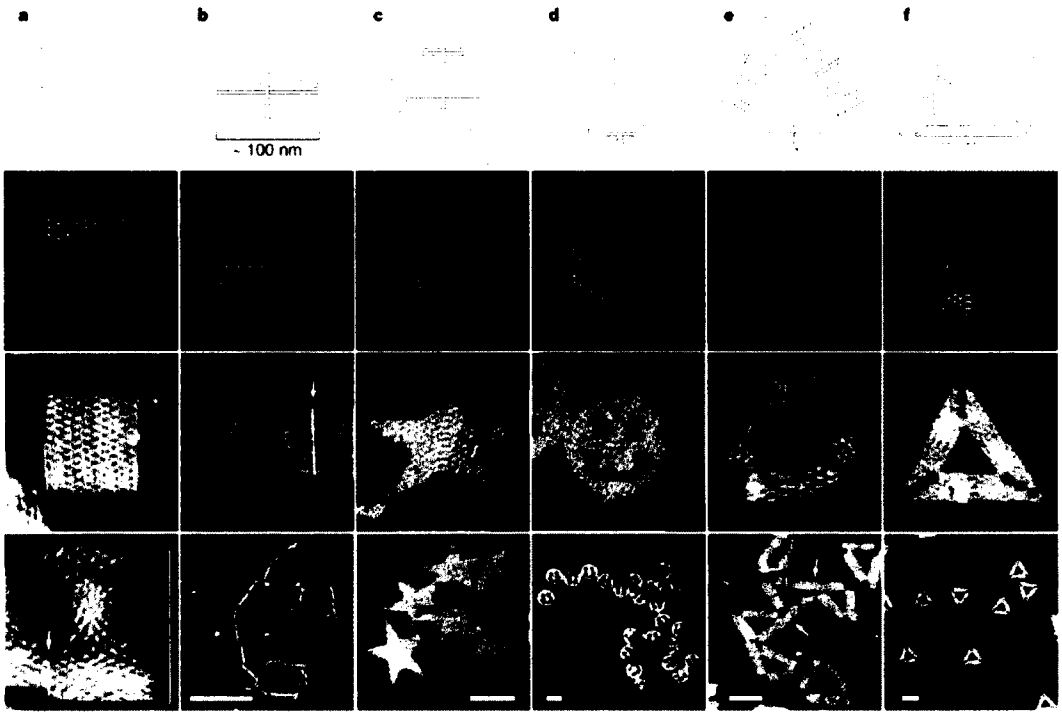


Figure 1.13 - Top row is the folding directions of six shapes. (A) Square (B) Rectangle (C) Star (D) Three-hole disk (E) Triangle with rectangular domains (F) Triangle with trapezoidal domains with red lines between the domains. The loose and hanging loops are single stranded unfolded sequences. In the second row, along each structure's folding path, the colors point to base pairing (red is the start and purple is the end). The last two rows are AFM images. Blunt end stacking are shown by the arrow and white lines. White brackets show unstretched versus stretched square. Scale bars are **b** 1μm **c-f** 100 nm. All images without scale bars are 165nm x 165nm. Reprinted from Rothemund[72]. Copyright 2006 Nature Publishing Group.

٥

## CHAPTER 2 - TEMPLATING VESICLE SPHERICAL SHAPE

During past 30 years, methods have been developed to fold DNA into different nanostructures [103-105]. These structures include such shapes as DNA hexagons, octahedrons, cubes, and prisms [103]. In 2006, Rothemund revolutionized the DNA nanotechnology field by establishing a method called 'scaffolded DNA Origami' [72]. In this approach, a 100-fold excess of hundreds of short single stranded staples was used to guide the folding of a long scaffold single strand through complementary base pairing. The resulting structures were around 100 nm in diameter with spatial resolution of 6 nm.

Figure 1.6 illustrates how to use 'scaffolded DNA Origami' in designing and making DNA nanostructures [72]. In this design, the basic structural building blocks are the cylinders and the basic building materials are: 1) a long scaffold strand, 2) 'scaffold crossovers', and 3) 'staple strands'. The designed DNA nanostructures will consist of cylinders with different lengths. Each cylinder is made from two DNA helices that are bound to one another via periodic arrangement of crossovers. Electrostatic repulsion keeps the parallel helices in position without packing together [106], and thus the yielded cylinders would have x-dimension of 3.6 nm (per turn) and y-dimension of 4 nm (per two helices). The long scaffold strand is folded in raster fill pattern and becomes one strand of the double helix in every

cylinder, and 'scaffold crossovers' were used to carry the scaffold from one cylinder to another. The 'staple strands' via complementary base pairing direct this folding process. With staples, direction is reversed at the crossovers or antiparallel, yielding a very stable structure [107]. In general, odd number of half turns is reserved for the distance between 'scaffold crossovers'. However, if the raster changes direction, the distance between 'scalffold crossovers' must be an even number of half turns. As shown in figure 1.6, whenever two of these staple strands run into one another, there is a nick in the backbone on the top and bottom faces of the cylinders. A couple of adjacent staples merge across nicks so that larger binding domains are granted between staple and scaffold. This follows the pattern of higher binding specificity and energy leading to higher melting temperatures.

Based on this strategy, Rothemund folded six different structures (Figure 1.13) [72]. Thus, in this chapter, we adapt Rothemund's method to create larger and more complex three-dimensional ring structures with virus M13mp18 circular genomic DNA. M13mp18 is a widely used scaffold because it has a natural sequence with a stable secondary structure and the staple strands can be generated with little error and in correct stoichiometries. We have successfully designed and produced 6- and 12-helical bundle rigid circular origami rings and demonstrated that lipids can be strategically attached in selective ways. Further we show that membrane structures were formed either on the inside or on outside using lipid linked

scaffolds and that rotation positioning of lipids can further affect the final templated phospholipid structure.

## 2.1 - Formation of Rigid Circular DNA Rings with Molecule Ligand Attachment Handles

The rigid circular DNA rings were formed from M13mp18 DNA using the 'scaffolded DNA Origami' method. The ligand attachment handles were added on either inner or outer surface DNA rings for the lipid attachment. Spatial location and orientation, and functionality of these handles were confirmed with gold-nanoparticle conjugated DNA oligos complementary to the handles. These experiments described in the following section were done in Dr. Chenxiang Lin's group.

Figure 2.1 shows the design and creation of four DNA origami rings with diameters of 28 nm, 47 nm, 61 nm, and 94 nm. Also shown is the model and the negative stain electron microscopy (EM) images of the ring. The two rings used in this thesis are the 46nm (6hb) and 60 nm (12hb) rings.

To confirm the location, orientation, and functionality of the handles, the gold-nanoparticle (AuNP) conjugated DNA oligonucleotide strands were used to demonstrate the selective attachment of molecule ligands onto the DNA origami ring. The AuNPs were coupled to thiolated DNA oligonucleotide

strands complementary to the inner DNA handles [86]. The coupled product was hybridized to our DNA origami ring handles and the assembled product was analyzed by agarose gel electrophoresis. The desired product band of DNA origami ring with AuNP-oligonucleotide strands was then cut and purified from the gel, and imaged using negative stain EM. In figure 2.3, the 6hb 3inner handle ring was used to prove correct attachment. The 3 inner handles were hybridized to their complimentary AuNP-oligonucleotide strands. We observed circular rings of 46nm in diameter, majority of which contained 3 dark spots (AuNP) inside at the correct positioning where the 3 inner handles are located. A few rings did contain deformed and incorrect positioning and number of AuNP, but those were not the majority. These results demonstrated successful synthesis of the origami rings and the correct location and inward orientation of the ring's inner handles. These handles on the surface DNA rings can bind their complementary ligands via base pairing.

## 2.2 - The Formation of Membrane Structures on the Inside or Outside Using the Lipid-Linked Scaffolds

To study the roles of DNA Origami Ring in templating lipid vesicle formation, the lipid-linked anchors were produced and tested. These anchors (figure 2.4) were lipid-conjugated DNA oligonucleotide strands complementary to the handles on the DNA Origami Ring. Thus, the DNA

oligonucleotide portion of the conjugates will bind to the DNA Origami Ring while its lipid portion will intercalate into the lipid membrane structures (figure 2.5).

*2.2 a - Manufacture and Characterization of DNA Origami Ring Templated Vesicles*

Oligo-lipid conjugates serve as the main anchoring units that allow lipid structures to seed on the DNA ring templates. Here, we show an example of anchoring oligo-lipid conjugates on the inner surface of DNA Origami Ring. The inner handle sequence is 5'-AAATTATCTACCACAACTCAC-3' and the direction is 0° pointing directly inward towards the center of the ring and the three handles are located 120° apart from one another. As shown in figure 2.4, a complementary 5'thiol modifier C6 S-S Oligo-Cy5 is ordered from Integrated DNA Technologies (IDT). On this molecule, a cyanine dye (Cy5), containing a hydrophilic sulfonate group, was used to label the 3' end of the nucleic acid. The anti inner handle oligo sequence is 3'-TTTAATAGATGGTGTTGAGTG-5' (designated as anti iv in this study). The 5'thiol modifier reacts with dithiothreitol (DTT) to form an intermediate that can further conjugate with the lipid, 1,2-dioleoyl-*sn*-glycero-3-phosphoethanolamine-N-[4-(p-maleimidophenyl) butyramide] (sodium salt) (Maleimide-PE). The coupled product is reconstituted into liposomes with DOPC:DOPS:PEG2K-PE:Rho-DOPE (79.2%:15%:5%:0.8%) composition and

purified using an iodixanol three layer step density gradient ultracentrifugation.

The precast SDS-PAGE gel (12% Bis-Tris Gel) was used to characterize the conjugates of thiol-Oligo-cy5 to Maleimide-PE. We have tested two lipid-oligo conjugates, and the difference between them is the length of oligos, 21mer vs 42mer. The figure 2.6 A1 confirms the purity of desired conjugate products 21mer-PE and 42mer-PE. Both lipid conjugates were observed as clean bands that run slower than both the two monomers respectively, after monomers, dimers, and impurities were removed. In the following experiments, we will use the 21mer-PE conjugate for the structural studies.

Once the conjugated product was hybridized to the DNA ring, a rate-zonal ultracentrifugation was applied (using a glycerol step gradient) to separate the pure ring complex from the free vesicle lipids and from unbound lipid-DNA conjugates. The different fractions were collected based on the glycerol density in the order of low to high. A successful formation and purification of 6hb 3 inner handle iv ring complex was shown in figure 2.6 A2. The SDS agarose gel electrophoresis (gel concentration 1.5%: 0,5x TBE, 10mM $MgCl_2$, 0.05% SDS) was used to determine location of the pure ring complex bands within fractions. The red channel detects the existence of cy5-antihandle hybridized to the inner handles of the origami ring, and the green channel reports the free rhodamine lipid mixture. The desired ring complex product emits signal from fractions 7 through 12; whereas the free

unbound lipids float up to fraction 1 through 4. The well-separated and purified ring complex product within fractions 7 and 8 (with the strongest pure signal) was combined and then used in the next step.

The purified ring complex was mixed with 200 nm extruded SUVs mix consisting of DOPC:DOPS:PEG2K-PE:Rho-DOPE (79.2%:15%:5%:0.8%) and dialyzed overnight in the presence of Biobeads to form the Saturn product. This crude product was then purified by a three-layer iodixanol step density gradient ultracentrifugation and 50 μL fractions were collected and run on an SDS agarose gel. Figure 2.6 B shows the detection on the gel of the vesicle modeled by a 12 hb 8 inner iv ring. The red channel reported the cy5 signal located on the inner handles of ring complex. The green signal represented the Rho premix liposomes. Coexistence of both red and green bands locates the fraction containing the Saturn vesicle. During the ultracentrifugation, the crude product initially placed in the bottom 30% layer is floated up and separated into pure fractions. Once the crude templated Saturns come close to their isopycnic density, it is observed that the less dense SUVs will naturally incline towards the top and DNA rings bound to it will float up with the lipid, however, unbound DNA will remain in the bottom of the tube. In figure 2.6 B, most of the vesicles are detected in fractions 1,2, and 4, and the DNA ring signal was the highest in fraction 2, with a coexistence of template rhodamine mix. Fraction 2 is then stained on FCF400-Cu FORMVAR carbon film grids and imaged using negative stain electron microscopy (EM).

*2.2 b- Formation of Vesicles Directed by Two Radically Different Geometries: 3 Handles on the Inside or 3 Handles on the Outside Surfaces of 6hb Ring.*

Negative stain EM revealed a light grey templated vesicle located within or on the ring with a diameter that is no larger than the one of the DNA ring (figure 2.7 A). The DNA ring appeared as a darker grey structure and hugs the border around the vesicle. This product was in the majority within the sample and provided the first hint of evidence that the DNA ring does dictate the size and the shape of the SUV. Our collaborators Dr. Yang Yang and Dr. Hideki Shigematsu obtained beautiful Cryo-electron microscopy images of this final structure. In these images (figure 2.8), the ring appeared to lie equatorial along the vesicle in a structure we term the Saturn. Obtaining this structure inspired design of a DNA origami ring (6hb 3 outer handle) with 3 handles positioned 180° from the center to further test the templating abilities of our design. Negative stain EM showed a dark grey DNA ring with 3 light grey SUVs (around 16-18 nm in diameter) positioned outside the ring where the handles lay. This structure we termed the "bolo" (Figure 2.7 B). The size of vesicle varied, and thus, in this case, the DNA ring templated the position of the SUVs but not the size.

## 2.3 - Effects of Rotation Positioning of Lipids on 6hb Ring Remplate Vesicle Formation

Given the radically different outcomes of template membranes by the 6hb ring, we then explored how the rotation positioning of lipids would affect the templating process. The 6 helical bundle ring with 3 handles was used in this study. The four different rings were made with 3 handles positioned at 0° (helix 3), 60° (helix 2), 120° (helix 1), and 180° (helix 0) from the center of the ring (Figure 2.9). Again, the gradient centrifugation was used to purify the product and the fractions were collected as described above. The SDS agarose gel (Figure 2.10) showed that, in the cases of 180° and 120° rings, the majority of the products were concentrated in fraction 1 and 2. But in cases of 60° and 0° rings, the crude product spanned through fractions from 1 to 6. We have imaged fractions 1 through 6 on EM. However, most of the excess lipids floated up to fractions 1 and 2 thus hindering our assessment on whether those bound to the DNA ring were specific (Figure 2.11 and 2.12). Therefore, the statistical analyses were only performed on data from fractions 3-6 as reported in figures (figures 2.13 through 2.16).

EM capture of the third fraction (figure 2.13) from the products of 180° and 120° rings revealed that the templated vesicles were in a bolo design, predominantly with the three SUVs positioned on the outside surface

of one ring. Interestingly, aggregate structures of dimer rings were also observed, in which one vesicle is linked to 2 handles on two different rings. Contrastingly, in the cases of the 60° and 0° rings (highest occurrence of 1 vesicle per ring), most of the templated vesicles located within the rings grow no larger than the circumference of the ring. There were two populations of vesicles observed with different sizes, one with a diameter between 15-18 nm similar to that observed with 180° and 120° rings, and the other with one around 38-40 nm. Further, the occurrence of the latter size is more prevalent, and most structures templated by the 60° and 0° rings contain one vesicle per ring.

In fraction 4 (Figure 2.14), we also observe this similar trend as in fraction 3 among the preparations. The 180° and 120° rings still only have majority of structures with 3 vesicles per ring (around 18nm in diameter). And the 60° and 0° rings predominantly have one vesicle per ring with diameters of two sizes, 18 nm and 37 nm.

When we move further down the gradient, fractions 5 (figure 2.15) and 6 (figure 2.16) display the expected trend for number of vesicles bound to a ring and the template vesicle diameter as in fractions 3 and 4 with several exceptions. Firstly, for the 120° Saturn, the majority of rings contain 2 vesicle per ring (fractions 5 and 6) and the only major product are the 18 nm

vesicles (fraction 5). Secondly, in fraction 6, none of the rings templated vesicles with a major peak at 37 nm.

## 2.4 - Discussion

Of major importance here was the question of what minimum handle angle will initiate fusion of neighboring handle SUVs. And is there a critical angle in which SUVs at nucleation sites will start fusing with their neighbors. We were interested in studying the effect of handle angle on templating the size and location of the liposomes. The 180° origami ring templated vesicles that floated up to fractions 1, 2, and 3, with the highest intensity at fraction 1. Since all the handles in this ring face outward, there is no constraint as to what controls the growing and grabbing of template vesicles onto neighboring vesicles. Thus, majority of the rings have the potential to bind to large vesicles and concentrate in fraction 1. The 120° origami ring has similar freedom potential of rotation to one in the 180° origami ring, however, the ability to grab neighboring vesicles is hindered a little and the resultant products separate with a bit more of a spread among the fractions. The handles on the 60° rings are angled closer inward to the plane of the ring that the constraint on "free" vesicle growth is even further controlled leading to the spread in product from fraction 1 to 6. The 0° ring is the ring with the most constrained handles and thus is the highly desired structure for templating our Saturn products. The ring boundary forces the three vesicles

to fuse with each other. It provides the greatest spread in product showing that majority of the vesicles templated by this ring will not grow larger than the ring diameter. Further, this demonstrates that the ring truly with handles at 0° templates the shape and size of the vesicle.

Under negative stain EM, fractions 1 and 2 of the 180° ring resulted in a wide variety of mixed aggregate products such as multi vesicles per ring, large aggregate vesicles per ring, and two rings linked by a common large liposome. These multifaceted products were so dominant in these two fractions that we chose to ignore them, as they were irrelevant to study of the templating effects of our various rings. In studying fraction 3 of our various rings, a critical angle required for vesicle nucleation was indicated. Majority of the products suddenly shifted from 3 vesicles per ring to 1 vesicle per ring between 120° and 60°. As the handles transition from the 180° to 0° position, the neighboring SUVs are brought closer in proximity to one another, leading to neighboring fusion. And this also allows for ease in forming the final templated structure with vesicle diameter of 37 nm, which is close in size to that of the ring. In term of the lipid contents, fractions 5 and 6 contain lower lipid concentrations than those in the less dense fractions. This would hinder the formation of the fully filled Saturn. Even with the optimal positioning of the handles to stimulate neighboring vesicle fusion, if the lipid supply is not adequate, then neighboring vesicles will not fuse. This is primarily seen in the 60° ring of fraction 5 and the 60° and 0° ring of fraction 6, in which the

majority of templated vesicles only contain one peak diameter of 18 nm. From these experiments, we learn that the minimum handle angle that will initiate fusion of vesicles is between 60° and 120°. Further, the findings from our density gradient demonstrate that the vesicles form by seeding on the individual handles first and then fuse into larger structures.

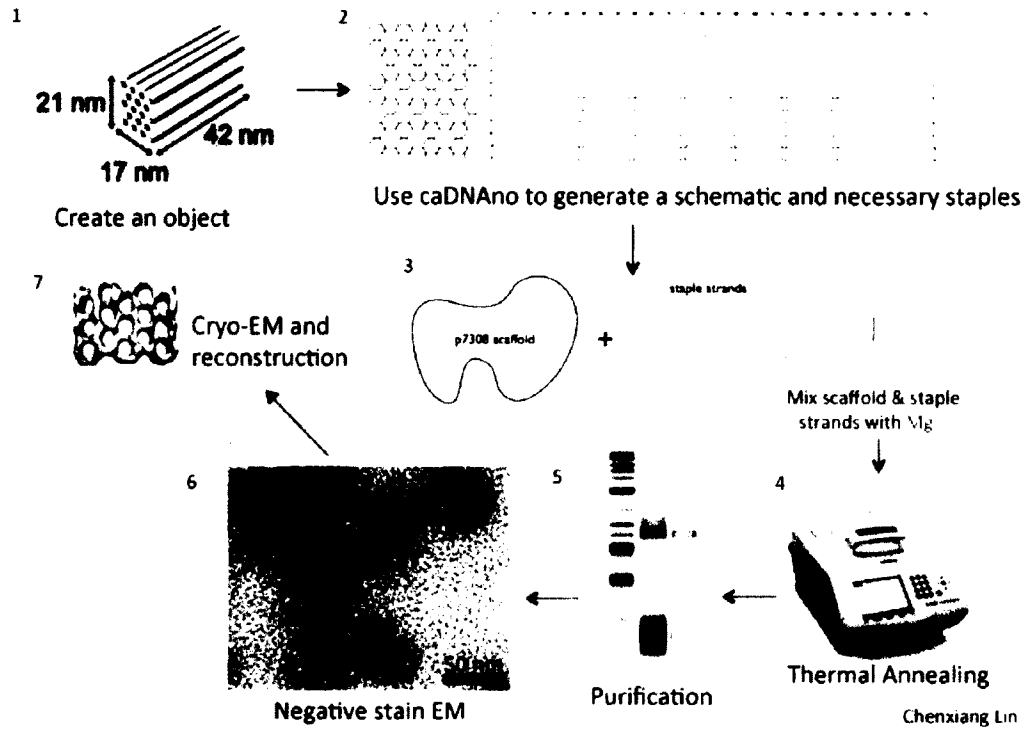


Figure 2.1 – General schematic of the conception and design using caDNAno, scaffold and staple annealing and purification, and final imaging of the product using negative stain EM and cryo-EM.

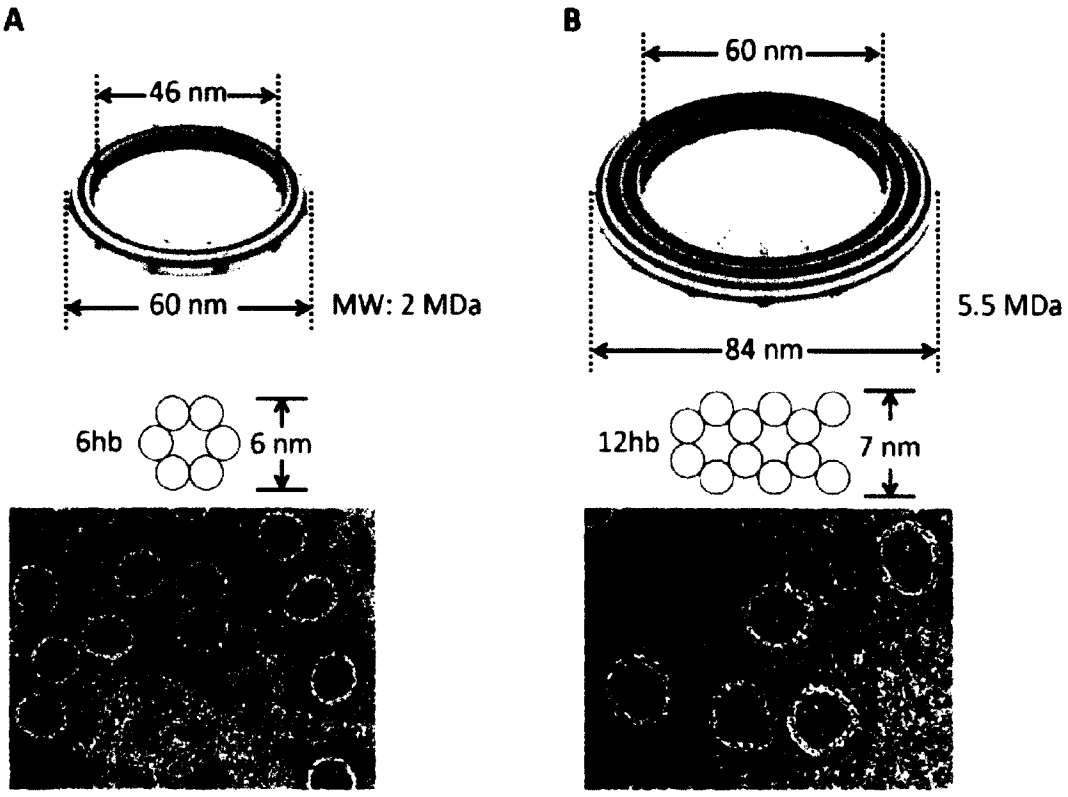


Figure 2.2- (A) 6 helical bundle origami ring (46 nm in diameter). (B) 12 helical bundle origami ring (60 nm in diameter). The second row shows their cross section and third row show the negative stain EM of both rings.

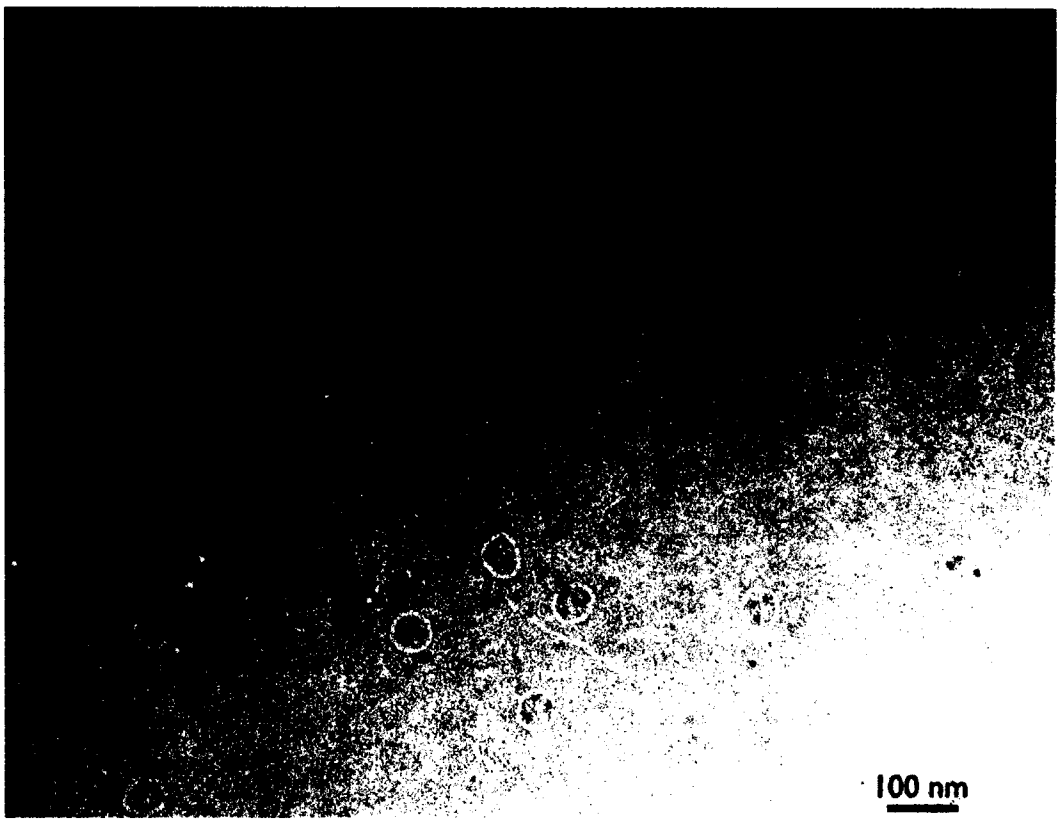


Figure 2.3 Selective attachment of gold nanoparticles AuNP on DNA Origami Ring using negative stain EM to demonstrate successful synthesis of the origami rings. The AuNP shows the location of the ring's inner handles and their correct inward orientation.

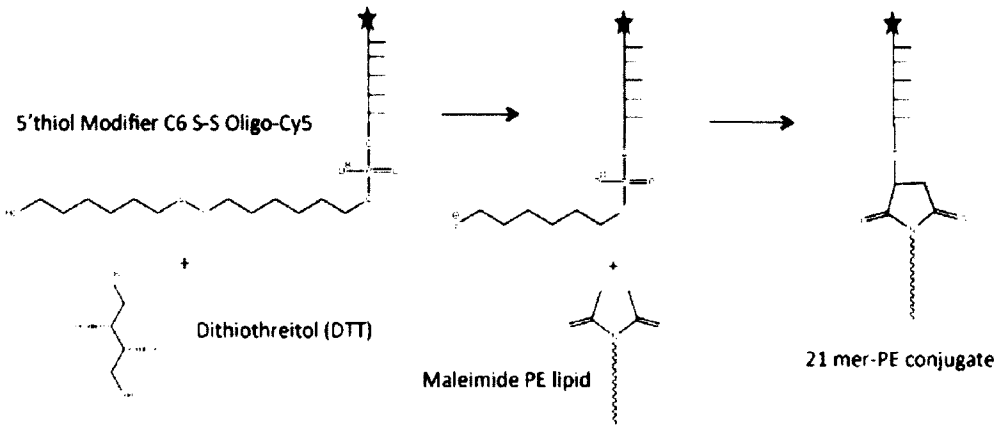


Figure 2.4 Synthetic schematic of the 21mer maleimide PE conjugate.

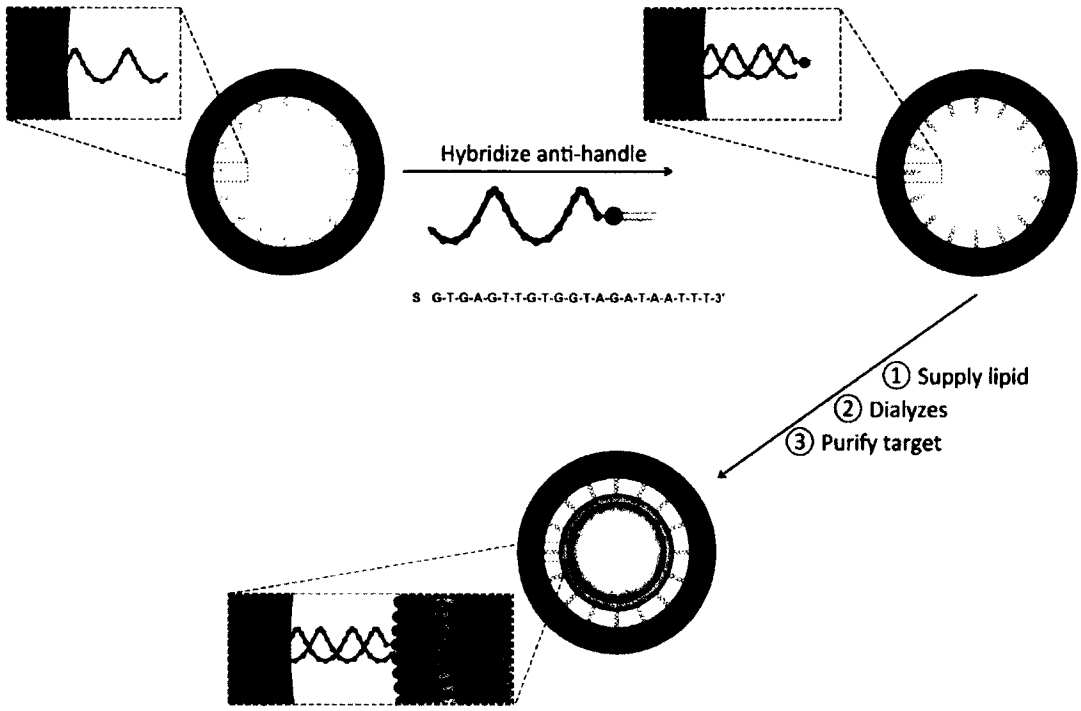


Figure 2.5 General scheme of Saturn formation. Once the ring complex is formed with hybridized anti inner handles, it is mixed with extruded liposomes, dialyzed and purified to obtain the final product.

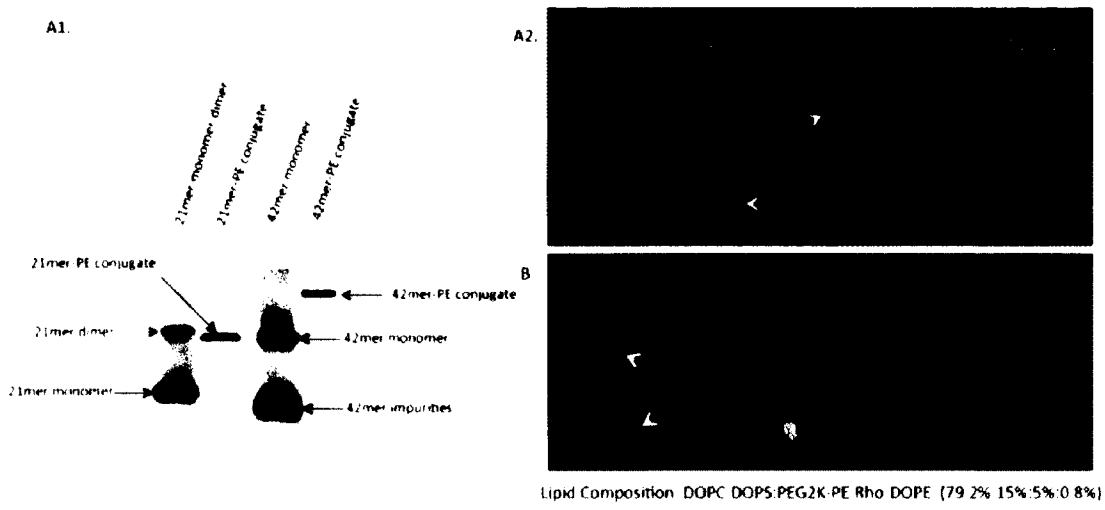


Figure 2.6 (A1) Coupling of thiol-Oligo-cy5 to Maleimide-PE: SDS gel confirms purity of desired products 21mer-PE and 42mer-PE. (A2) 6hb 3 inner handle iv ring complex: the red channel detects the existence of cy5-antihandle hybridized to the inner handles of the origami ring. Whereas, the green channel detects free rhodamine lipid mixture. A very clear separation is observed. (B) Incorporation of 6 hb 3 inner iv ring with 200 nm extruded rhodamine liposomes: The red channel detects cy5 signal located on the inner handles of ring complex. The green channel detects Rho premix liposomes. Coexistence of both red and green bands (frac 2) locates the fraction containing the Saturn vesicle.

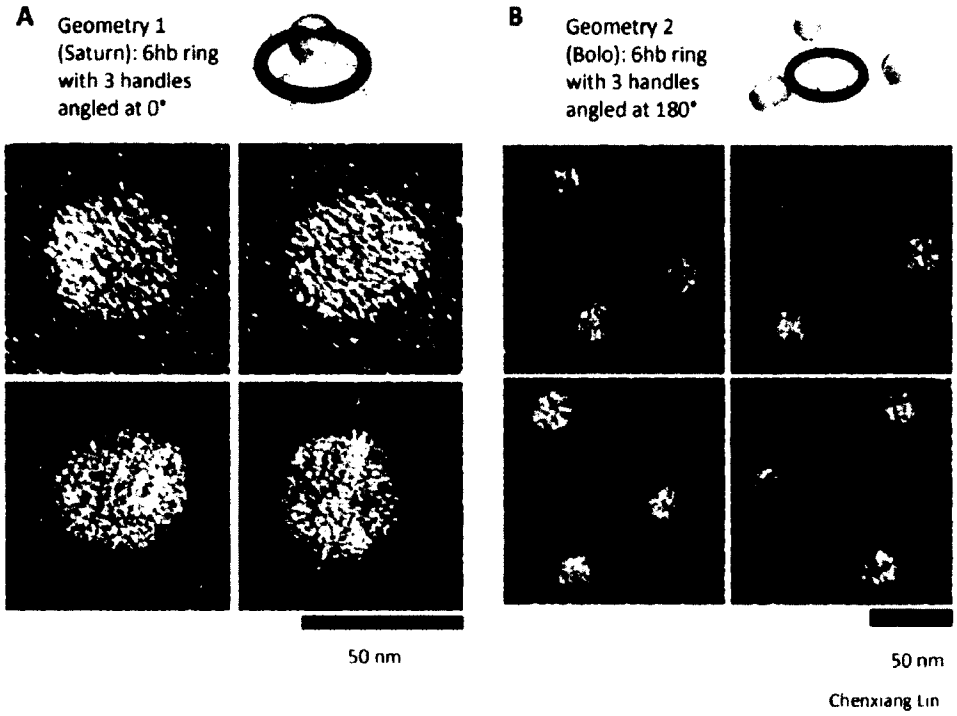


Figure 2.7 Negative stain EM of templated vesicles from (A) 6hb 3 inner handles at 0° and (B) 6hb 3 outer handles at 180°.

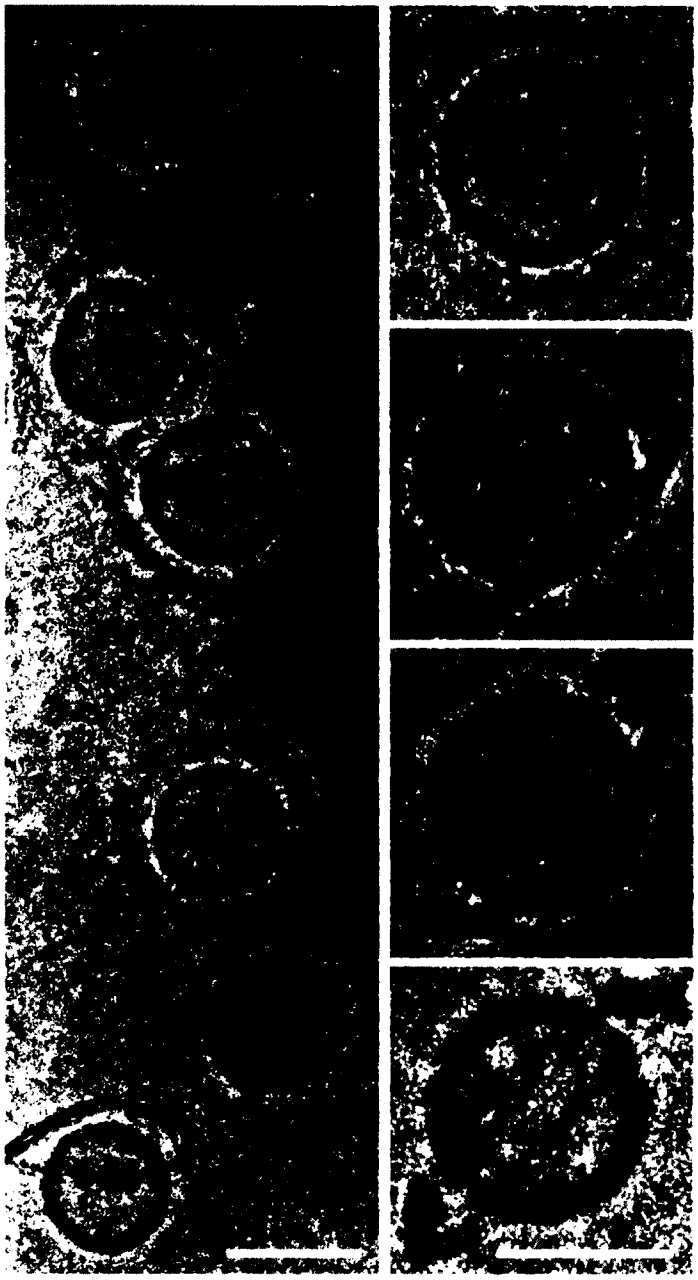

Figure 2.8 Cryo EM of 12hb 16 inner handle Saturn. The white scale bars are 50nm.

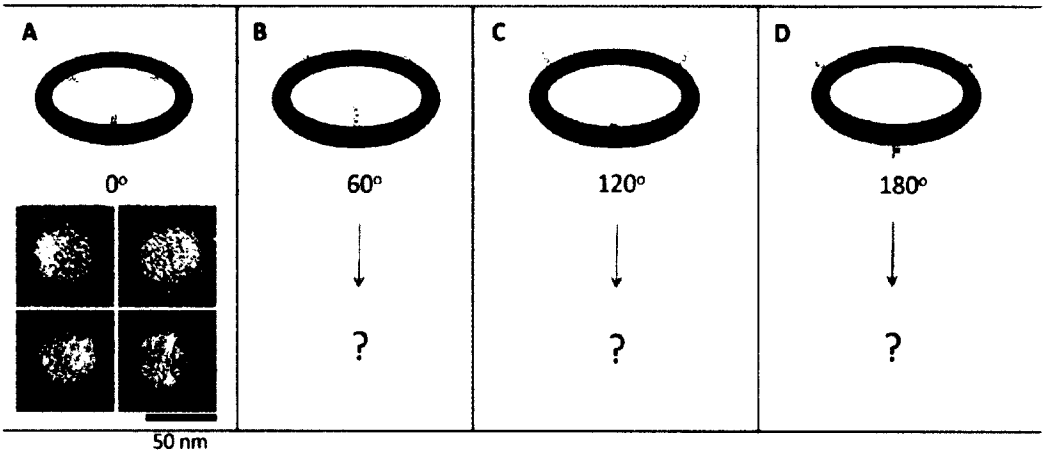


Figure 2.9 Design of 4 new rings with three angled handles at (A) 0° (B) 60° (C) 120° and (D) 180° to study their effect on templating lipids.

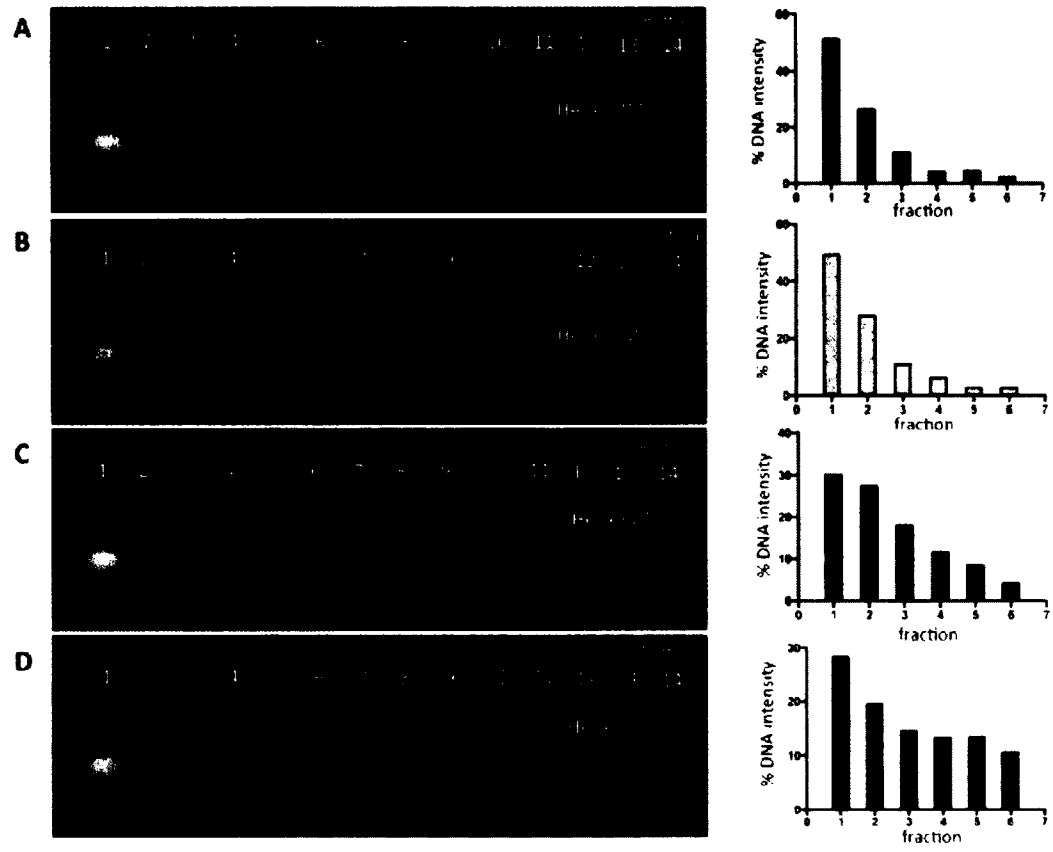


Figure 2.10 Each row shows the SDS agarose gel and the plot of % DNA intensity of fractions 1-7 for the pure product of the templated vesicle(s) from 6hb origami rings with three handles positioned at (A) 0° (B) 60° (C) 120° and (D) 180° to study their effect on templating lipids.

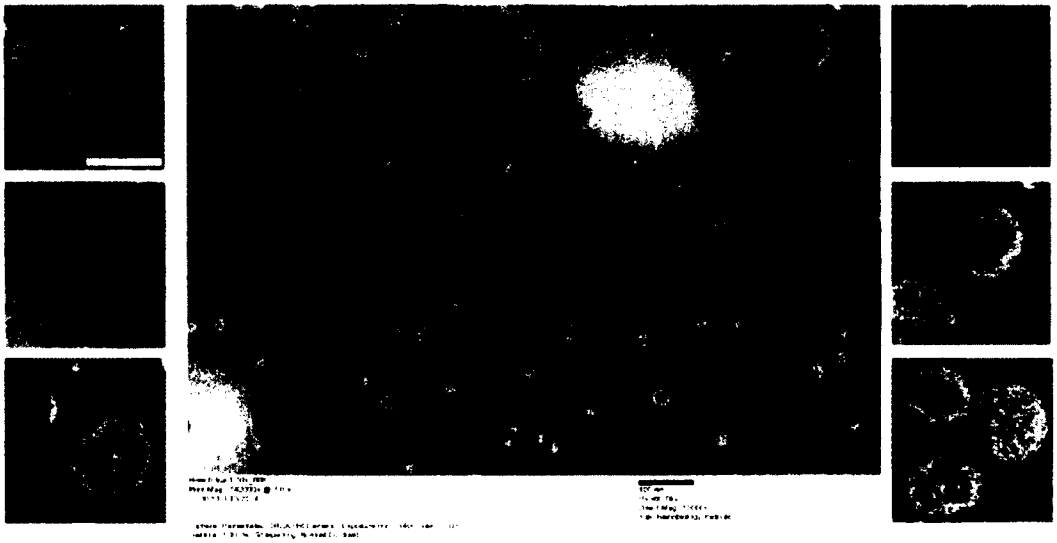

Figure 2.11 Negative stain EM of fraction 1 vesicles templated by 6hb origami rings with 180° handles. The white scale bar on the cropped images is 100 nm.

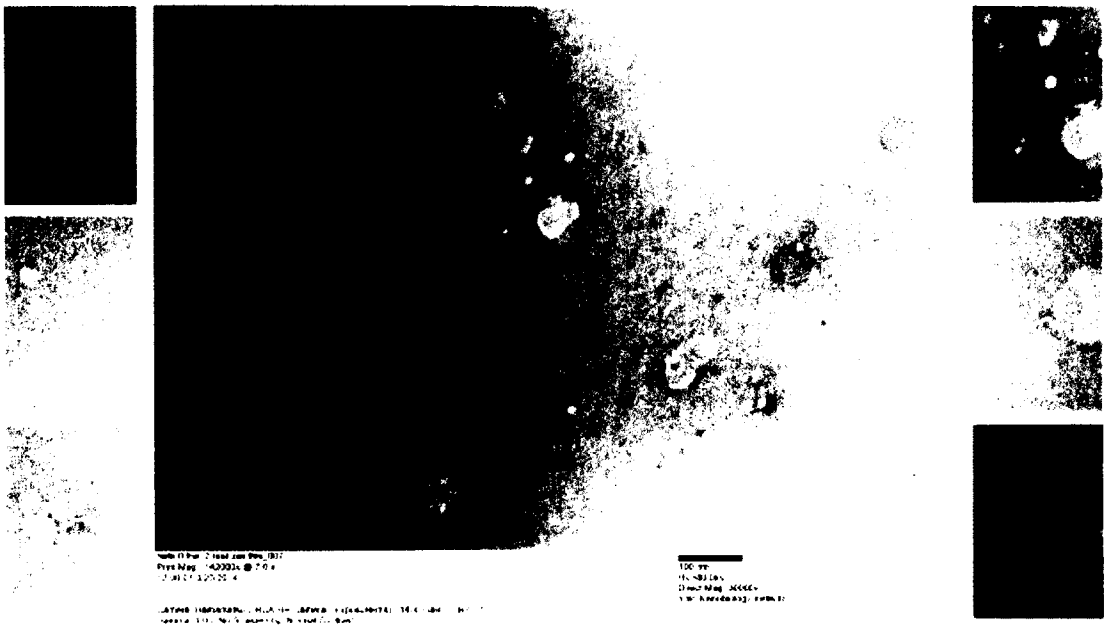

Figure 2.12 Negative stain EM of fraction 2 vesicles templated by 6hb origami rings with 180° handles. The black scale bar on the cropped images is 100 nm.

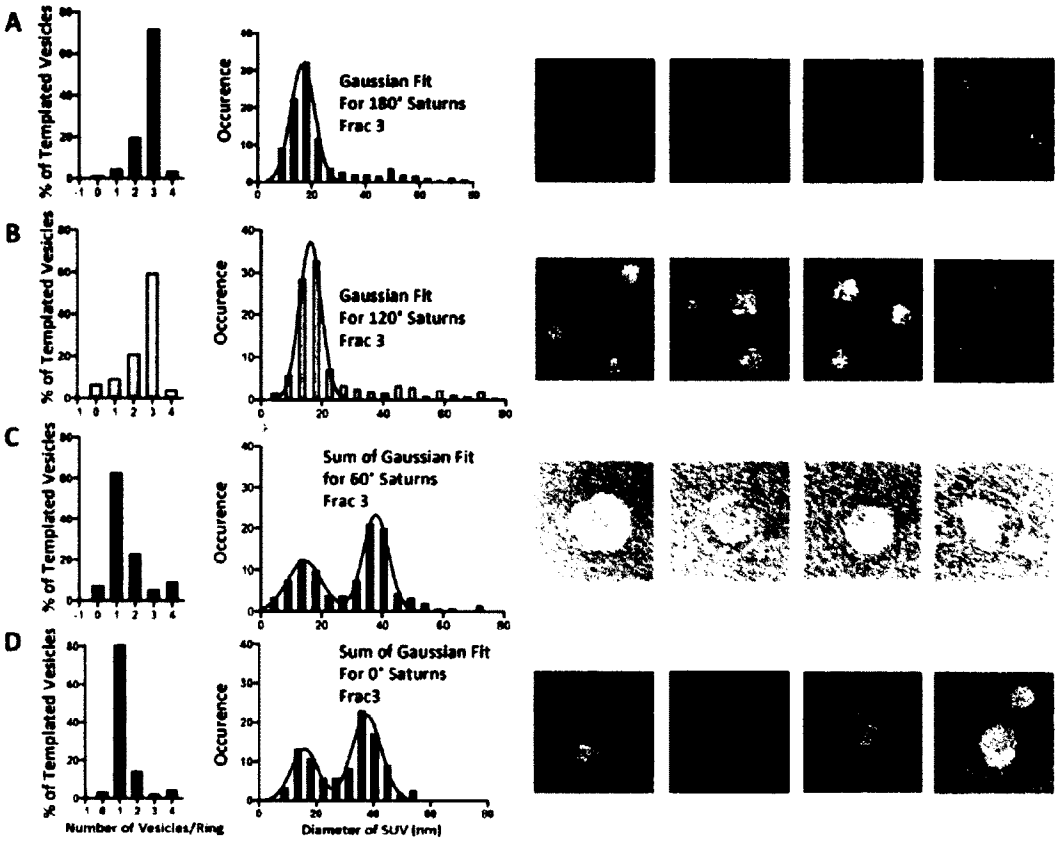


Figure 2.13 Templated Vesicles by Angled Handle Rings (A) 0° (B) 60° (C) 120° and (D) 180° in Fraction 3. The first column is a depiction of vesicle count per ring. Second column is the measure of vesicle diameters templated by the origami ring. And the third column is the negative stain EM of a few cropped structures from fraction 3, with each side 100nm x 100 nm.

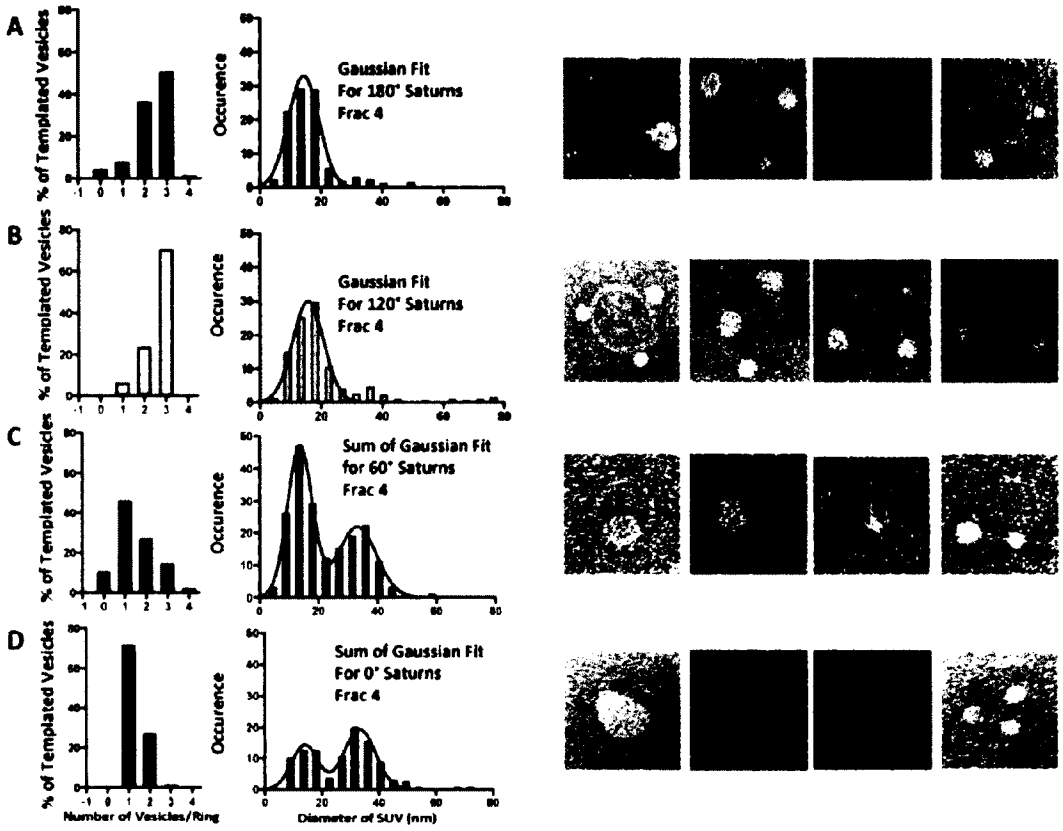


Figure 2.14 Templated Vesicles by Angled Handle Rings (A) 0° (B) 60° (C) 120° and (D) 180° in Fraction 4. The first column is a depiction of vesicle count per ring. Second column is the measure of vesicle diameters templated by the origami ring. And the third column is the negative stain EM of the a few structures from fraction 4, with each side 100nm x 100 nm.

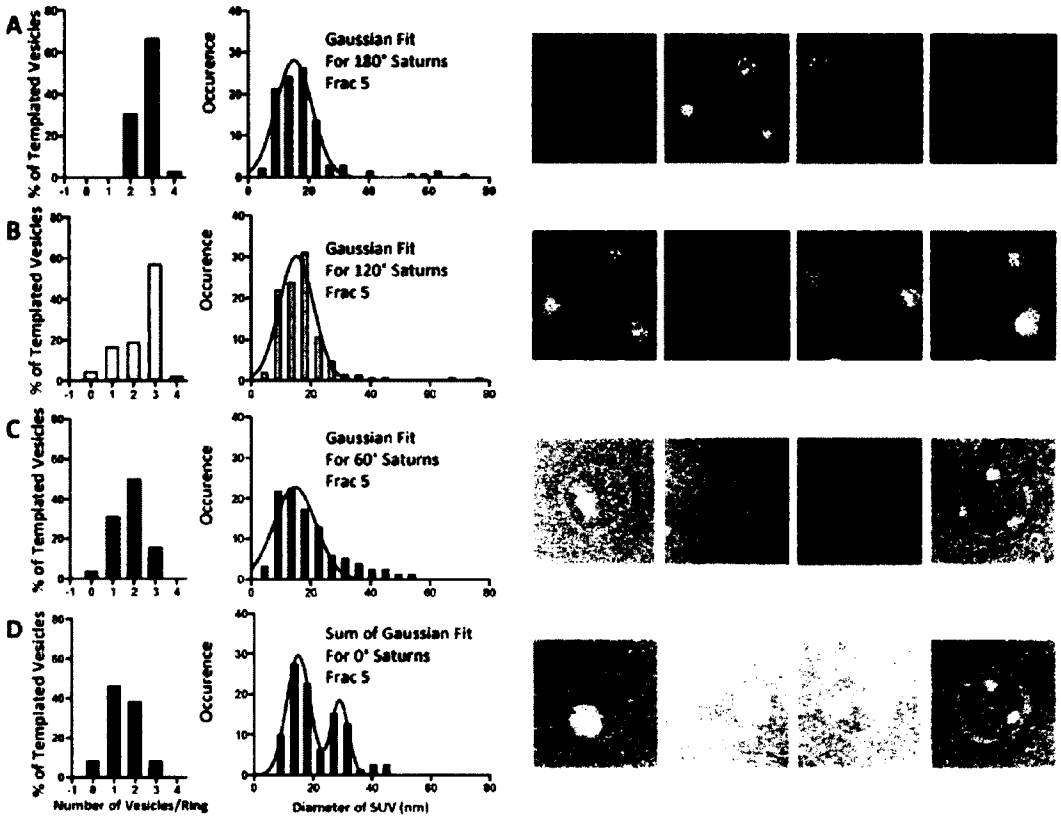


Figure 2.15 Templated Vesicles by Angled Handle Rings (A) 0° (B) 60° (C) 120° and (D) 180° in Fraction 5. The first column is a depiction of vesicle count per ring. Second column is the measure of vesicle diameters templated by the origami ring. And the third column is the negative stain EM of the a few structures from fraction 5, with each side 100nm x 100 nm.

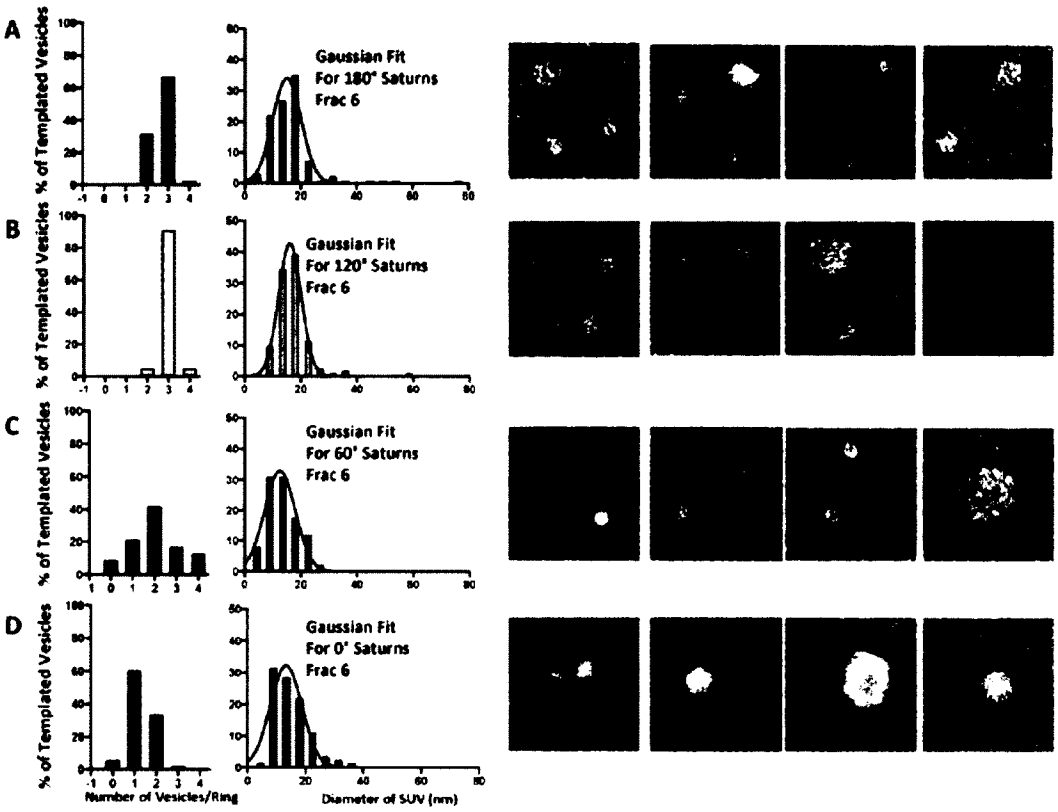


Figure 2.16 Templated Vesicles by Angled Handle Rings (A) 0° (B) 60° (C) 120° and (D) 180° in Fraction 6. The first column is a depiction of vesicle count per ring. Second column is the measure of vesicle diameters templated by the origami ring. And the third column is the negative stain EM of the a few structures from fraction 6, with each side 100nm x 100 nm.

## CHAPTER 3 - TEMPLATING VESICLE SIZE

Our results in previous chapter show that the DNA origami ring with 3 inner handle models the vesicle formation with the defined size that was directly controlled by the diameter of the DNA ring. The procedures we used in the formation and purification of DNA origami ring – vesicle complex involves 1) overnight dialysis to remove the detergent from the reaction mixture and 2) overnight centrifugation to purify the target products. Thus, the studies in this chapter were undertaken to first optimize our system with respect to the parameters described below and then to determine the mechanism underlying DNA origami ring templated vesicle formation. The extent of DNA origami ring – vesicle complex was determined in two ways: 1) agarose gel electrophoresis, and 2) EM imaging.

The 12hb origami ring with a diameter of 61nm was used in this chapter. Four-, eight-, or sixteen- inner handles with the sequence of 5'-AAATTATCTACCACAACTCAC-3' are located inside of DNA rings. The direction of these handles is 0° pointing towards the center of the ring. Again, a complementary 5'thiol modifier C6 S-S Oligo was ordered from Integrated DNA Technologies (IDT). The anti inner handle oligo sequence is 3'-TTTAATAGATGGTGTTGAGTG-5' designated as anti iv. The 5'thiol modifier reacts with dithiothreitol (DTT) and the thiol-Oligo-cy5 is coupled to 1,2-dioleoyl-*sn*-glycero-3-phosphoethanolamine-N-[4-(p-maleimidophenyl)

butyramide] (sodium salt) (Maleimide-PE). Furthermore, the ring contain X number of outer handles with sequences 5' –CTTCACACCACACTCCATCTA-3', which can hybridize to its complementary sequence containing the Cy5 dye, 3'-GAAGTGTGGTGTGAGGTAGAT-Cy5-5' that could serve as a reporter.

### 3.1 - Centrifugation Time and Density Gradient Measurements.

In the previous study, the dialyzed samples were centrifuged overnight at 50K, and 4°C and then individual fractions at different density of centrifugation media were collected for further analyses. To optimize the centrifugation time that yields greatest product, the dialyzed samples were centrifuged for 1hr, 2hr, 3hr, 5hr, 10hr, 15hr, and 20hrs. Further, in order to make comparison with our previous study, an overnight dialysis protocol and 6hb 3 inner handle ring system were used in this experiment. In addition, this experimental design also helped us address whether centrifugation is part of vesicle formation or simply purification of the final product

As shown in Figure 3.1, after 1 hr of centrifugation, there appears a cy5 peak at fraction 5 with a broad spread of products from fractions 1 through 12. After 2 hrs, the product seems to continue floating up with a majority at fraction 2 and a spread of cy5 intensity all the way to fraction 7. And after 3hrs and 5 hrs, the majority peak still stays at fraction 2, but the

signal is more concentrated to the top less dense fractions. The negative stain EM images show fully filled DNA origami rings at fraction 5 after 1 hr and 2hrs along with partially filled vesicles, ring-less vesicles, and empty rings. With 5hrs of centrifugation, the highest intensity peak at fraction 2 shows that majority of the products are fully filled DNA rings. We were surprised to find that fully filled vesicles were located in fraction 5 after 1 hr (Figure 3.2) and 2 (Figure 3.3) hours of centrifugation. This result revealed a critical detail that the product is completely formed after overnight dialysis, and that the centrifugation, not contributing to the vesicle formation, is simply separating the product from reaction mixtures based on density with ideal ultracentrifugation time at 5 hrs (Figure 3.4).

Centrifugation after 5hrs (Figure 3.5) result in a shift of both the cy5 (DNA) and cy3 (lipid) bands toward a denser fraction. This phenomenon is quite surprising. In the samples with centrifugation for 10, 15, and 20hrs, the majority peak of the cy5 band shifts to fraction 3, 4, and then 5. The cy3 band also has a shift from fraction 1 to 2 then 3. After 20hrs (Figure 3.6), the EM of fraction 5 reveals partially filled DNA rings. Ring concentration increased with smaller templated vesicles and decreased with larger templated vesicles.

In an attempt to explain the "shrinking" of vesicles in centrifugation longer than 5 hours, we measured the densities (Figure 3.7) of all the

fractions 1 through 14 during 1hr, 2hr, 3r, 5hr, 10hr, 15hr, and 20hrs of centrifugation. The refractive indices of the fractions were determined and converted to their corresponding densities. As shown in figure, between 5 and 20 hours, the density gradient in fractions 1-10 shifts downward. This observation corresponds to the shift in ring and lipid signal seen on the agarose gels.

These results in this section indicate that 5 hours of centrifugation is optimal, in which 50% of the fully formed Saturns are observed. We observe the maximum Saturn vesicle size obtained in fraction 2 after 5 hours of centrifugation time. The final Saturn product is obtained already after the dialysis. And ultracentrifugation is strictly serves as a means of separating various products into their respective fractions. There appears to be a loss of lipid and shift in the size of Saturn vesicles toward denser fractions when centrifugation times are longer than 5 hours.

**3.2 - OG/Lipid ratio: Varying Lipid to Detergent (OG) Ratio by Extruding Liposomes of 135.3 (0.5 nM), 23 (3 nM), 4.6 (15 nM) for 12 hb 4 Inner Handle Ring.**

Another attempt to optimize and understand the conditions, we varied the detergent to lipid ratio at 135.3 (0.5 nM), 23 (3 nM), or 4.6 (15 nM). The 12 hb 4 inner handle ring was used in this study. This ring

structure was of particular interest because it produced 2 distinct populations of products: fraction 2/3 (fully filled rings) and fraction 5/6 (partially filled rings). Its geometry has a diameter of 84 nm and a lower density of handles spaced at 48 nm, thus resulting in majority of products that are partially filled rings. As shown in figure 3.8, after purification, the two major peaks were observed in fractions 3 and 6. When the lipid concentration is lowered, there is a decrease in fully filled rings and an increase in partially filled rings. Thus, based on this study, the detergent to lipid ratio in future experiments will be 4.6 (figure 3.9).

### 3.3 - EM to Study the Mechanism of DNA-Origami Templated Formation of Liposomes

In order to fully elucidate the mechanism of formation of the Saturn structures, the intermediate structures were of importance in capturing. Dialysis is the most common method used in liposome formation. The crude mixture of lipid-detergent micelles is placed in a porous membrane and dialyzed against a detergent free buffer. The vesicles and micelles are so much larger in size compared to the detergent monomers that the former will be retained and the latter will be removed. We initially hypothesized that the complete formation of the templated vesicles occurs during the dialysis of OG and that the ultracentrifugation separates the crude product. To determine the removal of detergent, radioactive OG was used to study the

amount of detergent remaining at 0hr, 30 min, 1hr, 3hr, 5hr, and overnight dialysis. After 1 hr of dialysis, the detergent rapidly drops from 0.66% to 0.093% OG (equivalent to ~20% of original concentration) and after 3 hours, the detergent leveled out to back ground. As a result, intermediates were captured at 0hr, 30min, 1 hr, and overnight as means to interrogate the liposome forming mechanism. We performed such mechanistic study on 60-nm rings with different number of inner handles, systematically varying the initial number of lipid molecules anchored to the inside of each ring.

**12hb 4 Inner Handle Ring**: In figure 3.10, the first column shows the SDS agarose gel of all the fractions, the middle column displays several negative stain EM images from fraction 4, and the last column are plots of % DNA ring signal from the SDS agarose gel in the first column. For the 12hb 4 inner handle ring, at 0hr of dialysis, the purified products appeared in fractions 3-7. These fractions appeared as empty rings under the microscope (without noticeable attachment) (figure 3.11 and 3.12). The 0.66% OG and the iodixanol has an interaction on the grid that seems to burst the vesicles and prevent it from binding to the rings.

After 30 min dialysis, the spread of products floated up further and spanned fractions 1 through 7. In this case, 0.228% OG remained and was inserted among the lipid molecules. In fraction 2, a wide variety of templated structures were observed. First, a white lipidic thin layer formed along the inside of the DNA ring (mean thickness = 5.2 nm). Another structure

observed was a lipid/detergent mixture that wrapped around the DNA ring like a donut (mean thickness = 21.2 nm). A third structure was either a partially filled ring or chunky lipid aggregates that sits on one side of the ring. In fraction 3, the donut lipid/detergent mixture seems to be a dominant structure figure 3.13. In fraction 4, the majority product was the partial or complete spread of donut/detergent mixture along the inner lining of the DNA ring (figure 3.13). And in fractions 5,6, and 7 the similar spread was seen in addition to empty rings. It is believed that at this time point, micelles seeded at the ends of the handles and later non-specifically spread and bridged with neighboring micelles (Figure 3.14).

At 1hr, with 0.109% OG remaining, fraction 2 and 3 showed first signs of vesicle formation, with several SUVs inside the ring or with fully filled rings. A small population of rings fully filled with liposomes (Saturn-like structures) also began to emerge. In fraction 4, the SUVs (mean diameter = 18.1 nm) are smaller and further separated from one another. A few donuts and fully filled vesicles were also seen in this mixture (figure 3.15). In later fractions up till 7, we observed the similar trend of thin lipid/OG ring along with empty rings (figure 3.16).

After overnight dialysis and complete removal of detergent, fractions 2-4 revealed the templated SUVs and a higher population of fully filled vesicles than compared to fractions 5-7. The majority of the rings were either

fully filled with a single liposome or associated with a few separated vesicles, while a minority of rings remained empty (figures 3.17 and 3.18).

In addition to templated vesicles, another prominent observation was the development of non-templated micelles and later non-templated vesicles at 1hr and overnight dialysis. At 0hr and 0.5 hr, the excess lipids were dried during grid preparation and seem to burst in the presence of detergent.

**12hb 8 Inner Handle Ring:** In figure 3.19, the first column shows the SDS agarose gel of all the fractions, the middle column are negative stain EM images from fraction 4, and the last column are plots of % DNA ring signal from the SDS agarose gel from the first column. For the 12hb 8 inner handle ring, at 0hr of dialysis, the purified products appeared in fractions 3-7 with a DNA ring peak at fraction 6. As expected, these fractions appeared as empty rings under the microscope (figures 3.20 and 3.21).

At 0.5 hr dialysis with 0.228%OG remaining, the DNA ring peak was mainly seen in fractions 2 and 3. The former appeared as our donut structure whereas the latter stained the origami ring with an inner white lining of detergent/lipid mixture. These structures are primarily observed, because this system has a higher density of inner handles than the 4inner handle ring. The double density of handles on the DNA ring allows for greater specific capture and binding of vesicles. Fractions 4 through 7 reviewed of mixture of

products seen in fraction 2 and 3 but with more empty rings at higher density fractions (figures 3.22 and 3.23).

At 1 hr, with 0.109% OG remaining, fraction 2 and 3 revealed a majority of fully filled vesicles in addition to a few with a double inner lipidic membrane (mean diameter = 14.7 nm). This membrane was more prominently seen in fraction 4. We believe this is an inner donut with two bilayers (figure 3.24). And in fractions 5 through 7 with lower lipid content, again, a mixture of empty rings and inner lipid lined DNA rings were imaged (figure 3.25).

After overnight dialysis and complete removal of detergent, majority of the fully filled DNA rings appeared. Doubling the handle density promotes not only acceleration of the final Saturn structure but also a complete fully lipid vesicle inside the ring. Fractions 2 and 3 revealed a lighter grey vesicle sitting inside the ring. It grows to the size of the inner diameter but no larger than a darker grey DNA ring. Fraction 4 showed a similar structure however, gaps were observed between the outer border of the vesicle and the inner diameter of the ring. Also, seen are smaller vesicles that decorate along the ring (figure 3.26). The types of templated vesicles in fractions 5 through 7 are smaller vesicles that were decorated along inside the ring but were unable to fuse with the neighboring vesicles due to an inadequate amount of active handles (figure 3.27).

**12hb 16 Inner Handle Ring:** In figure 3.28, the first column shows the SDS agarose gel of all the fractions, the middle column is negative stain EM images, and the last column are plots of % DNA ring signal from the SDS agarose gel in the first column. For the 12hb 16 inner handle ring, at 0 hrs, we observed the usual DNA ring-lipid-detergent crude products to be separated into fractions 3-6, with the highest DNA ring intensity peak in fraction 6. Under negative stain EM, similar empty rings (as in 4- and 8-inner handle system) without any lipid attachment was observed (figure 3.29). After 30 min of dialysis, the product floated up to fractions 2 and 3 in which the DNA ring signal was strongest. Under negative stain EM, fraction 2 contained the white lipidic circular layer that forms along the inside of the DNA ring. This layer's structure was similar to those seen in the other ring systems, however, the thickness was slightly greater. Fractions 4 through 6 contained mostly the DNA rings bearing a thin circular strip of lipid, while the remaining few were of empty rings (predominantly observed in fraction 6) (figures 3.30 and 3.31). After 1 hr of dialysis, the agarose gel revealed the major DNA peaks in fractions 2 and 3. However, the negative stain EM displayed a different templated structure than the 30 min time point. Most of the structures were fully templated vesicles that consume the entire inside of the ring but don't grow past the edge of the ring. The other half of the products was the commonly seen lipid layer inside of the ring. This structure starts to show precedence in fraction 4 but slowly the population lowers

during fraction 5 and 6, in which more empty rings are observed (figures 3.32 and 3.33). Finally, after overnight dialysis, the DNA ring peaks are seen in fractions 2, 3, and 4. These contain mostly, fully filled Saturn structures with some partially filled structures (figures 3.34 and 3.35).

From the results presented above, it is clear that a variety of different lipidic structures can be formed in the presence of our DNA origami ring. However, until now, it is still of question whether the lipids are truly templated by the ring or whether non-specific interactions are occurring. To test that, we ran a control experiment using the 12hb 16 inner handle ring in absence of its coupled anti inner iv handle-maleimide PE lipid. Without using lipid anchors, we reacted the naked origami ring to our standard extruded 200 nm liposome mix and dialyzed the mixture at 0hr, 0.5hr, 1hr, and overnight. The crude mixture at each time point was purified by our standard iodixanol gradient centrifugation and 51 μL fractions were collected from the top to the bottom and ran on an SDS agarose gel. Figure 3.36 shows DNA ring (red) and lipid (green) peaks. For all four time points, the DNA ring and unbound outer handles containing the cy5 dye remained in fractions 7 through 11. However, the lipid signal spans fractions 1 through 6. This confirms that most of the DNA rings are unbound to any lipid and that the presence of a lipid anchor is vital for lipids to be templated by the DNA ring. Since the 16 inner handle ring, the densest system in terms of number of

handles per ring, was used in this control experiment, similar observations will be very likely to occur for the 4- and 8- inner handle rings.

### 3.4 - Discussion:

Three parameters were successfully addressed in this chapter: 1) centrifugation time and density gradients, 2) OG/Lipid ratio, and 3) dialysis conditions to capture intermediates of the Saturn formation. By addressing the effect of centrifugation times on Saturn structure, we were trying to answer two questions a) the optimal time that yields greatest product and b) whether centrifugation is part of vesicle formation or simply purification of the final product. Of all the times tested, 5 hrs of centrifugation produced the highest concentration of templated vesicles by the DNA ring in fraction 2. And after 5hrs, the product started separating toward the denser fractions. This suggested that there could be a shrinking effect on the templated vesicles, as by 20 hrs of ultracentrifugation, the majority DNA peak existed in fraction 5. And by negative stain EM, these rings contained a little vesicle inside of the ring. Thus, we speculate that DNA ring templated vesicles might not be stable under the centrifugation force for a longer period and that over time the fractions start to smear with one another. Further, we could also confidently state that the centrifugation contributes to separation of a crude product. Evidence that points to this include the existence of fully filled Saturn structures in fraction 5 after only 1 and 2 hours of centrifugation. This

suggested that very early on in the purification process, fully filled vesicles were already produced and were simply floating up to the less dense fractions as a means of separating from the other products.

The detergent to lipid ratio experiments were useful in allowing us to produce three extruded liposome concentration 0.5 nM, 3nM, and 15nM with ratios of 135.3, 23, and 4.6 respectively. The 12hb 4 inner handle ring was of particular interest because it produced 2 species of products: fraction 2/3 (fully filled rings) and fraction 5/6 (partially filled rings). This 4 inner handle ring geometry has a diameter of 84 nm and a lower density of handles spaced at 48 nm resulting in majority of products that are partially filled rings. Our data indicates that the ratio of 4.6 molecules of detergent to 1 molecule of lipid produced the highest percentage intensity of fully filled Saturn (fractions 2 and 3) and lowest of partially filled Saturn (fractions 5 and 6). Thus, the OG/lipid ratio of 4.6 should be used future experiments.

In order to fully elucidate the mechanism of formation of the Saturn structures, the intermediate structures were of importance in capturing (figure 3.37). Iodixanol was a great media here because it occurs rapidly and doesn't need extended ultracentrifugation time or salt density adjustment. This makes this process superior to sequential floatation ultracentrifugation (SFU) and salt gradient systems [108-112]. We were able to achieve rapid separation and preparative sub-fractionation in a single run using our 7-

layer self generating continuous density gradient. Once the crude templated Saturns come close to their isopycnic density after ultracentrifugation in the density gradient, the purification was complete and the fractions were identified on the SDS agarose gel. For all three of the ring structures, at 0 hrs (0.66% OG) of dialysis, the products do not float up past fraction 3. However, fractions 3-7 displayed empty rings on negative stain EM. This observation that the ring does float up to fraction 3 indicates that the ring is bound with lipidic structures, which is high in detergent amount. If the coexistence of iodixanol and high detergent concentration were creating an obstructing interaction that burst any lipidic structures formed by the ring, the ring would stand-alone positively stained.

At 30 min (0.228% OG), the lipids seem to have seeded small micelles (different detergent-lipid mixture than at 0hrs) at the ends of the handles and then started bridging among its neighboring micelles into the two structures of a thin circular lipidic paste along the inside of the ring and a lipid mixture that wraps around the ring (fractions 2-4). At this point, because the detergent concentration is still high, there is an interesting dynamic in solution where the OG impacts the constant changing of the structures, therefore making it difficult to capture exactly one intermediate structure. Fractions 5 though 7 contain fewer lipid molecules thus, the products are partially filled versions of the thin circular lipid ring, with higher populations of empty rings as we move towards denser fractions.

At 1 hr (0.109% OG), with additional detergent removal, we believe that the resultant gaps in the lipidic structure are filled in with nearby lipids and the first signs of vesicle formation is observed. Fractions 2 and 3 reveal a new fully filled Saturn structure, but the population increases as the density of handles increase. At this point, the rate of forming fully filled Saturns increases as the number of handles increase. If vesicles seed at the handles and later fuse with its neighbors, the closer the proximity of the handles are to one another, the quicker and more likely the neighboring vesicles will fuse. At this same time point, fraction 4 generated a variety of interesting intermediates. In the 4- inner handle ring, we observe a variety of small vesicles positioned where some of the handles are in addition to fully filled rings and rings with a thin lipidic layer. The first intermediate provides a solid templating evidence of the ring that little vesicles nucleate (seed) at the ends of handles and then later fuse with its neighboring vesicles to form a larger vesicle. In the same fraction for the 8- inner handle system, we observe another critical intermediate, the lipid-bilayer torus inside the ring. This structure can be interpreted as the fusion structure of many neighboring small vesicles that cannot stand on their own in high handle density rings because the close proximity spontaneously forces the vesicles to fuse. In fractions 5-7, the obvious result of fewer lipid molecules per ring is observed in which the population of empty rings increases in denser fractions. After overnight dialysis and complete removal of detergent, all the final structures

are of varying size vesicles templated by the ring, and the smaller templated structures are found in the more dense fractions of the gradient. In the 4-inner handle system, although fully filled Saturns are seen, most of the structures are partially filled rings. However, it is due to the increase in handle density that the population of fully filled structures increases dramatically, especially when comparing the 4- and 16- inner handle final products.

We further looked at our 4 intermediate structures and our final fully filled Saturn product and measure the thickness of the lipid (figures 3.38 and 3.39) to calculate for number of lipids templated in each intermediate.

**Circular Thin Lipidic Layer:**

$C_{micelle} \times C_{Donut}$

$=[3.14 \times 5.2nm] \times 3.14 \times [60nm - 5.2nm]$

$=2860.9\ nm^2$ or **4,207 lipids**

**Seeded SUVs Intermediate:**

$4 \times (SA_{out} + SA_{in})$

$= 4 \times 4 \times 3.14 \times [R_{out}^2 + R_{in}^2]$

$$= 4 \times 4 \times 3.14 \times \left[\left(\frac{18.1nm}{2}\right)^2 + \left(\frac{18.1nm - 10.4nm}{2}\right)^2\right]$$

$=4859.3\ nm^2$ or **7,146 lipids**

**Lipid-Bilayer Torus:**

$SA_{outer} + SA_{inner}$

$= \pi[D_{out} + D_{in}] \times [\pi \times (61\ nm\text{-}14.7nm)]$

$=3.14 \times [14.7nm + 14.7nm - 2 \times 5.2nm] \times 3.14 \times (60\ nm - 14.7nm)]$

$=8673.5\ nm^2$ or **12,755 lipids**

**Outer Donut (Continuous Bilayer):**

$(P_{out} + P_{in}) \times (\pi \times D_{ring})$

$=[(21.2nm \times 2 + 18.1nm \times 2) + (10.8nm \times 2 + 7.75nm \times 2)] \times 3.14 \times 71nm$

$=25794.2\ nm^2$ or **37,933 lipids**

**Fully Filled Saturn Structure:**

$SA_{out} + SA_{in}$

$=4 \times 3.14 \times [\ (28.8\ nm)^2+(26.2\ nm)^2]$

$=19{,}039.4\ nm^2$ or **27,998 lipids**

From these calculations, the thin circular lipidic bilayer intermediate contains the fewest number of lipids, consistent with the facts that this structure is prevalent earlier in the dialysis (0.5 hr) or that in denser fractions of the gradient during 0.5 hr and 1 hr of dialysis. Thus, in these cases, the accumulation of templated lipids onto DNA origami shall be still low. For the seeded SUVs intermediate and the lipid bilayer torus intermediate observed after 1 hr of dialysis in 4- and 8- inner handle rings respectively, a double in the number of lipids was observed, as expected since the lipid anchor molecules are doubled in 8- inner handle ring as well or the dialysis time is 1 hr in case of 4- inner handle ring. Interestingly, the outer donut (occurs at 0.5 hr of dialysis, fraction 2 or 3) contains more lipids than the fully filled structure, probably due to the fact that the outer donut

wraps completely around the entire ring. Furthermore, the outer donut structure exists because of the high content of detergent gluing all the lipids together forming detergent-lipid structures on the DNA ring surface.

### 3.5 – Method and Material

If the ring sample were assembled in a batch larger than 200 µl (normally 400 or 800 µl), we use a size exclusive tube with 3kD pore size film (Amicon Ultra 0.5ml,Merck Millipore Ltd.) to concentrate it into 200 µl. Then we loaded the 200 µl sample on top of a 15%-45% v/v glycerol linear gradient in a polycarbonate centrifuge tube (13x 51 mm, Beckman Coulter Inc.), and centrifuged at 50k rpm (time request see above table) on a SW 55 rotor in the Optima XE-100 Ultracentrifuge (Beckman Coulter Inc.). The tube was then fractionated from top to bottom with 200 µl/layer steps.

Each fraction (4 µl) was then loaded into a 1.5% agarose gel with ethidium bromide pre-added and run 90 min under 60 V potential. The gel was then scanned by Typhoon Scanner (Typhoon FLA 9500, GE Healthcare).

Taking one typical gel of the 60 nm-Ring as an example (figure 3.40), most of the extra staples were kept in the top fractions (F1- F4) while DNA aggregates shifted further to the bottom (F9-F15). We collect fraction 6 and 7, which contain pure DNA Ring products, combine them and concentrate the product through the 3kD Amicon filter with 3 times buffer wash to remove

glycerol. Product concentration was then evaluated by NanoVue Plus Spectrometer (GE Healthcare) and adjusted to 50 nM using buffer.

Two rings were produced for this thesis. The 47nm - 6 helical bundle (6 hb) and 61 nm -12 helical bundle (12hb) ring. The 6hb ring has 3 inner handles with sequence 5'-AAATTATCTACCACAACTCAC-3'. And the 12hb ring has 4-, 8-, or 16- inner handles with sequence 5'-AAATTATCTACCACAACTCAC-3' and 8 outer handles with sequence 5'–CTTCACACCACACTCCATCTA-3'. Furthermore, anti outer handles with sequence 3'-GAAGTGTGGTGTGAGGTAGAT-Cy5-5' was ordered from Integrated DNA Technologies (IDT).

**DNA Ring Assembly:**

All staple strands were purchased from Integrated DNA Technologies Inc. in the format of 96-well plates at a 25 nmol synthesis scale. All the strands were normalized to 100 μM and were used without further purification. Genetic engineered M13 DNA was used as scaffold, and several different lengths were chosen for different sized rings as listed in the Table 3.1. All the rings were assembled in a 50 nM scale (scaffold concentration) with 6 times of molar excess staple strands (300 nM) in 1x TE $Mg^{2+}$ buffer (5mM Tris• HCl, 1 mM EDTA, 10 or 12 mM of $MgCl_2$,pH 8.0) following a 36 hours annealing: 80℃ ~65℃ 5 min/ ℃; 64℃~ 24℃ 50 min/ ℃; 15℃ hold.

Oligo-lipid conjugates serve as the main anchoring units that allow lipid structures to seed on the DNA ring templates. Two methods of Oligo-Lipid conjugate synthesis were reported here. In the first protocol, a 5'thiol modifier C6 S-S Oligo-Cy5 was ordered from IDT. On this molecule, a cyanine dye (Cy5), containing a hydrophilic sulfonate group, was used to label the 3' end of the nucleic acid. The anti inner handle oligo sequence was 3'-TTTAATAGATGGTGTTGAGTG-5' and we designated as anti iv. In the second protocol, 5'thiol modifier C6 S-S Oligo without a Cy5 on the 3' end is ordered from IDT. In this method, the Cy5 is labeled on the 5' end of the anti outer handle.

**Synthesis of Oligo-Lipid Conjugates (Antihandles):**

*Protocol 1 (cy5 linked to oligo):*

The 1,2-dioleoyl-*sn*-glycero-3-phosphoethanolamine-N-[4-(p-maleimidophenyl) butyramide] (sodium salt) (3uL, 1mM) (Maleimide-PE) and stock lipid mix of DOPC:DOPS:PEG2K-PE:Rho-DOPE (79.2%:15%:5%:0.8%) (10.7 uL, 28 mM) were dried down under vacuum for 1hr and 2 hrs respectively. Then, 20 uL of 5'thiol modifier C6 S-S Oligo-Cy5 (500 μM) reacted with 2 uL of dithiothreitol (DTT) (100 mM) for 1 hr at room temperature (RT) and the mixture was passed through a biospin micro P6 column containing buffer A (25 mM HEPES, 140 mM KCl, 0.17 mM TCEP).

The collected product then reacted with 10 μL of 10% OG (in 25mM HEPES, 400 mM KCl) instantly at room temperature. The total volume was adjusted to 100 μL using 25 mM HEPES, 140 mM KCl, 0.17 mM TCEP buffer and then added to the dried Maleimide-PE. The mixture was vortexed at RT for 30 min. and then stood at room temperature for another 30 min. The β-mercaptoethanol (10 μL, 0.14 M) was added and the new mixture stood at room temperature for 10 min. And the reaction mixture was finally added to the dried stock lipid mix and vortexed for 15 min RT. Before dialysis, 200 μL of buffer A was added and Slide-A-Lyzer dialysis cassette (7,000 MWCO, 0.1-0.5 mL capacity) against 2L buffer A with 2 g of Biobeads SM2 adsorbent media occurred at RT overnight.

An iodixanol gradient was used to purify the coupled product. In this gradient, the bottom layer consisted of 150 μL of dialyzed sample and 150 μL of OptiPrep (Sigma D1556, 60% iodixanol in water). The bottom layer was then overlaid with a 250 μL of 20% iodixanol middle layer and the top layer contains 50 μL of buffer A. The SW55 tubes were finally spun at 50K, 4°C, 5hrs-overnight Beckman Coulter SW55 Ti bucket. The liposome band (labeled by the pink rhodamine dye) was collected. In order to detect the purity of our final product, a precast Sodium Dodecyl Sulfate-Polyacrylamide Gel Electrophoresis (SDS-PAGE) from Novex (lot 14053072) was run with the first lane containing the standard ladder, second lane containing deprotected 5'thiol modifier C6 S-S Oligo-Cy5, and the last lane containing

our final product. The gel was scanned Typhoon FLA 9500 (typhoon scanner) at 647 nm and 532 nm for detecting the coupled product and the vesicle.

*Protocol 2 (oligo without dye):*

The buffers used in this conjugation were buffer B (140 mM KCl, 25 mM HEPES.KOH, pH 7.4), and 10x (1400 mM KCl, 250 mM HEPES.KOH, pH 7.4). First, the lipids in chloroform were blown dry under $N_2$ gas and then dried in a vacuum overnight using two glass test tubes: 1) 400 μL 1mM Maleimid-PE (400 nmole in total), and 2) 18 μL of 30 mM DOPC + 8 μL of 1mM Rho-PE (600 nmole in total).

In order to reduce the Di-thiolated DNA with TCEP, 20 μL of 1 mM (R-S-S-)-5'/3'-antihandle (20nmole in total), 5μl of 500mM TCEP, 5 μL of 10x reaction buffer and 10 μL of $H_2O$ were mixed together so that the final concentration was 25 mM HEPES, 140 mM KCl, 50 mM TCEP, pH 7.4 and the reaction runs at RT for 30 min. In the crosslinking reaction, 5 μL of 20% OG, 5μL of 10 x buffer and 40 μL of $H_2O$ were added to the thiolated DNA so that the final volume is 100μL with 1% OG and this mixture was transferred to tube 1. The tube was vortexed and stood at RT for 45 min and 30 min respectively. Then, the contents of tube 1 was transferred to tube 2 and vortexed at RT for 30 min, and then diluted by three fold. The final mixture

was transferred to the dialysis cassette and dialyzed against 2L buffer B at RT overnight.

From the dialysis cassette, 300 μL of liposome was recovered and mixed with 300 μL of OptiPrep (Sigma D1556, 60% iodixanol in water) media, resulting in a 30% OptiPrep solution layer containing our crude product. The bottom layer (300μL) was overlaid with 250 μL of 20% iodixanol middle layer and the top layer contains 50 μL of buffer A. The SW55 tubes were finally spun on the Beckman 90K floor centrifuge 50K, 4°C, 5hrs and lastly 50 μL for each fraction was collected from top to bottom. For the characterization, a SDS-PAGE gel of the liposome (20V/cm, 30 min) was run and stained the gel with SYBR-Gold. The correct product with highest yield appeared in fraction 2. To calculate product concentration, the intensities of bands were compared with those of DNA only references.

**Formation of the Ring Complex:**

*Without Purification:* In order to hybridize the anti handles onto the DNA ring, the final concentration of the ring was adjusted to 10 nM. The moles of 5'DNA-lipid inner anti iv was 5x the number of handles to one origmai ring. And the Cy5-outer anti ii was 12x to one origami ring. The detergent Octyl β-D-glucopyranoside (OG) was adjusted to 1% and the buffer was adjusted to buffer C (25mM HEPES, 400 mM KCl, and 10 mM $MgCl_2$). The reaction was

incubated at 37°C for 1 hr and then lowered to a 12°C hold. Following this same protocol, a control ring complex was also formed in the absence of 5'DNA-lipid inner anti iv.

*With Glycerol Purification:* The preparation of the ring complex will result in a final volume of 50μL with 10% glycerol and ring complex concentration of 6nM. So an equivalence of 1:20 of ring complex to Cy5-anti iv-PE was maintained with the final buffer adjusted to 25 mM HEPES, 400 mM KCl, 10mM $MgCl_2$, 10% glycerol, and 1% OG. Before adding the ring, the mixture was vortexed for 15 min. Once the ring was added, the reaction mixture was incubated at 37°C for 1.5hrs. The glycerol step density gradient, prepared the night before, consists of 12 layers: from bottom to top-60%, 40%, 37%, 34%, 31%, 28%, 25%, 22%, 19%, 16%, 13%, and 10% of glycerol in buffer C.

After 1.5hrs, the ring complex mixture was added to the top of the glycerol gradient and centrifuged for 50K, 4°C, 1hr 15min (for 12hb ring, decelerating slowly) or 3hrs (for the 6hb ring). A 50 uL fraction was collected down the tube and loaded onto a SDS Agarose gel (1.5 agarose gel concentration in 0.5x Tris/Borate/EDTA buffer with 10 mM $Mg^{2+}$ and 0.05% SDS) for product identification. The gel was run at 65 V for 2.5 hrs and scanned on a typhoon scanner at 647 nm for the DNA ring and 532 nm for the liposome. Typically fractions 6 and 7 (which has the highest pure

intensity of the DNA ring) were combined for reaction with the extruded liposome.

**Formation and Purification of Final Saturn Product:**

The ring and antihandles were mixed with 15mM extruded lipid DOPC:DOPS:PEG2K-PE:Rho-DOPE (79.2%:15%:5%:0.8%) and buffer C in a ratio of 2:1:1 and vortexed at RT for 1 hr. This was further diluted by adding one molar equivalent of buffer C containing 0.66% OG and transferred to a dialysis cassette (7k-0.5mL) for overnight dialysis against bucket with buffer B.

Two iodixanol gradients had been used in this thesis. First, a three-layer iodixanol gradient was prepared with a gradient consisting of 30% iodixanol with sample on the bottom layer, 20% iodixanol middle layer, and 0% iodixanol in the top layer. These were all in the presence of buffer C. Second, a seven-layer iodixanol gradient was used for centrifugation with a gradient consisting of 30% iodixanol with sample on the bottom layer and top layers of 26%, 22%, 18%, 14%, 10%, and 6%. The samples were centrifuged at 50K rpm, 4°C for 5hrs and 51 μL fraction was collected and identified on an SDS agarose gel. The gel was scanned at 647 nm and 532 nm to identify the fractions with DNA ring and with vesicle.

**Radioactive OG experiments:**

In preparing the reaction of the Saturn structure using radioactive OG, 240 μL of the ring complex containing 1 % OG was mixed with 60 μL of extruded liposome (15mM), 60 μL of buffer C, and 1.8 μL of OG-$C^{14}$ source. The reaction was vortexed for 1 hour and 10 uL was removed from this mixture, diluted 5x with dialysis buffer C, and mixed with 18 mL of scintillation cocktail (opti-fluor, cat # 6013199 PerkinElmser). The resulting mixture was measured on the Beckmann Coulter LS6500 Multi Purpose Scintillation Counter to obtain the $C^{14}$ count/minute and this was obtained at 0hr time point. The mixture was then diluted with 411.04 μL of buffer C (containing 0.66% OG) and split into 5 cassettes for dialysis and for measuring the amount of detergent remaining after 0.5hr, 1hr, 3hr, 5hr, and overnight. After each time point, 50 μL of the dialyzed product was mixed with 18 mL of the scintillation cocktail and the $C^{14}$ count/minute was measured.

**Preparation of 2% Uranyl Formate (UF) Stain :**

Boiling water (1mL) was added to 20 mg of uranyl formate hydrate (CAS # 16984-59-1) and the eppendorf tube was covered in foil and strongly vortexed for 5 min. The solution is then filtered through 0.2 μm pore and 800

μL of it is added to 4uL of 5M NaOH. The resultant mixture was spun down in Eppendorf Centrifuge 5424 at 21120 rcf for 5 min.

**Prepare Negative Stain EM Grids:**

Our samples for imaging were prepared on FCF400-Cu FORMVAR carbon film grids. We discharged the grids at 25mA for 30 sec. and then 5 μL of sample was deposited onto the grid for 5 minutes. The sample was removed and the grid was washed with 5 μL of the UF stain. Then, 5μL of the stain was deposited onto the grid for 1 minute. For fractions denser than fraction 3, we added an extra 5 μL buffer wash before the stain wash. For intermediate structures, all the buffers and stain were adjust with 0.66% OG (at 0hrs), 0.23%OG (at 0.5hr), and 0.11% OG (1hr). All grids were imaged through the JEM-1400 scope.

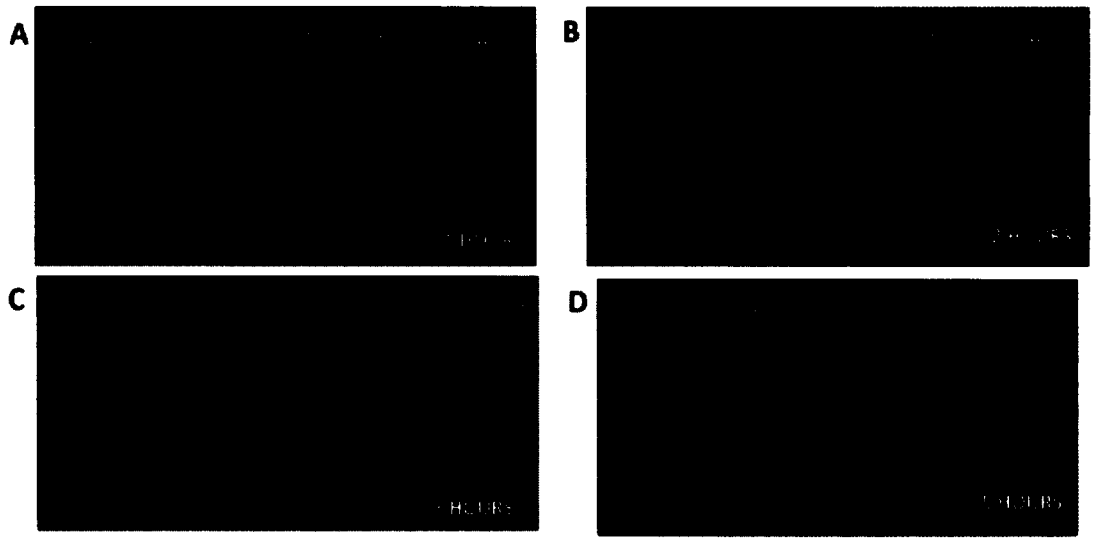


Figure 3.1 - SDS Agarose Gel of crude Saturn product after overnight dialysis at (A) 1hr (B) 2hrs (C) 3hrs (D) 5hrs of ultracentrifugation.


Figure 3.2 - Negative stain EM of Saturn product in fraction 5 after 1 hr of ultracentrifugation.

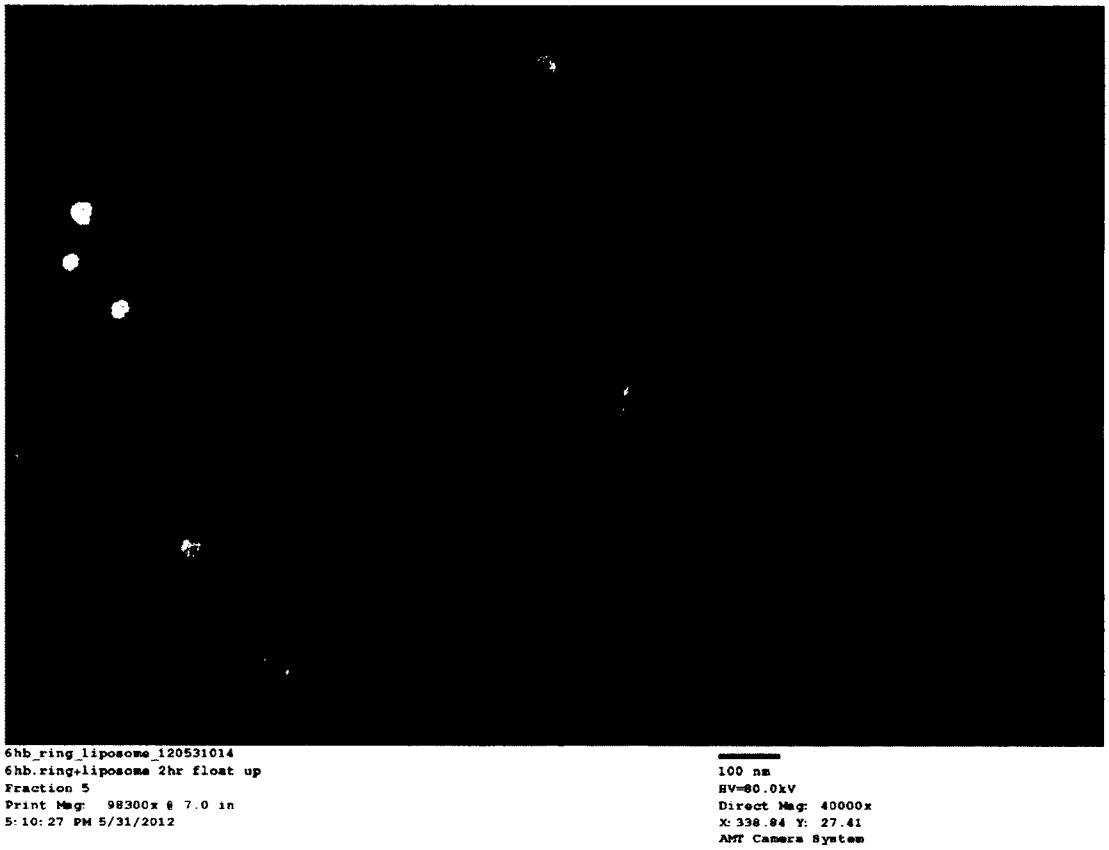


Figure 3.3 - Negative stain EM of Saturn product in fraction 5 after 2 hr of ultracentrifugation.

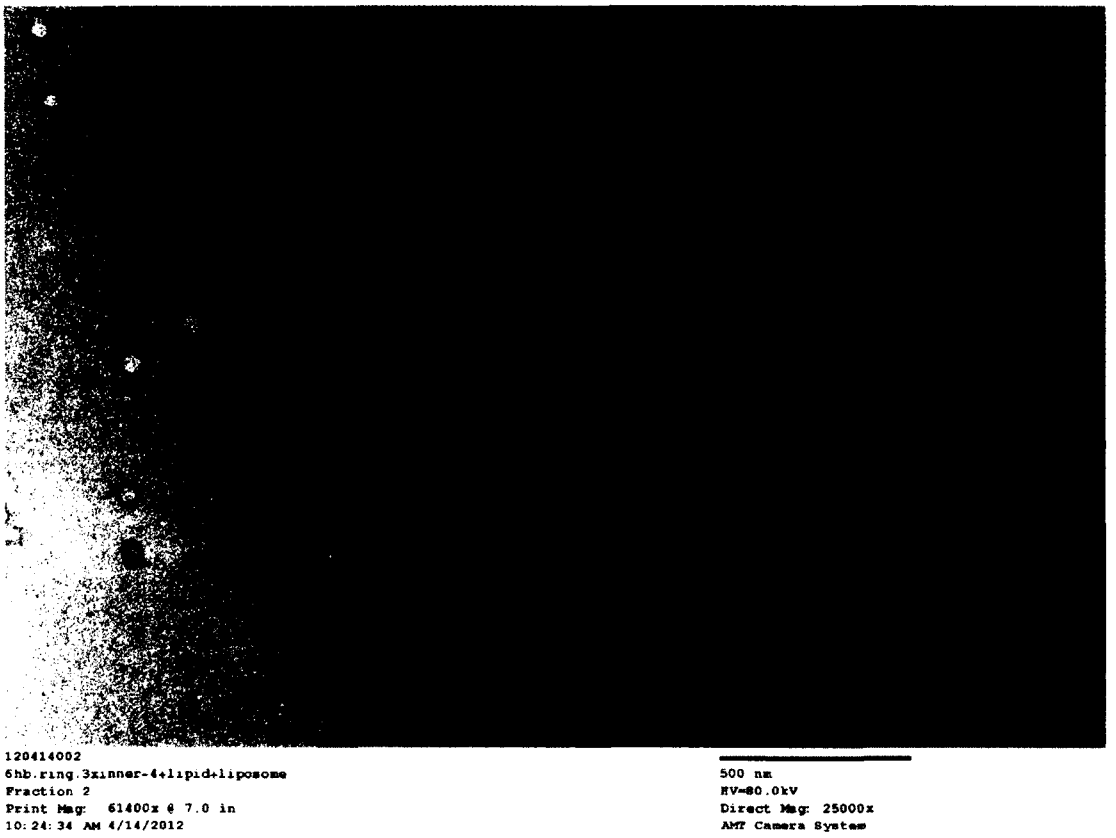


Figure 3.4 - Negative stain EM of Saturn product in fraction 2 after 5 hr of ultracentrifugation.

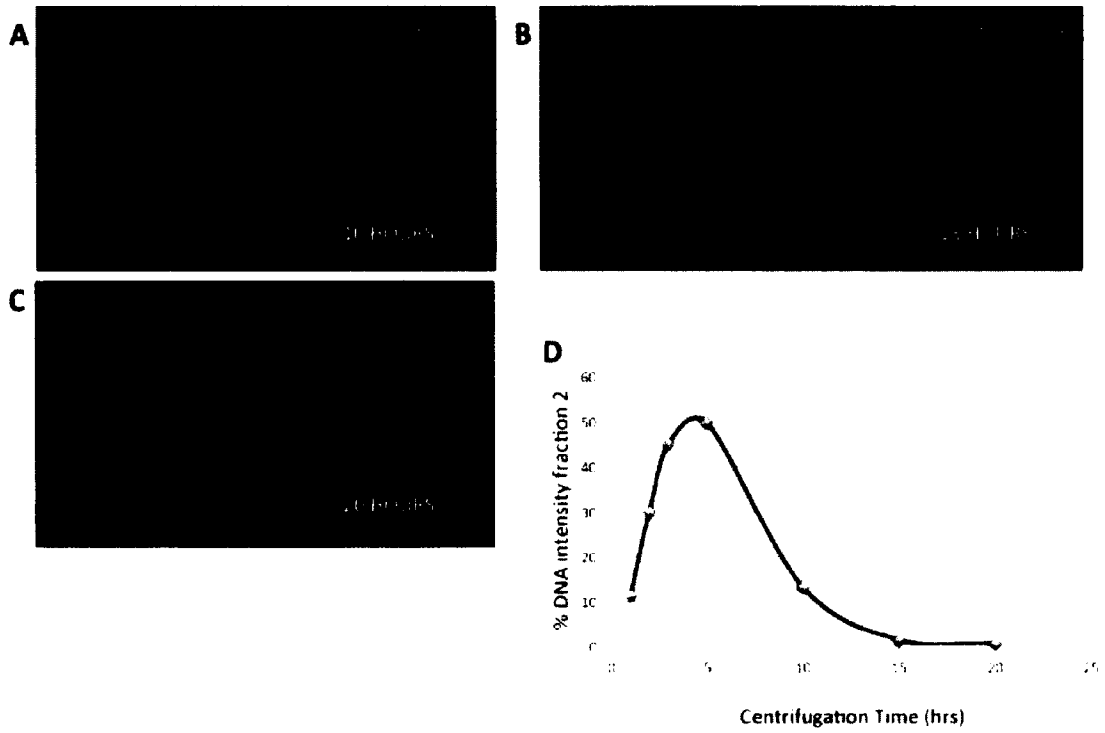


Figure 3.5 - SDS Agarose Gel of crude Saturn product after overnight dialysis at (A) 10hr (B) 15hrs (C) 20hrs ultracentrifugation. (D) Plot of % DNA intensity in fraction 2 over various ultracentrifugation times.

Figure 3.6 - Negative stain EM of Saturn product in fraction 5 after 20 hrs of ultracentrifugation.

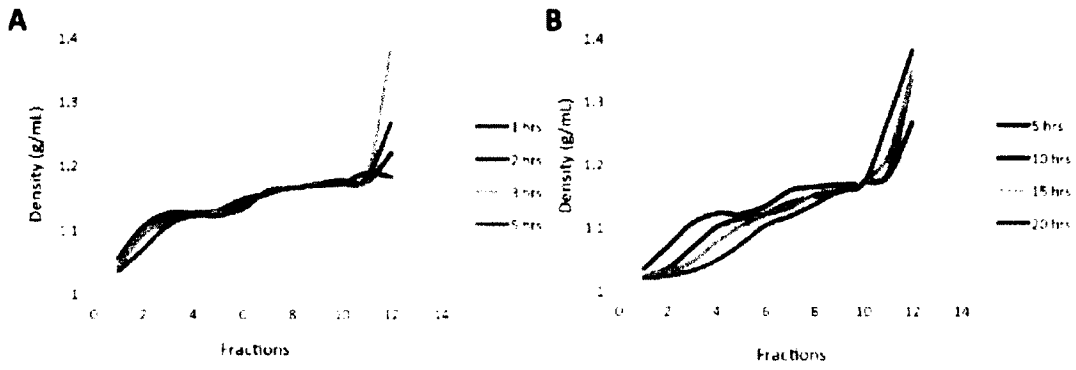


Figure 3.7 - Measured density of iodixanol for fractions after (A) 1 hr, 2hrs, 3hrs, 5hrs and (B) 5hrs, 10hrs, 15hrs, 20 hrs of ultracentrifugation.

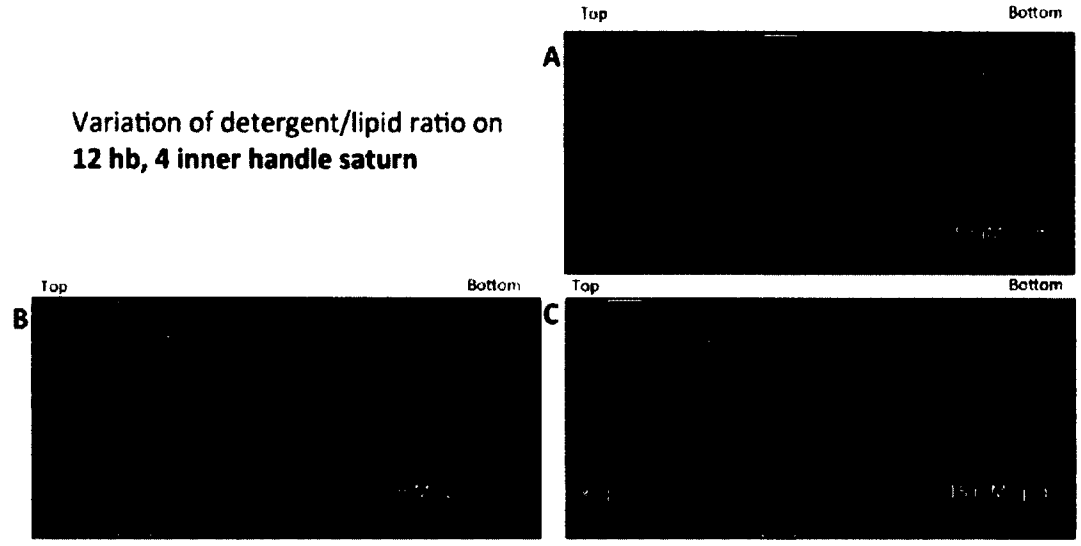


Figure 3.8 - SDS Agarose Gel of purified 12 hb 4inner handle templated Saturn structures with varying lipid concentrations (A) 0.5 mM (B) 3 mM and (C) 15 mM.

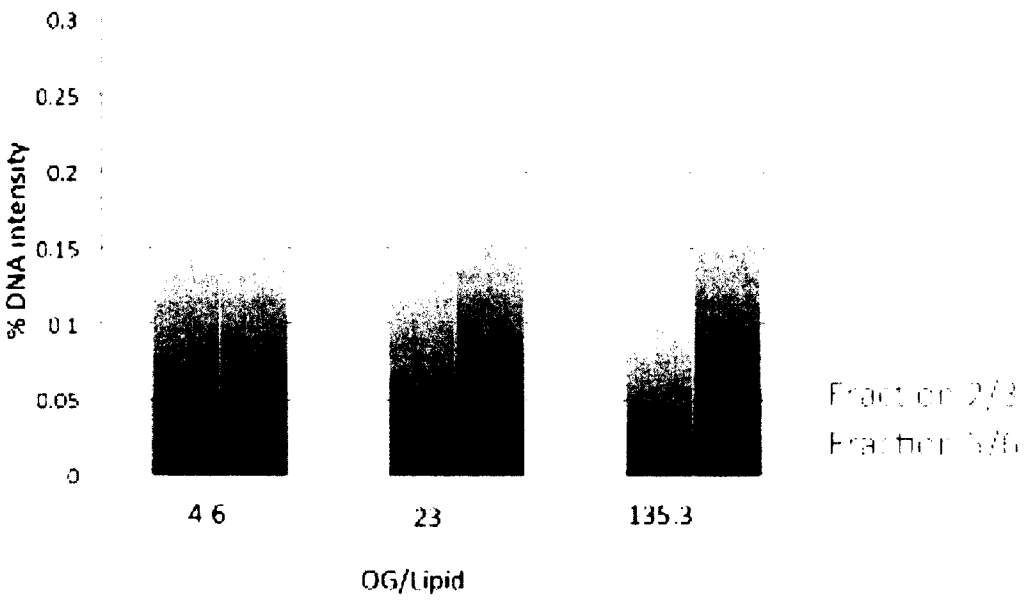


Figure 3.9 - Plot of % DNA intensity in figure 3.8 versus detergent to lipid ratio of fraction 2 or 3 and 5 or 6 (the peak DNA intensities).

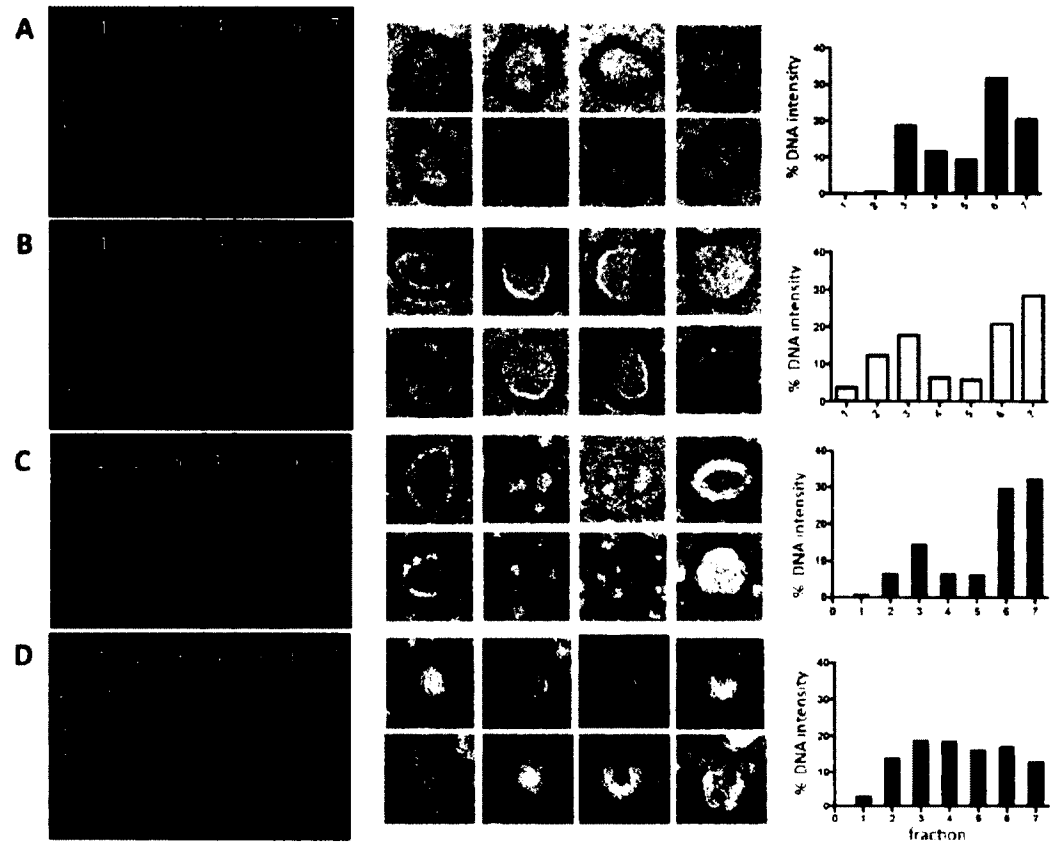


Figure 3.10 - 12hb 4inner handle templated Saturn intermediates after (A) 0hrs (B) 0.5 hrs (C) 1hr dialysis and final products after (D) overnight dialysis. The first column shows the SDS agarose gel of all the fractions, the middle column are negative stain EM images from fraction 4, and the last column are plots of % DNA ring signal from the SDS agarose gel in the first column.

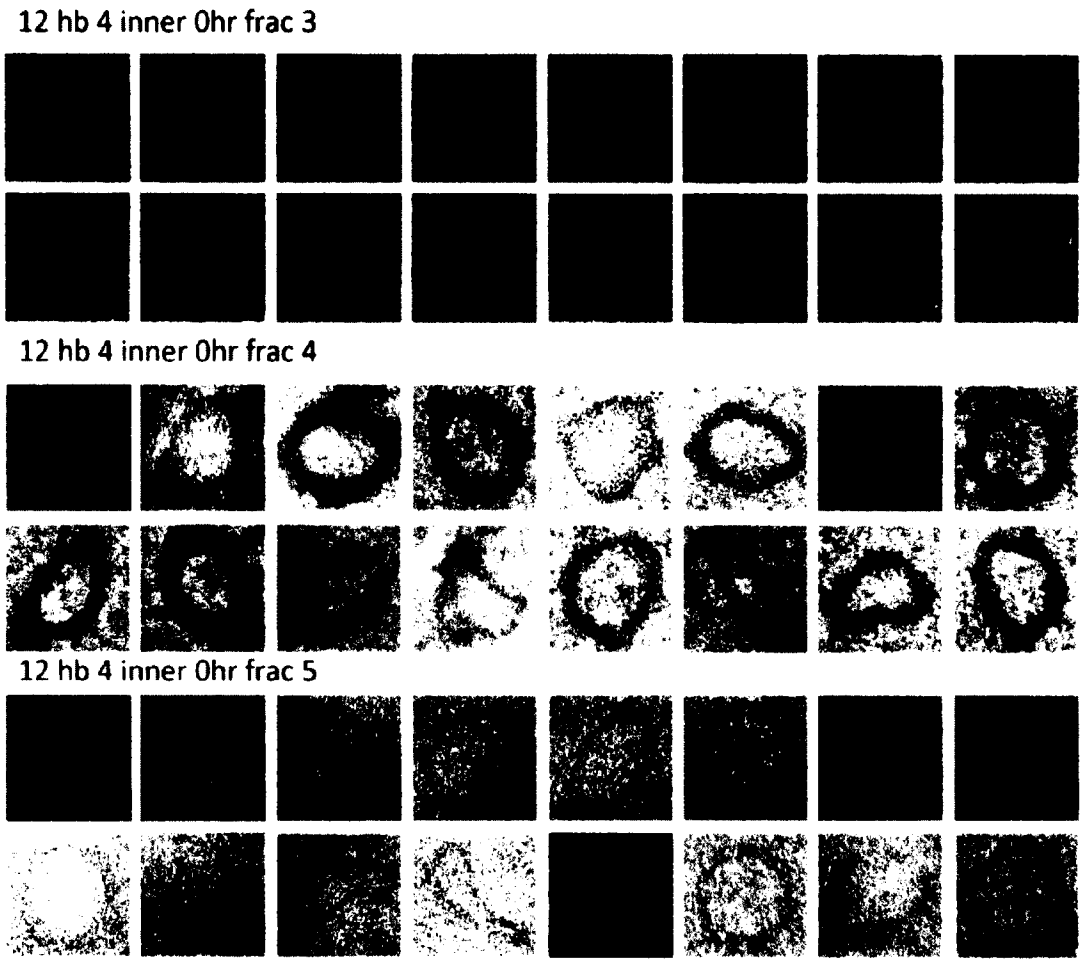


Figure 3.11 - Negative stain EM of fractions 3-5 for the 12hb 4inner handle templated Saturn intermediate after 0 hrs of dialysis.

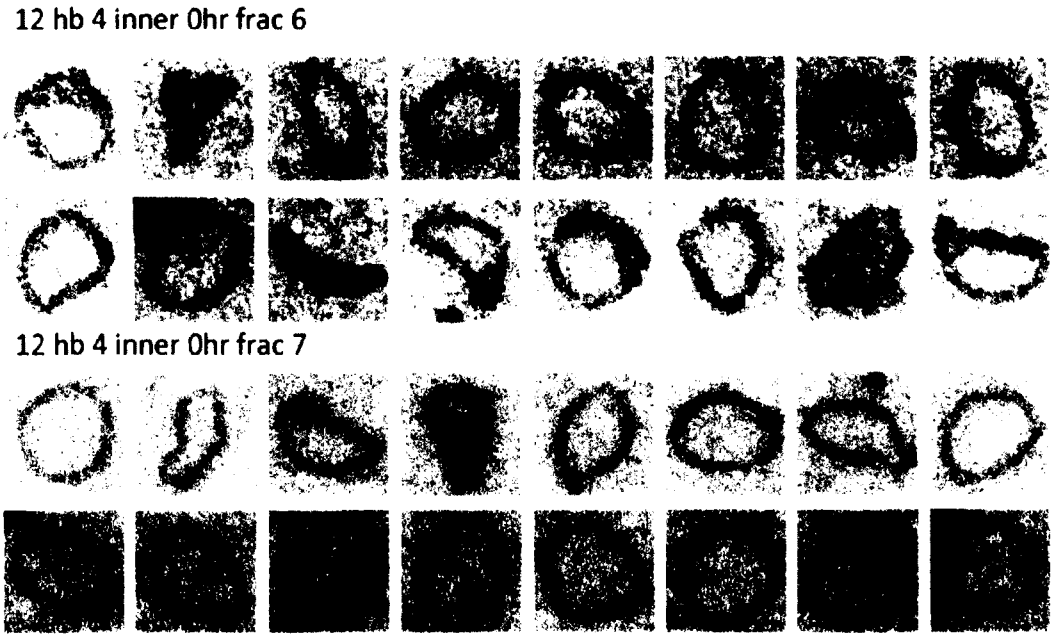


Figure 3.12 - Negative stain EM of fractions 6 and 7 for the 12hb 4inner handle templated Saturn intermediate after 0 hrs of dialysis.

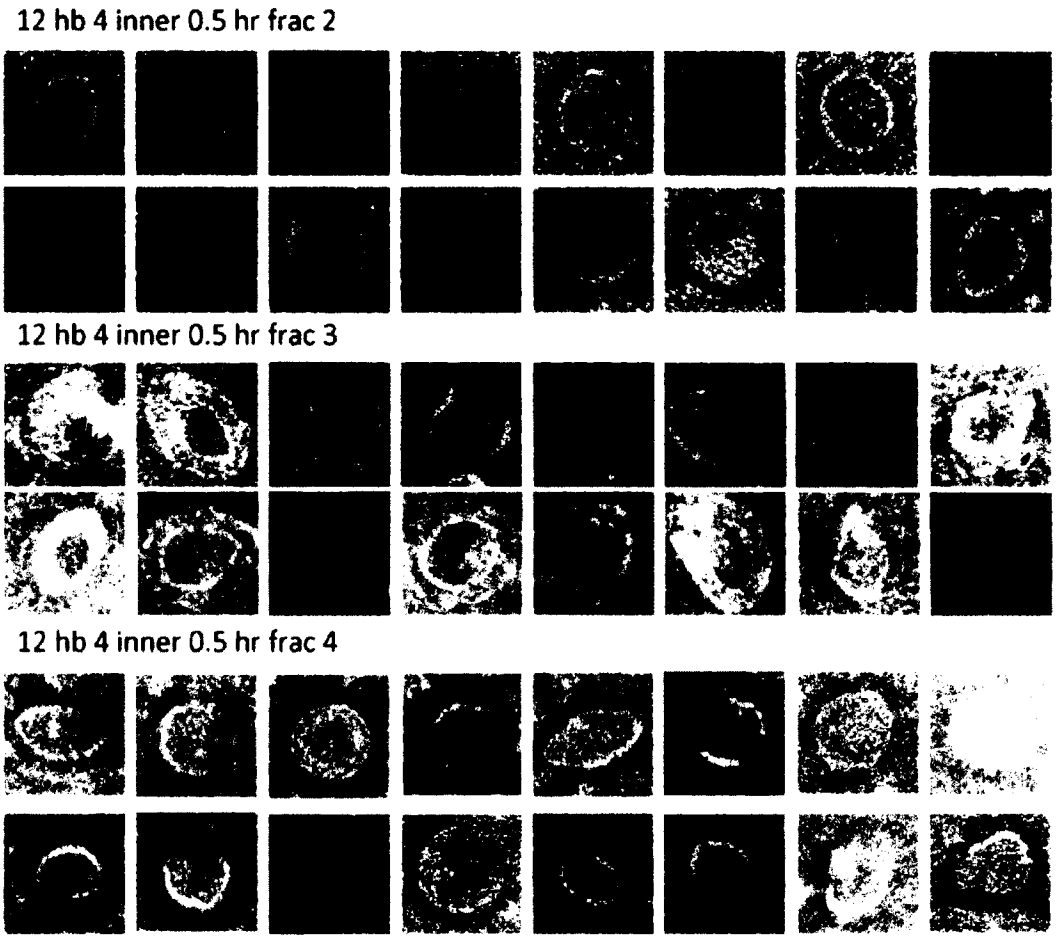


Figure 3.13 - Negative stain EM of fractions 2-4 for the 12hb 4inner handle templated Saturn intermediate after 0.5 hrs of dialysis.

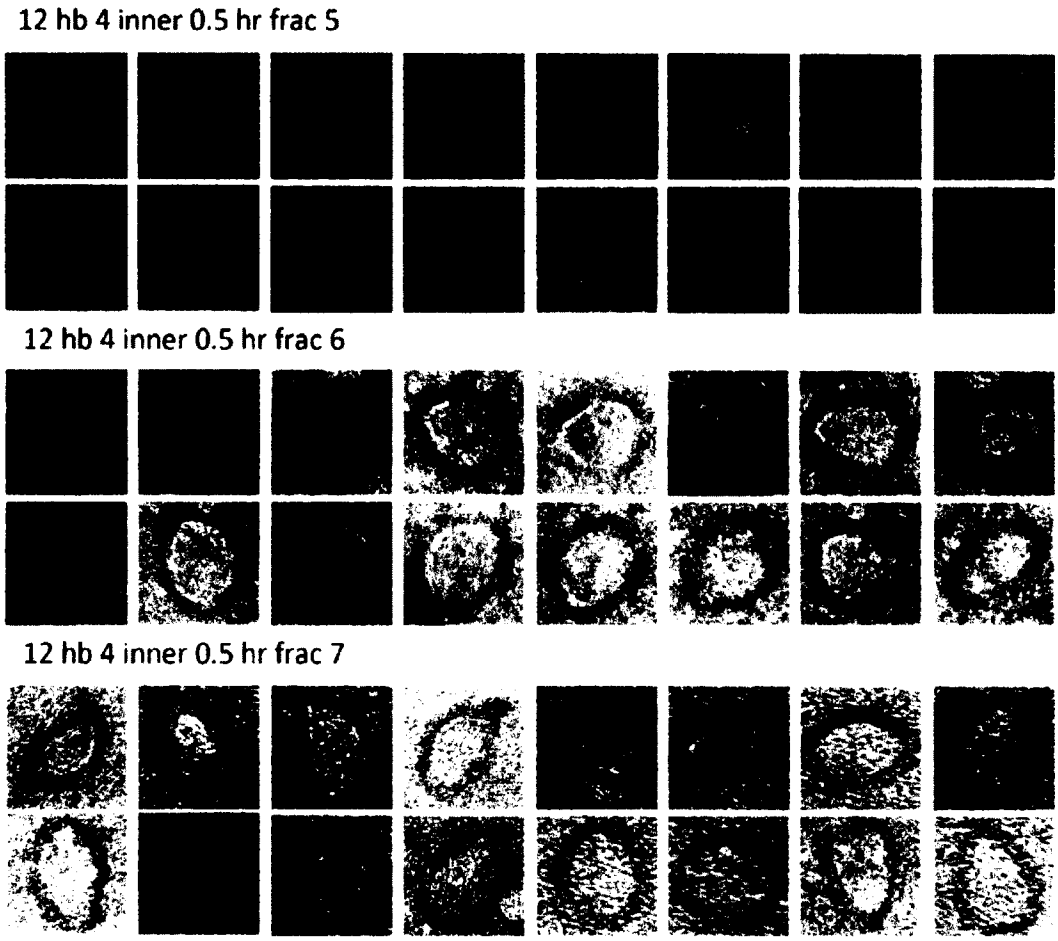


Figure 3.14 - Negative stain EM of fractions 5-7 for the 12hb 4inner handle templated Saturn intermediate after 0.5 hrs of dialysis.

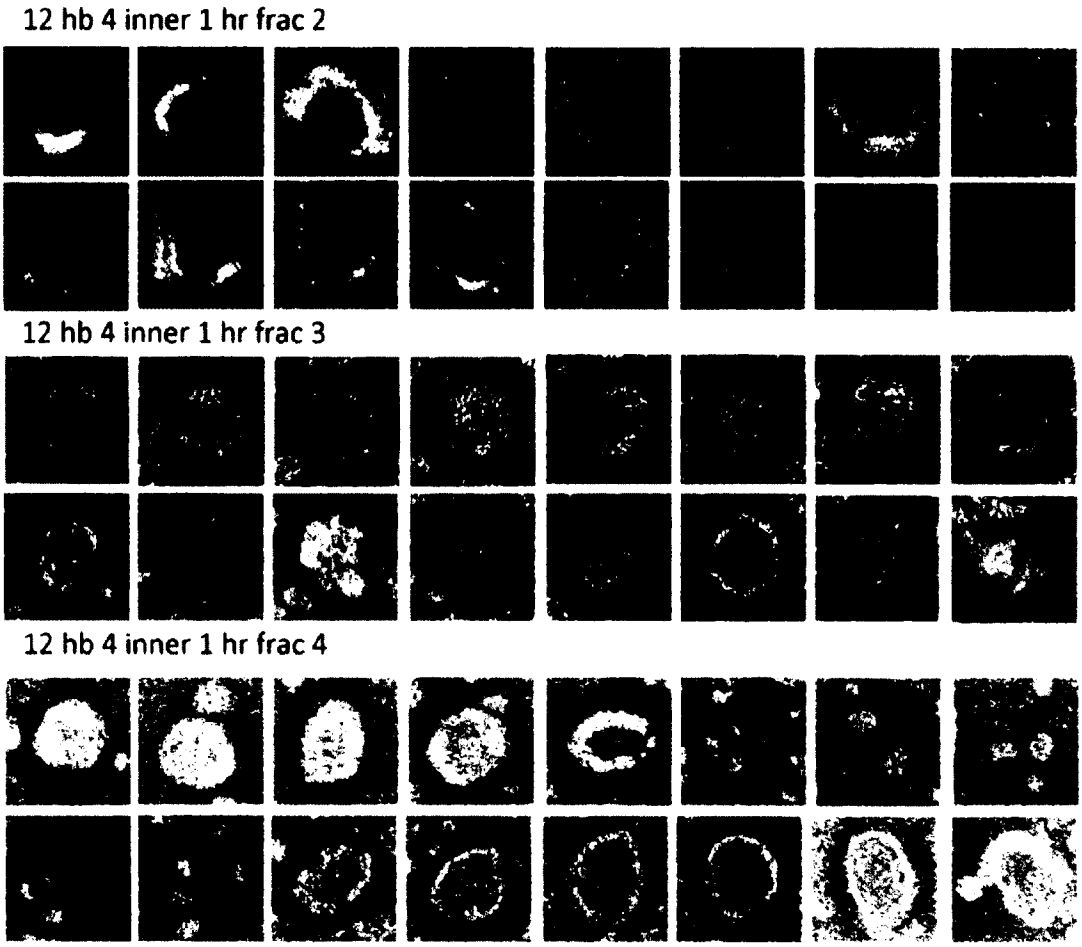


Figure 3.15 - Negative stain EM of fractions 2-4 for the 12hb 4inner handle templated Saturn intermediate after 1 hr of dialysis.

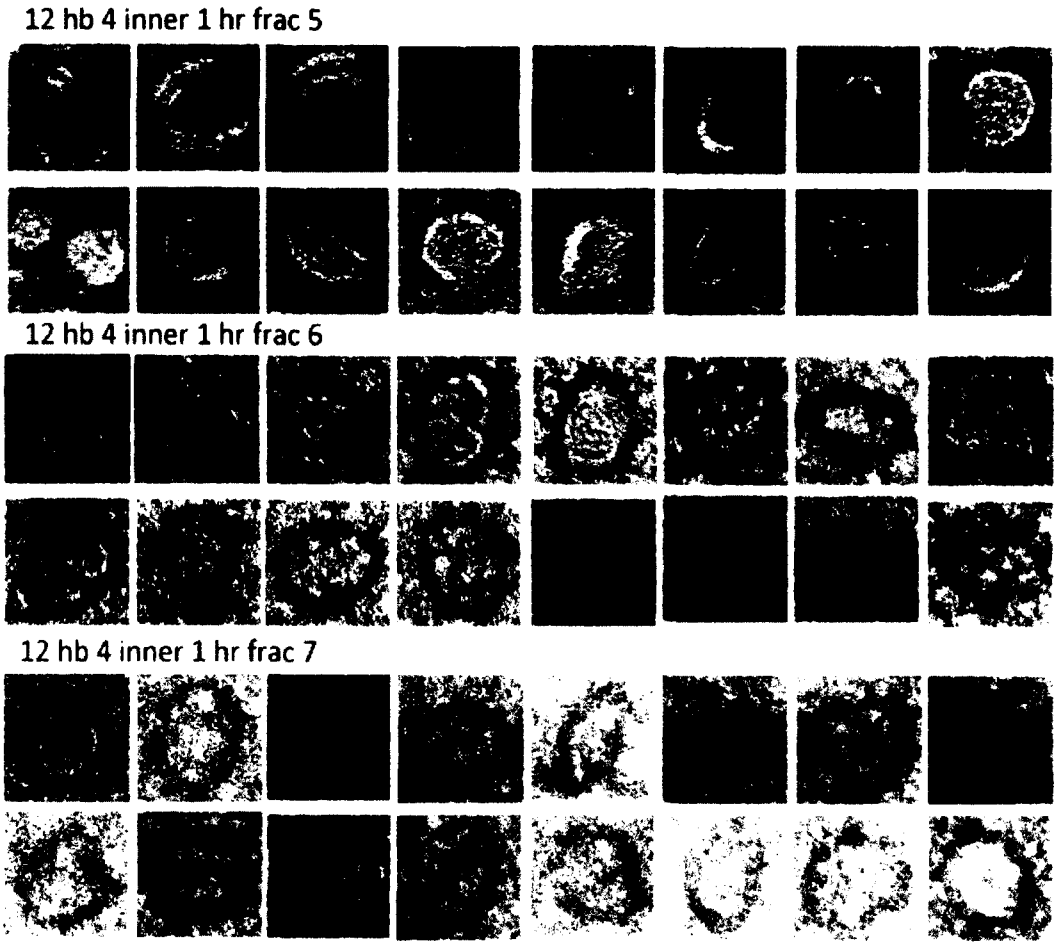


Figure 3.16 - Negative stain EM of fractions 5-7 for the 12hb 4inner handle templated Saturn intermediate after 1 hr of dialysis.

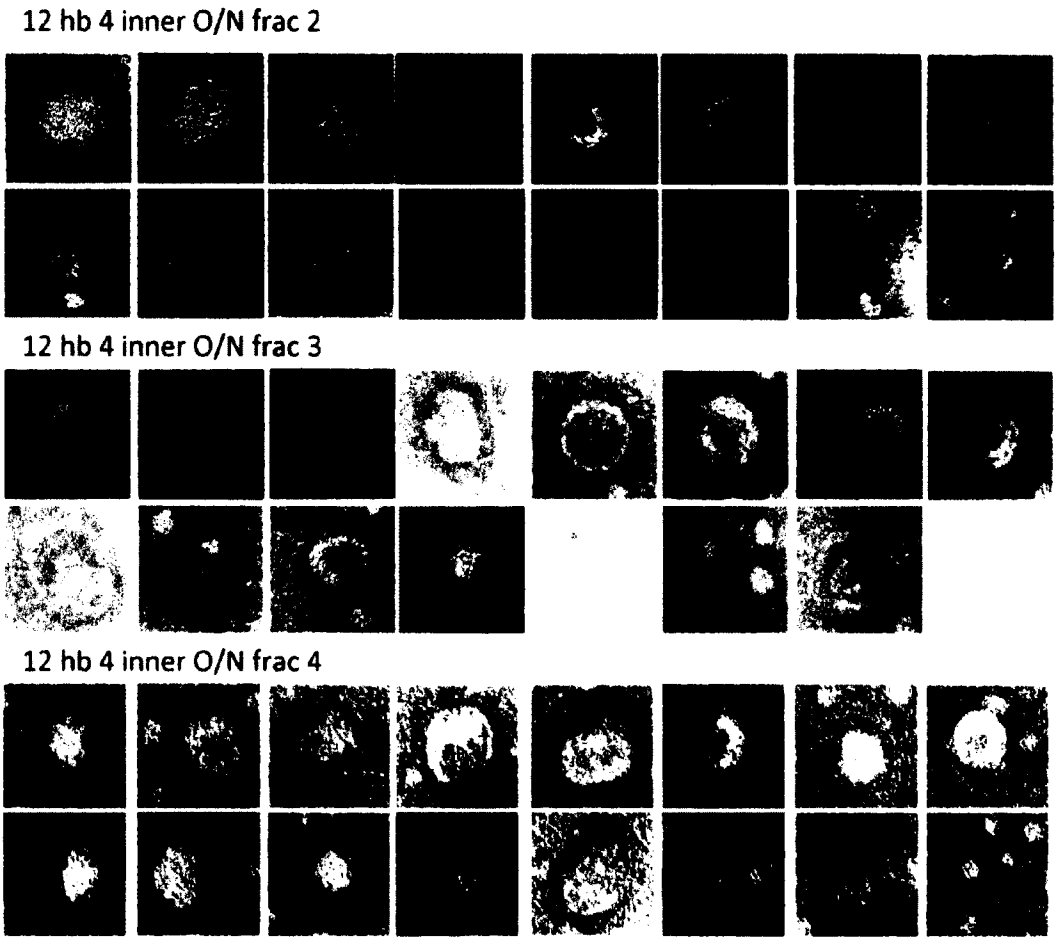


Figure 3.17 - Negative stain EM of fractions 2-4 for the 12hb 4inner handle templated Saturn product after overnight dialysis.

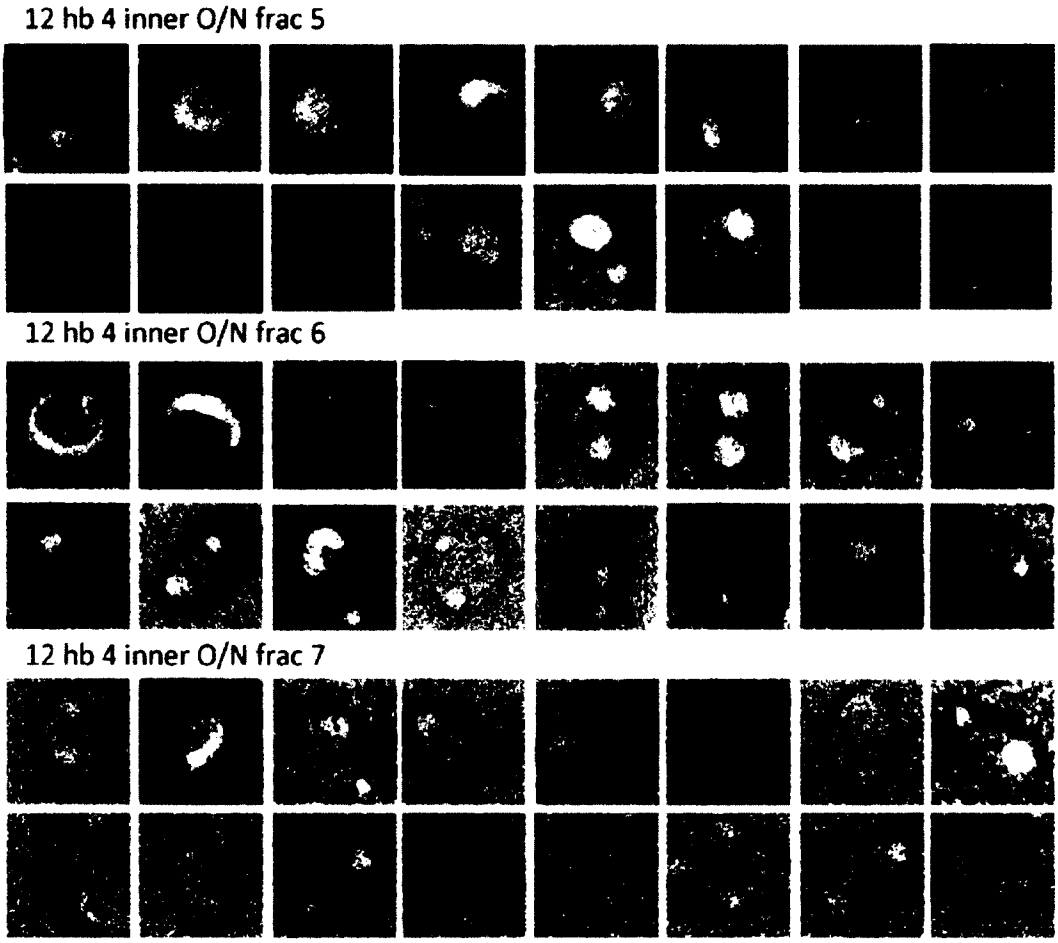


Figure 3.18 - Negative stain EM of fractions 5-7 for the 12hb 4inner handle templated Saturn product after overnight dialysis.

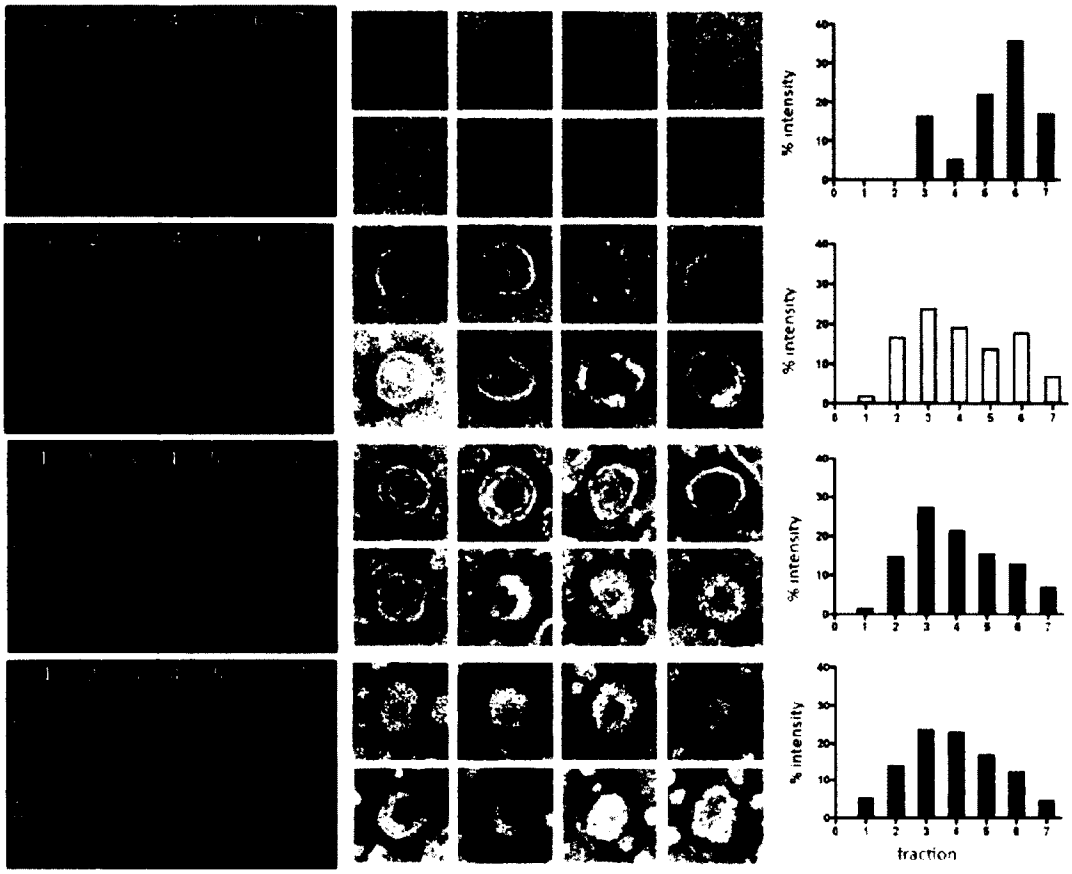


Figure 3.19 - 12hb 8inner handle templated Saturn intermediates after (A) 0hrs (B) 0.5 hrs (C) 1hr dialysis and final products after (D) overnight dialysis. The first column shows the SDS agarose gel of all the fractions, the middle column are negative stain EM images from fraction 4, and the last column are plots of % DNA ring signal from the SDS agarose gel from the first column.

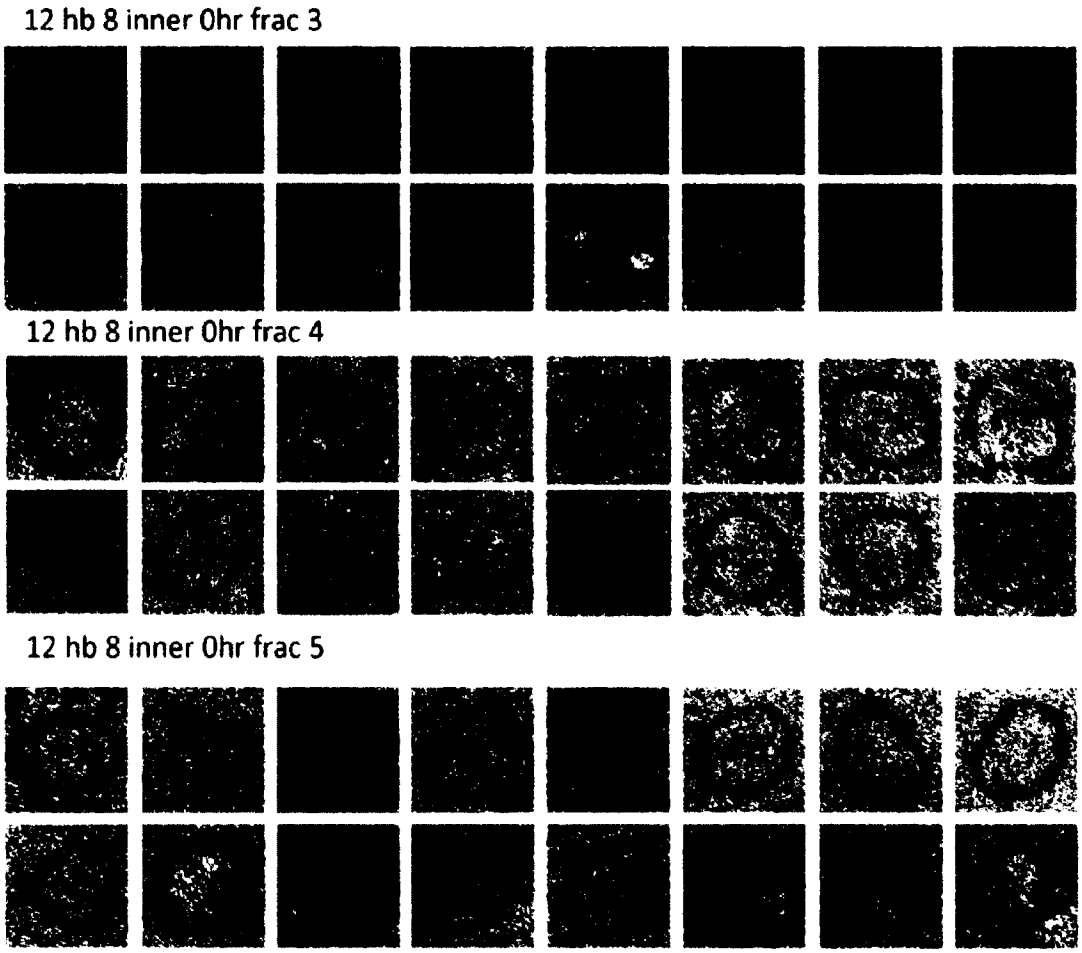


Figure 3.20 - Negative stain EM of fractions 3-5 for the 12hb 8inner handle templated Saturn intermediate after 0 hrs of dialysis.

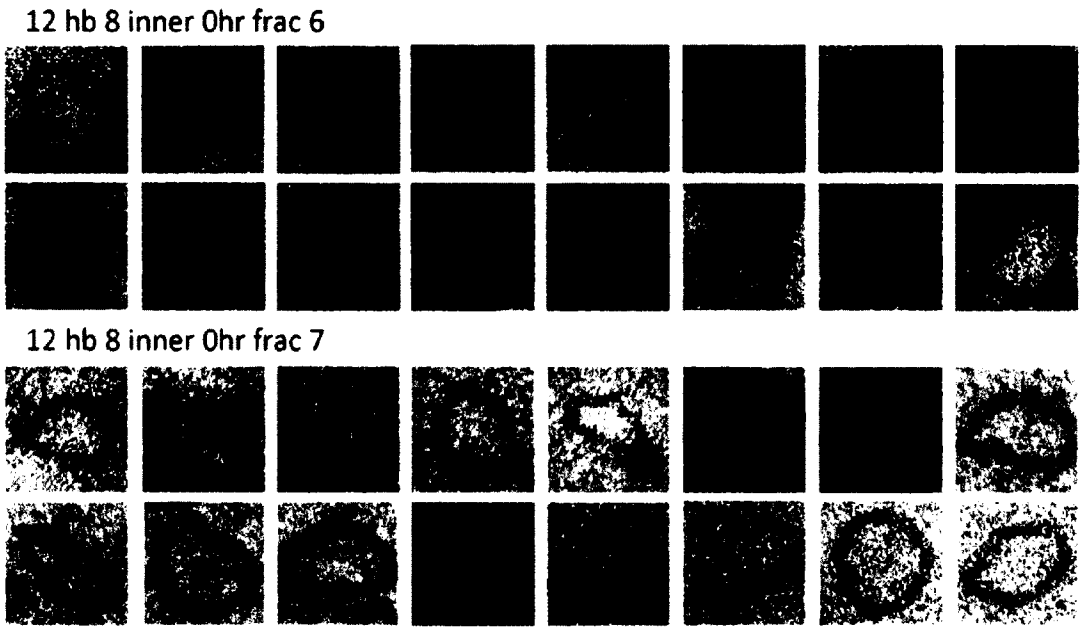


Figure 3.21 - Negative stain EM of fractions 6 and 7 for the 12hb 8inner handle templated Saturn intermediate after 0 hrs of dialysis.

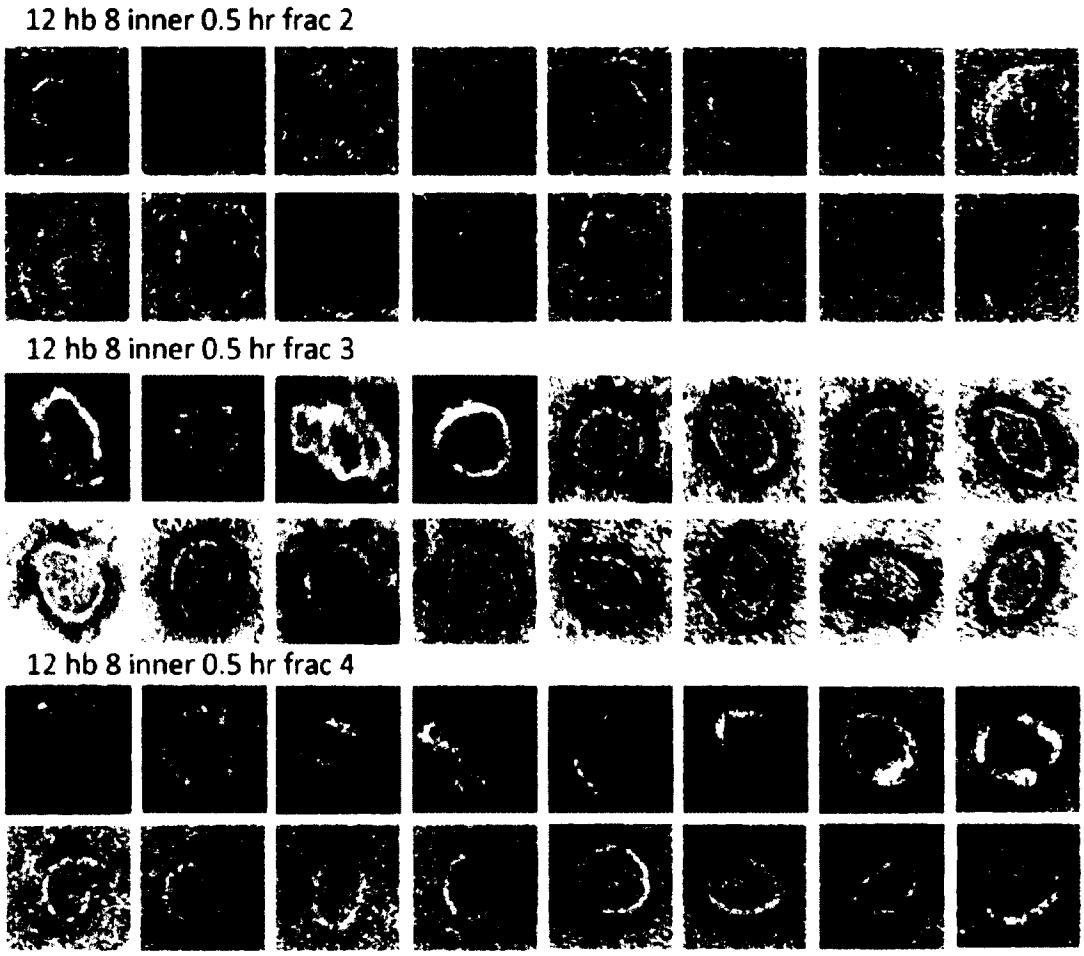


Figure 3.22 - Negative stain EM of fractions 2-4 for the 12hb 8inner handle templated Saturn intermediate after 0.5 hrs of dialysis.

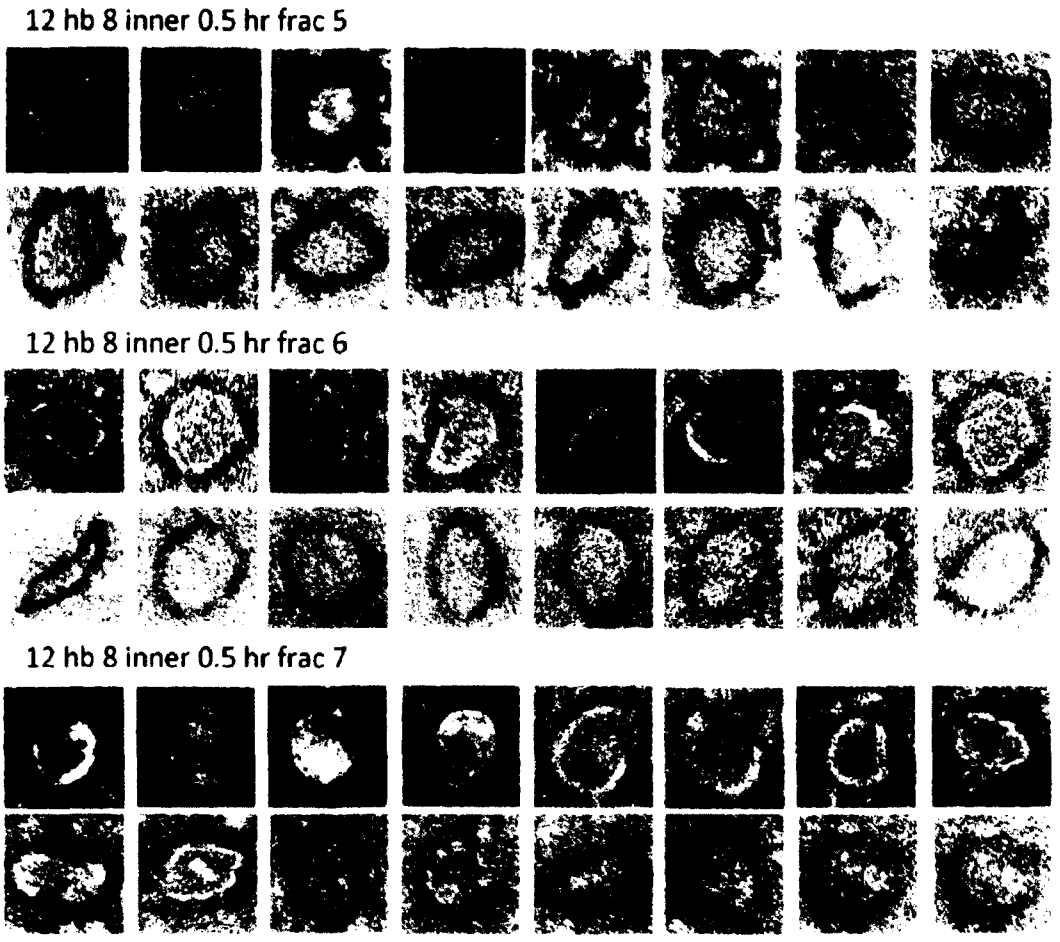


Figure 3.23 - Negative stain EM of fractions 5-7 for the 12hb 8inner handle templated Saturn intermediate after 0.5 hrs of dialysis.

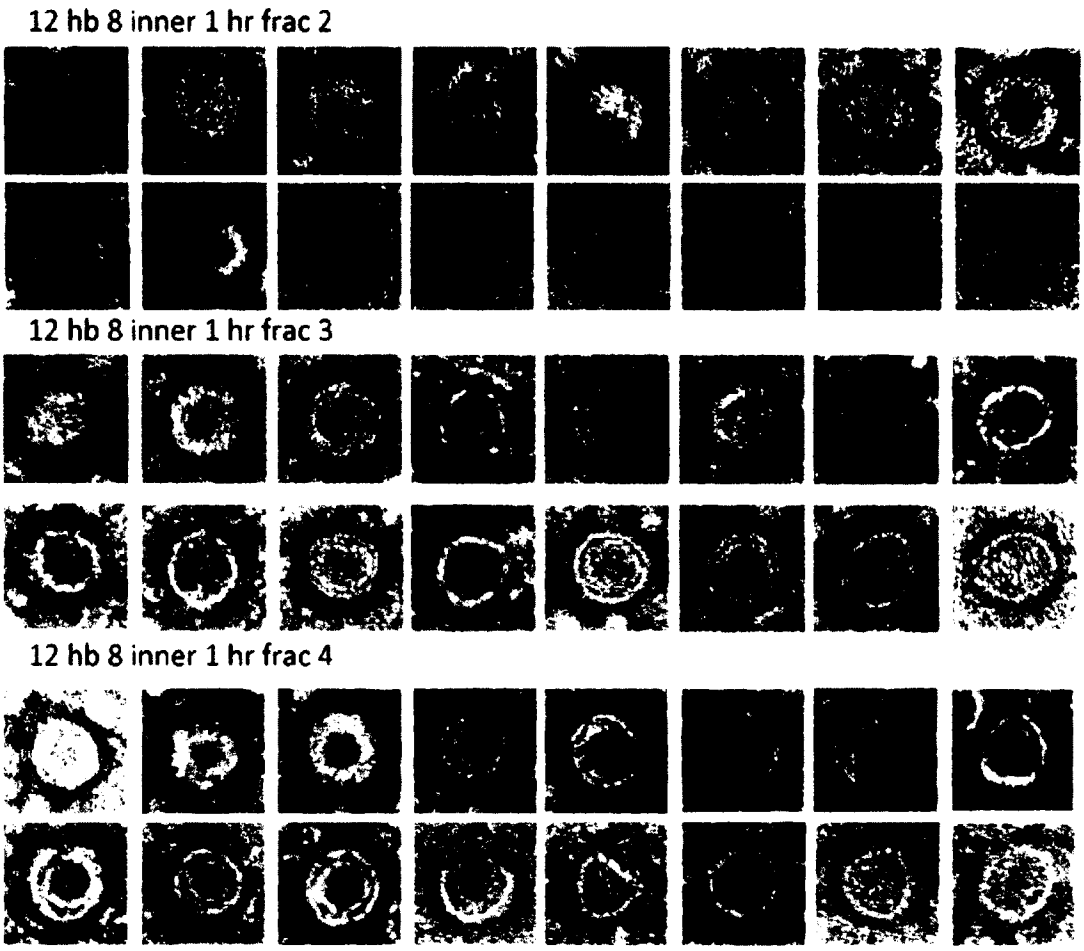


Figure 3.24 - Negative stain EM of fractions 2-4 for the 12hb 8inner handle templated Saturn intermediate after 1 hr of dialysis.

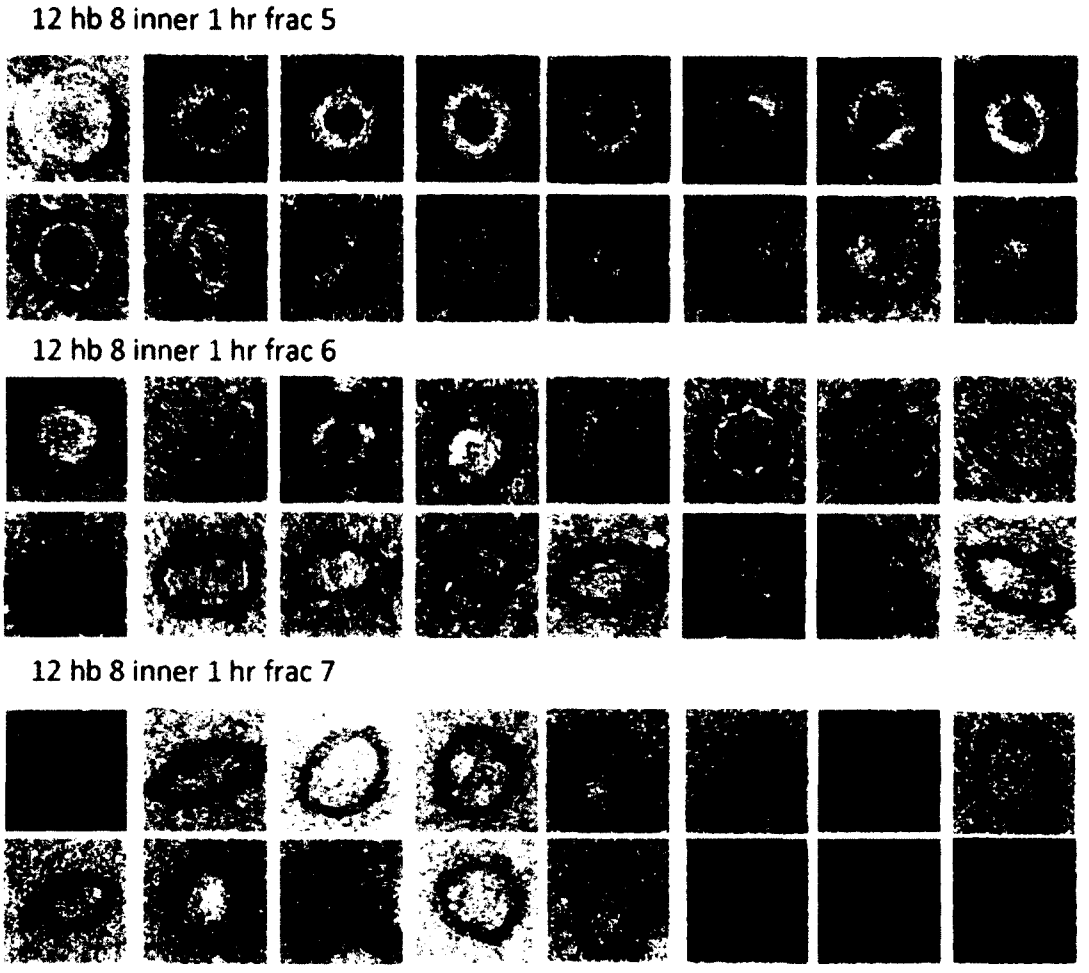


Figure 3.25 - Negative stain EM of fractions 5-7 for the 12hb 8inner handle templated Saturn intermediate after 1 hr of dialysis.

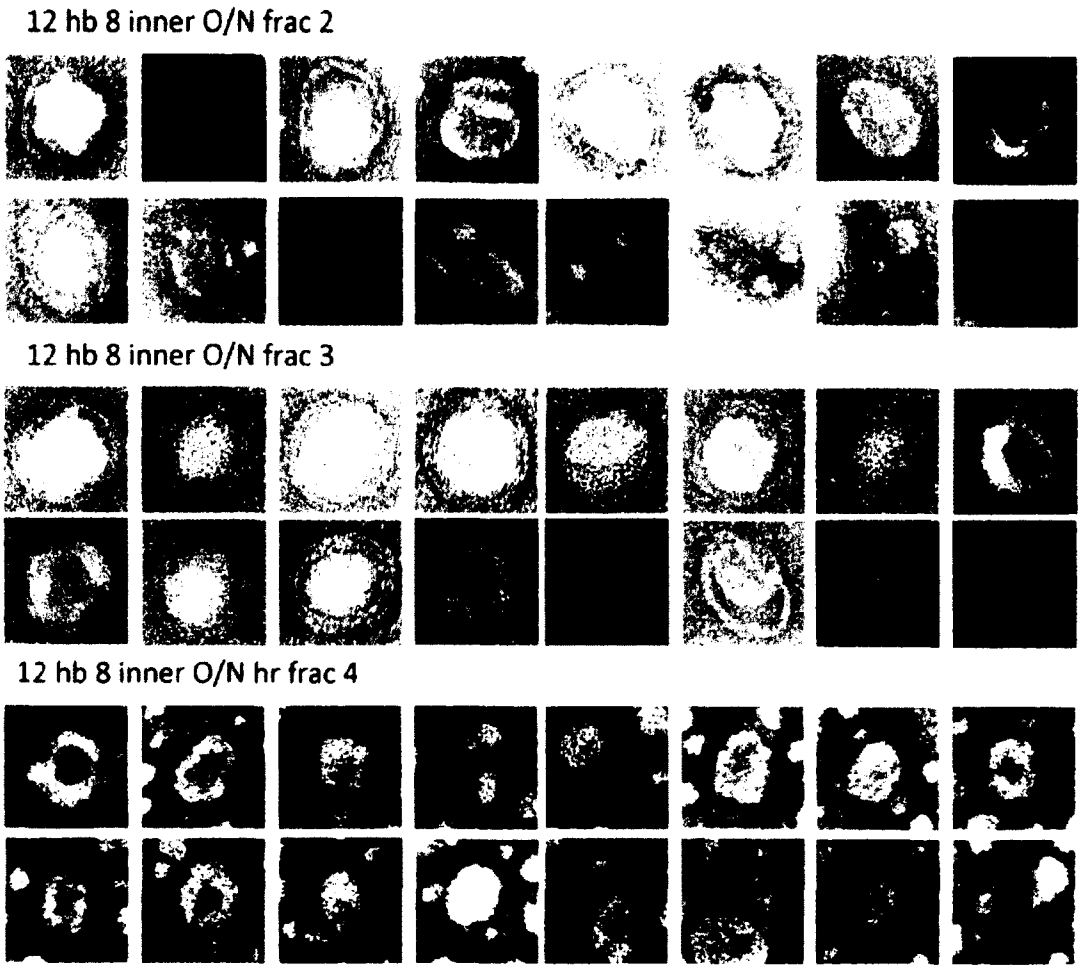


Figure 3.26 - Negative stain EM of fractions 2-4 for the 12hb 8inner handle templated Saturn product after overnight dialysis.

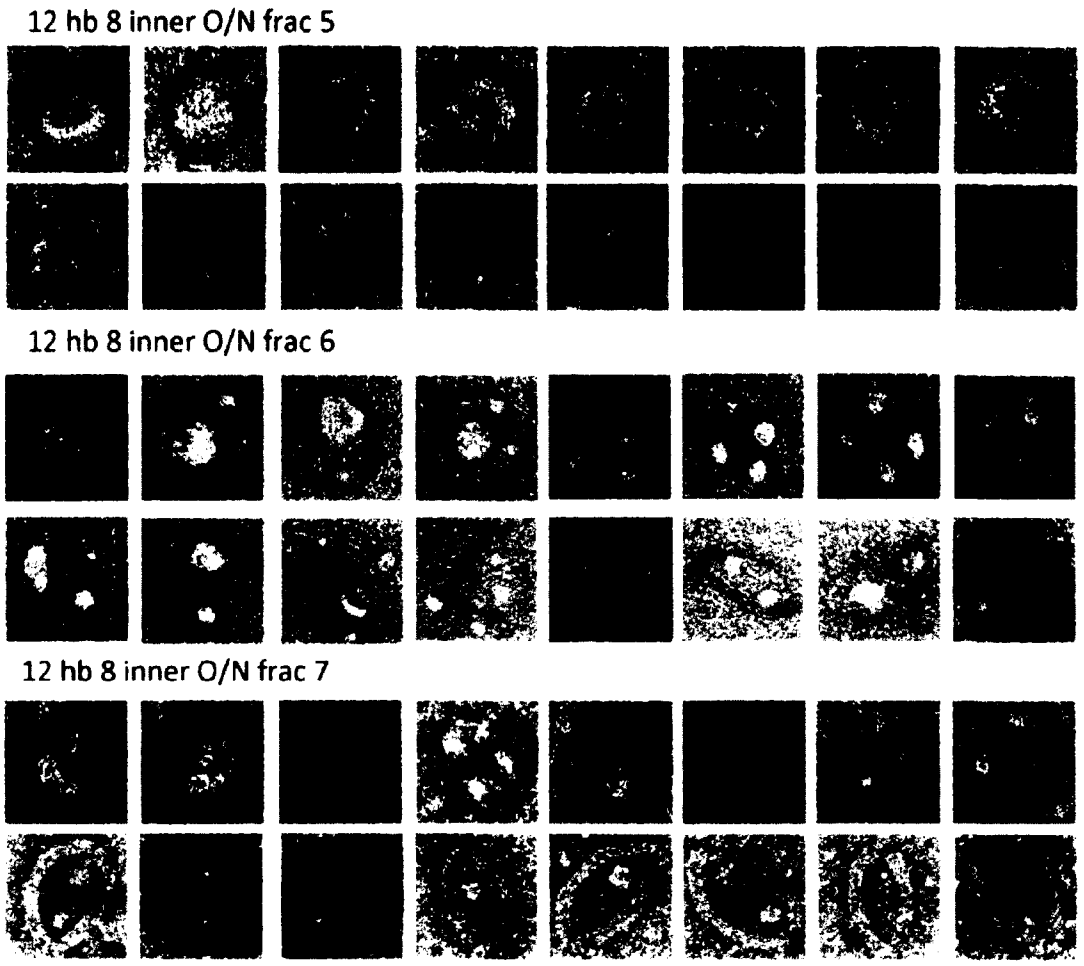


Figure 3.27 - Negative stain EM of fractions 5-7 for the 12hb 8inner handle templated Saturn product after overnight dialysis.

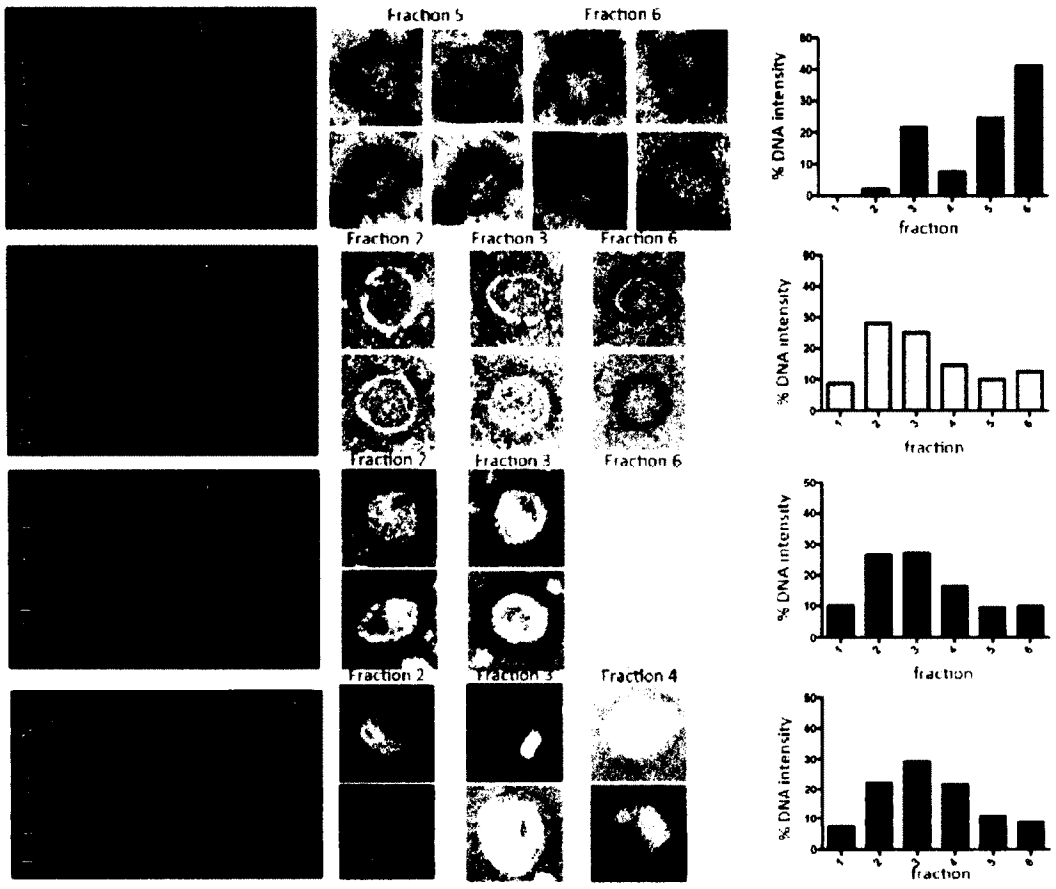


Figure 3.28 - 12hb 16inner handle templated Saturn intermediates after (A) 0hrs (B) 0.5 hrs (C) 1hr dialysis and final products after (D) overnight dialysis. The first column shows the SDS agarose gel of all the fractions, the middle column is negative stain EM images, and the last column are plots of % DNA ring signal from the SDS agarose gel in the first column.

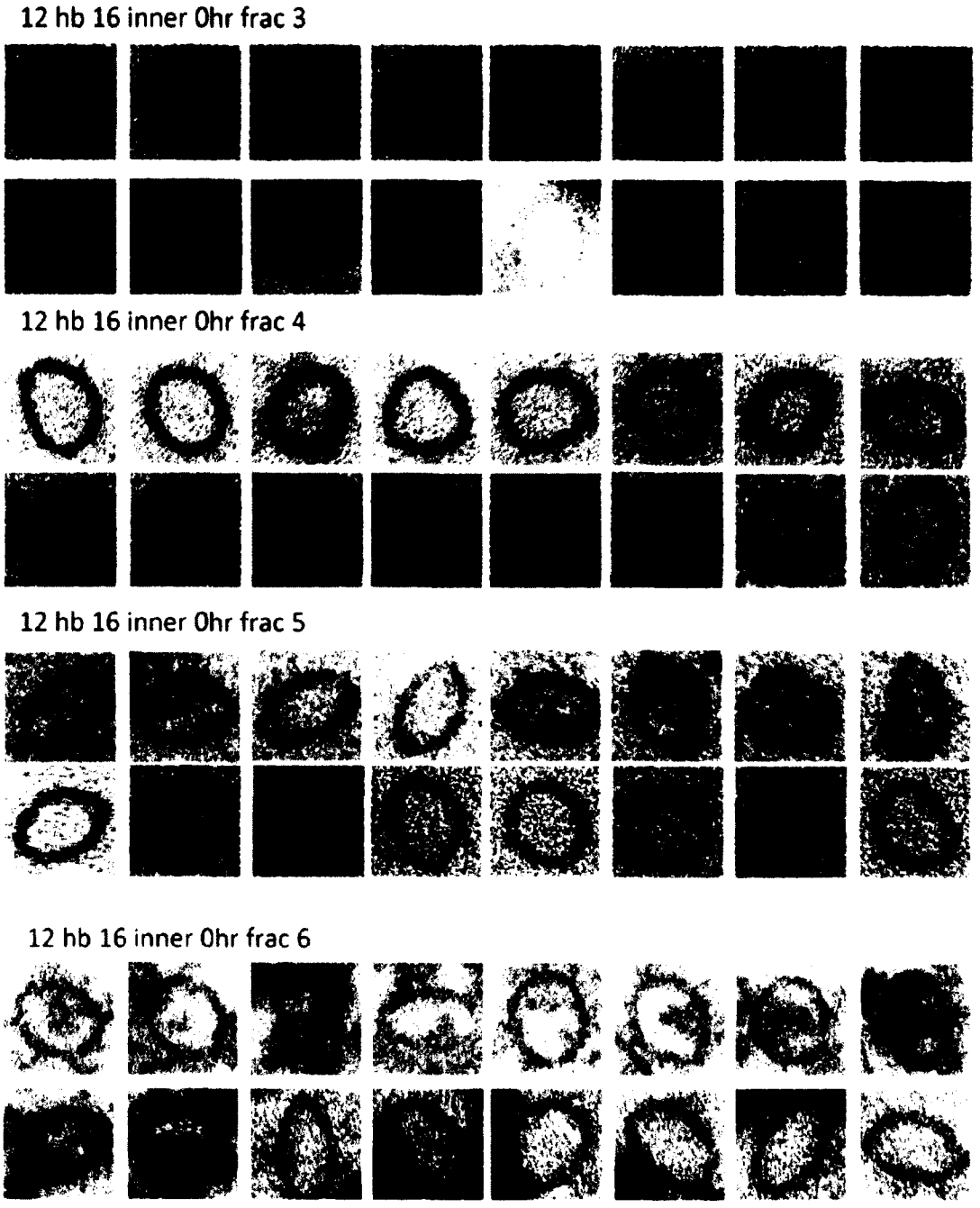


Figure 3.29 - Negative stain EM of fractions 3-6 for the 12hb 16 inner handle templated Saturn intermediate after 0 hrs of dialysis.

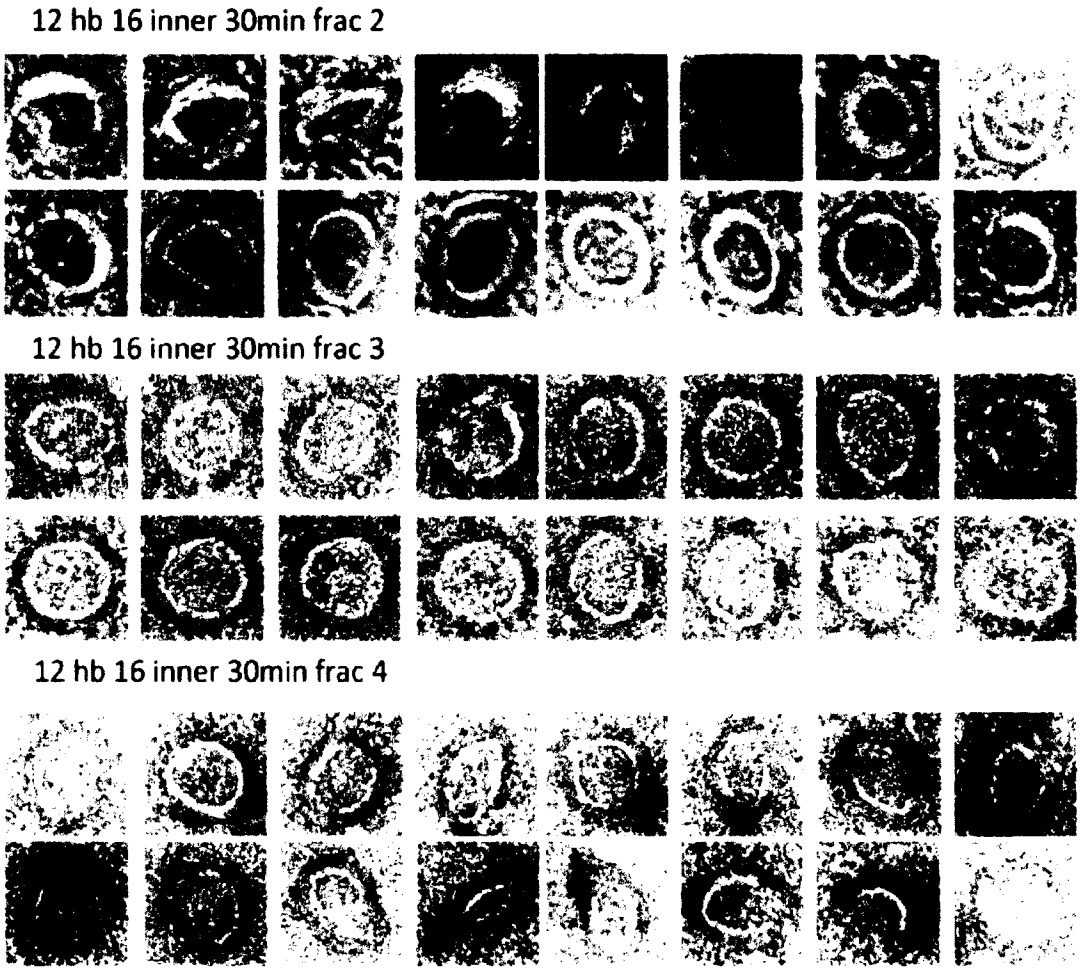


Figure 3.30 - Negative stain EM of fractions 2-4 for the 12hb 16inner handle templated Saturn intermediate after 0.5 hrs of dialysis.

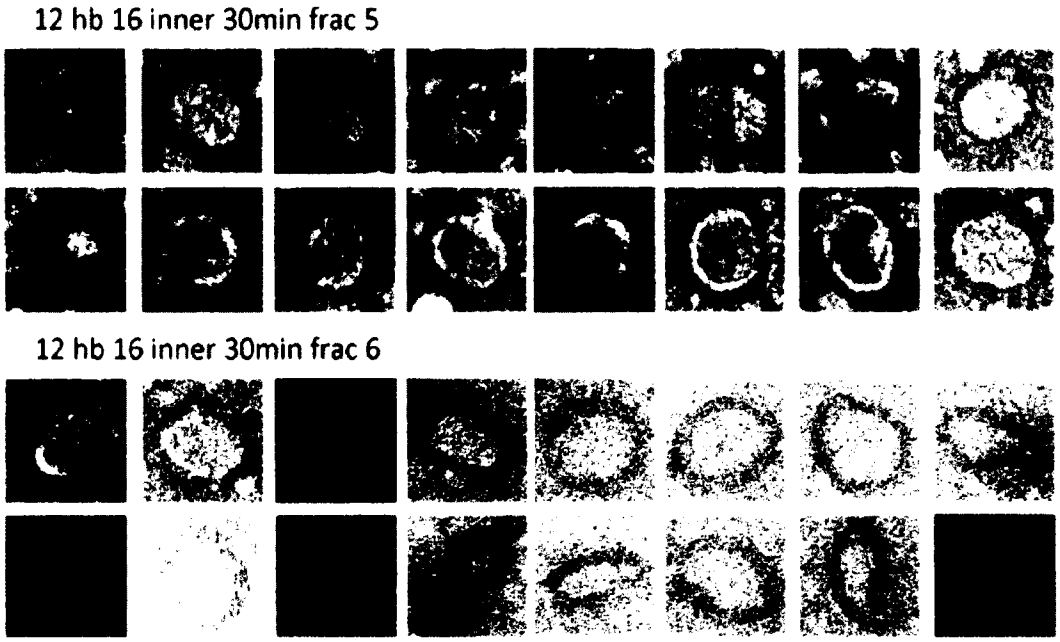


Figure 3.31 - Negative stain EM of fractions 5 and 6 for the 12hb 8inner handle templated Saturn intermediate after 0.5 hrs of dialysis.

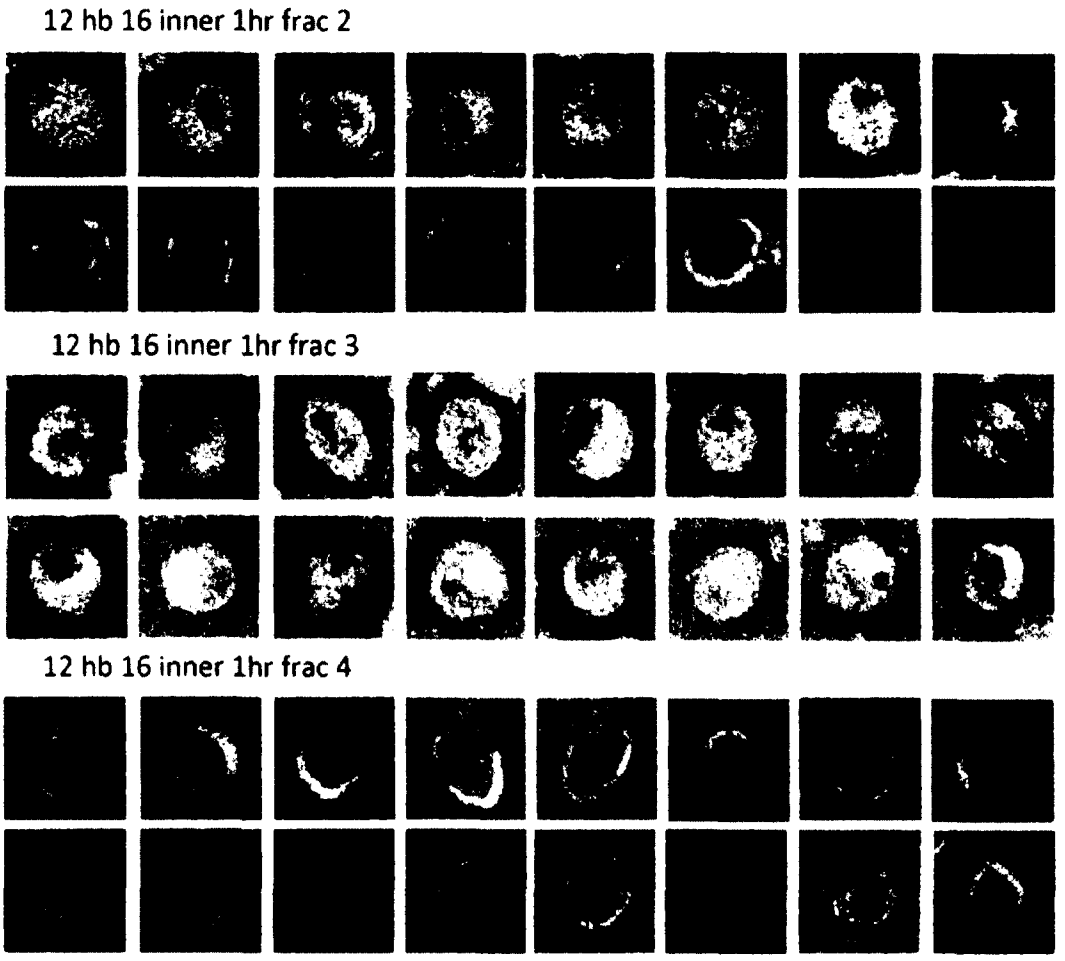


Figure 3.32 - Negative stain EM of fractions 2-4 for the 12hb 16inner handle templated Saturn intermediate after 1 hr of dialysis.

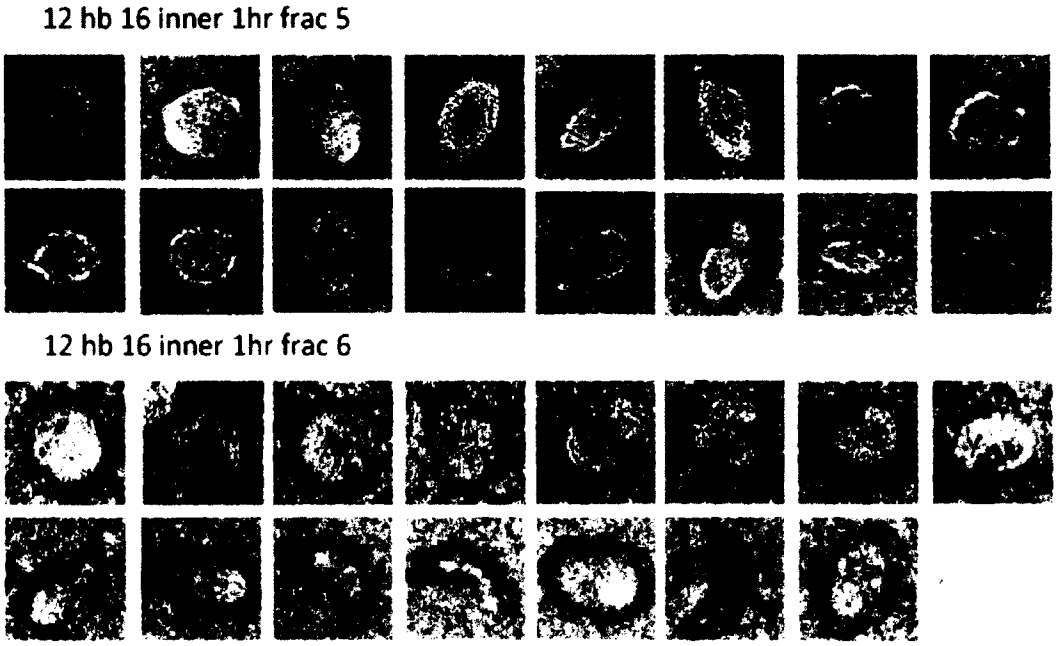


Figure 3.33 - Negative stain EM of fractions 5 and 6 for the 12hb 16inner handle templated Saturn intermediate after 1 hr of dialysis.

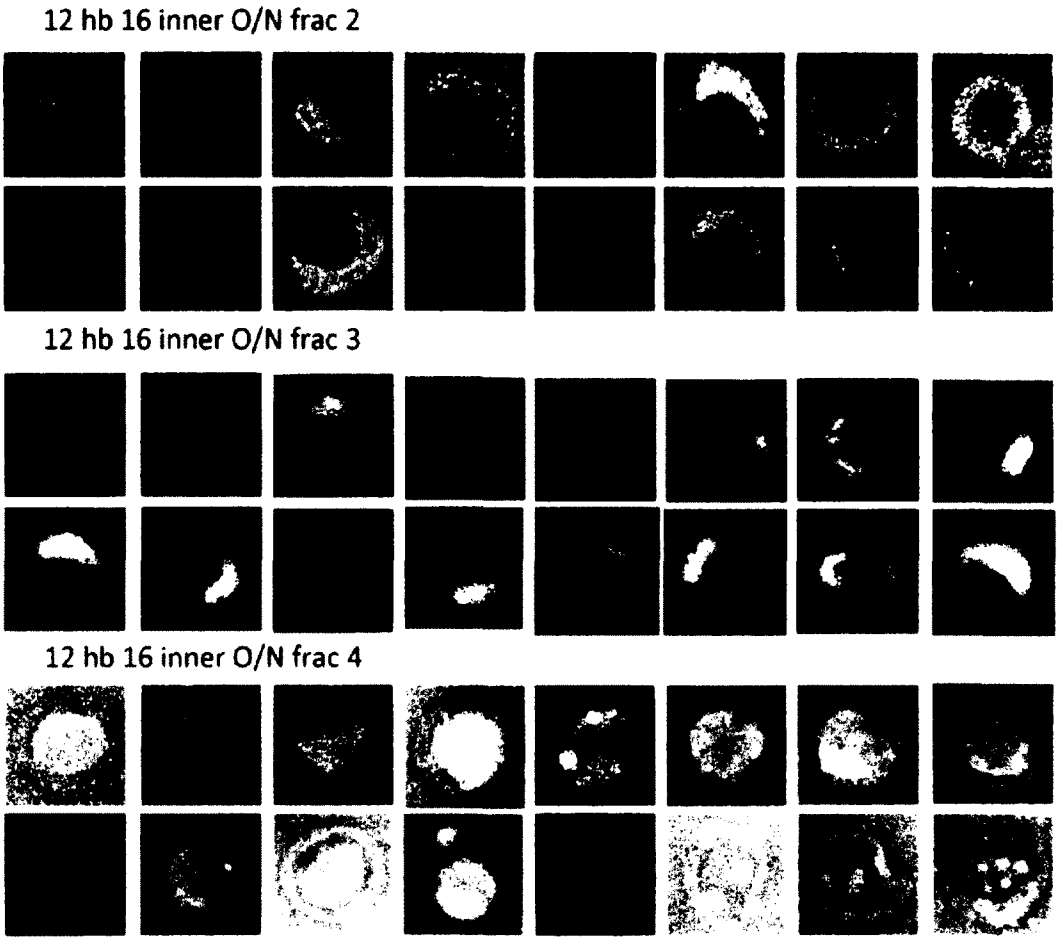


Figure 3.34 - Negative stain EM of fractions 2-4 for the 12hb 16inner handle templated Saturn product after overnight dialysis.

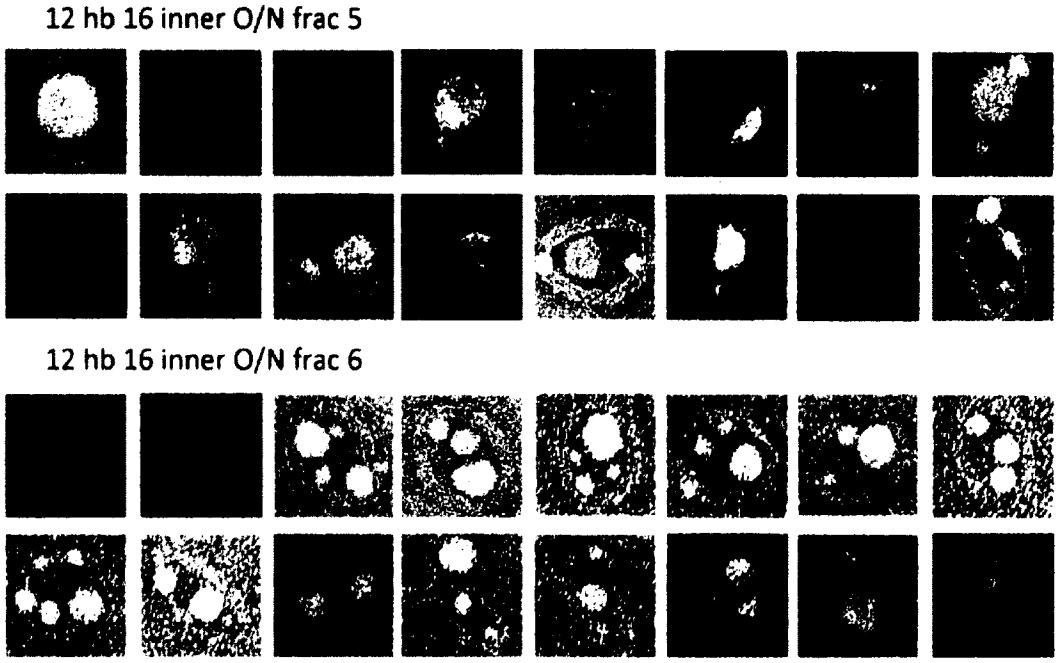


Figure 3.35 - Negative stain EM of fractions 5 and 6 for the 12hb 16inner handle templated Saturn product after overnight dialysis.

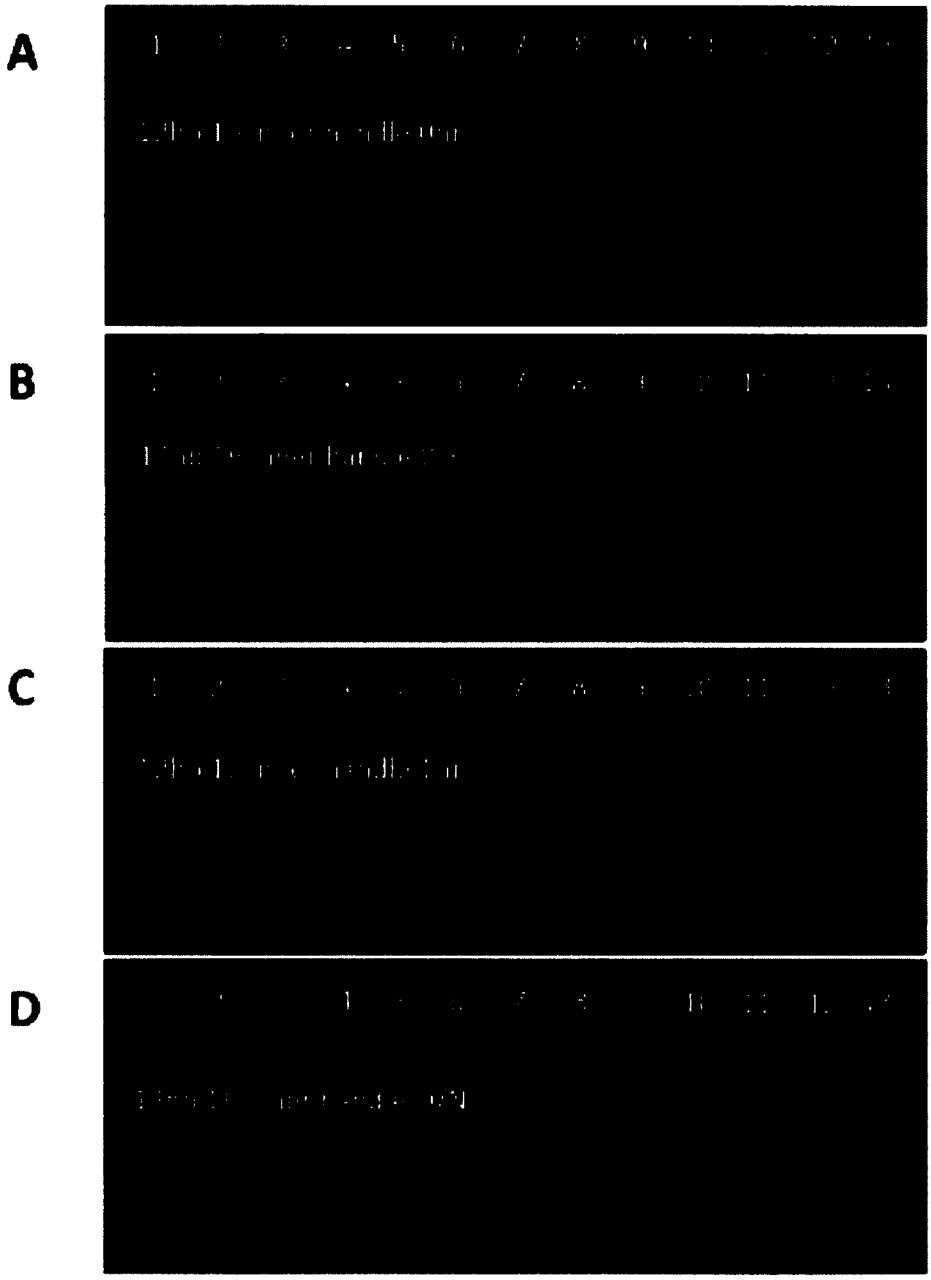


Figure 3.36 - Control: SDS agarose gel of purified 12hb 16inner handle templated vesicles in the absence of lipid anchors after (A) 0hrs (B) 0.5 hrs (C) 1hr and (D) overnight dialysis.

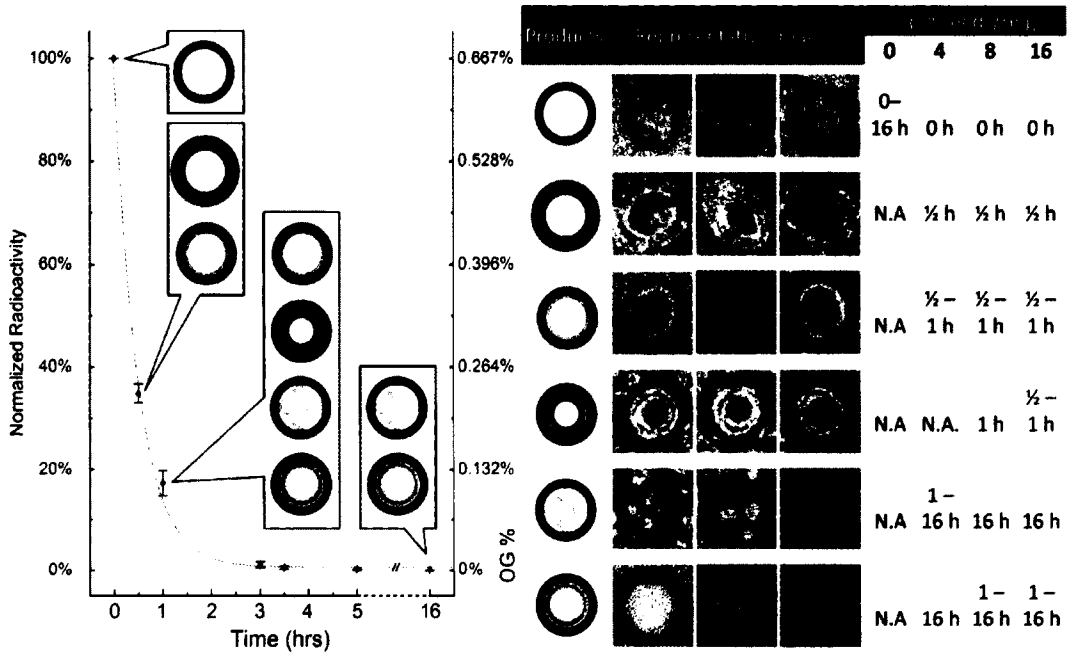


Figure 3.37 - Summary of intermediates and final products identified in the mechanism of 12 hb ring's templated Saturn formation in accordance with the percentage of radioactive detergent remaining over dialysis time.

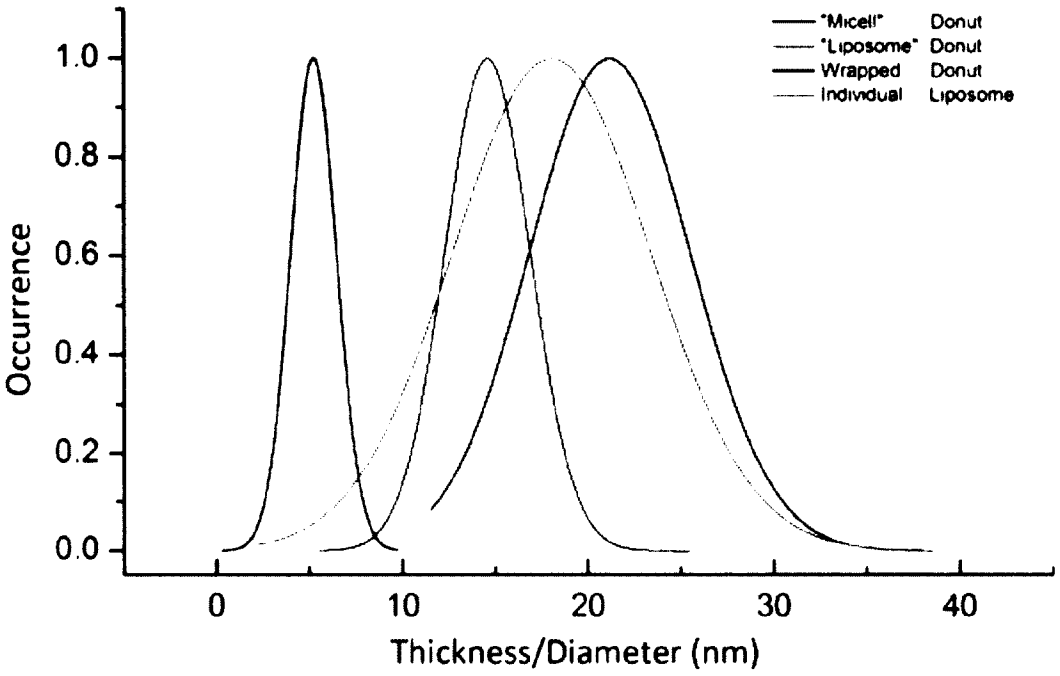


Figure 3.38 - Plot of the lipid thickness and diameter of the 4 intermediates identified during dialysis.

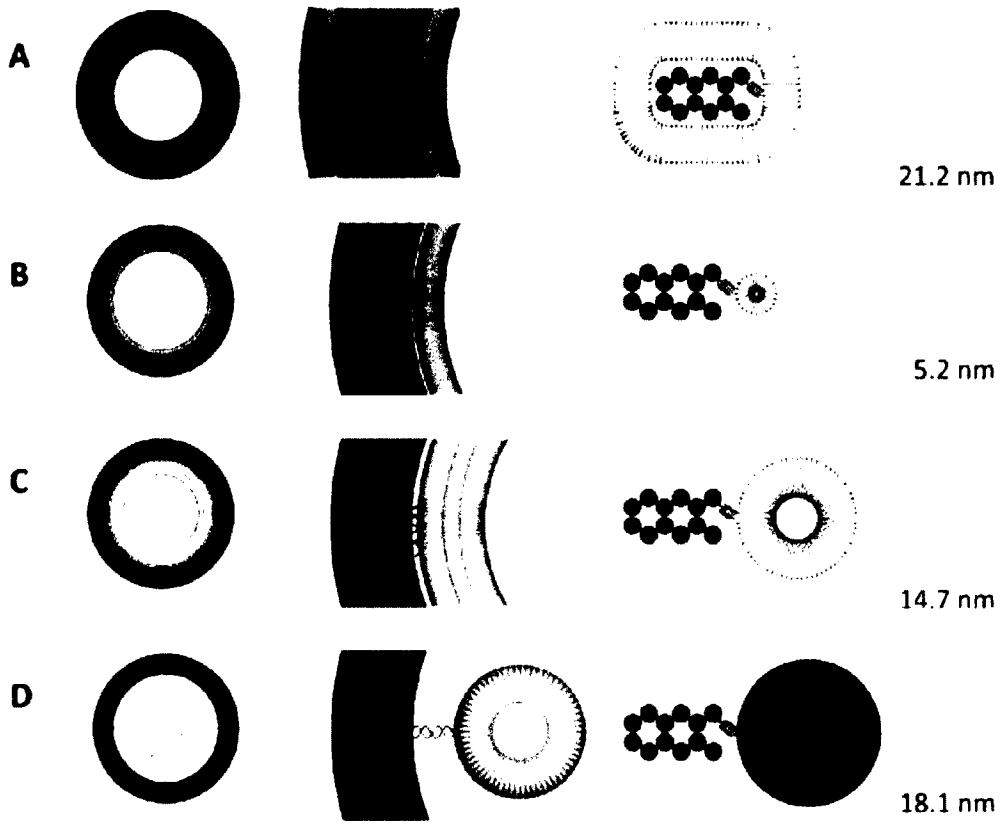


Figure 3.39 - Various views, cross section, and measured lipid thickness and diameter of the four templated intermediates.


Figure 3.40 – SDS agarose gel displaying the complete formation of the DNA origami rings and its clean separation from excess free staple strands.

| Name | Scaffold | Used length | Bundle Number | $Mg^{2+}$ requirement | Gradient purification speed and time |
|---|---|---|---|---|---|
| 29 nm-Ring | 7308 mer | 2016 bases | 6 | 10 mM | 50 krpm x 90 min |
| 46 nm-Ring | 3024 mer | 3024 bases | 6 | 10 mM | 50 krpm x 90 min |
| 60 nm-Ring | 8064 mer | 8064 bases | 12 | 12 mM | 50 krpm x 60 min |
| 94 nm-Ring | 7560 mer | 7560 bases | 10 | 10 mM | 50 krpm x 40 min |

Table 3.1 - Assembly table of various parameters for 29nm, 46nm, 60nm, and 94 nm DNA origami ring.

## Chapter 4 - Future Perspectives and Expansion of Technology:

Two models of the Saturn templating mechanism were initially proposed: 1) the Grab and Dunk model and 2) the Nucleation model, as shown in figure 4.1. It wasn't certain at the time whether, during dialysis, liposomes formed independent of lipid anchors on the DNA ring or whether they nucleated around the anchors first as micelles and then during detergent removal grew in size. We have successfully captured and presented three key intermediates during a time course study of dialysis. At 0 hr, detergent-lipid micelles are accumulating around the lipid anchor molecules and by 0.5 hr, the micelles still exist but wrap around the DNA origami ring in different ways. The critical observation here is that the detergent concentration lowering lead to a change in the micelle composition that differs from the one at 0 hr. After 1 hr of dialysis, the first signs of vesicle formation were observed. And the fact that we observed lipidic intermediate structures around the DNA ring at early times of dialysis indicate that the origami ring and the lipid anchors play a key role in initiating and stimulating micelle to vesicle formation. With the results presented in this thesis, we are confident to say that the nucleation model is the governing mechanism.

In chapter 2, we have successfully developed a method for manufacturing templated vesicles with a uniform size in high yield and purity. The Saturn structure has opened a new avenue in controlling size,

shape, and content incorporated of a liposome by the DNA Origami template. Furthermore, rotational positioning has been explored to study its effect on templating vesicles. We have reported 4 different geometries and a critical angle between 60° and 120° has been identified for templating liposome formation. However, the angled handle-ring system has been explored only in the extent of negative stain EM. A 2D capture of the structures can provide only a limited view and understanding. Thus, to study the morphology of our angled vesicles, Cryo-electron microscopy was used because it can provide more information than conventional negative stain EM. Cryo-EM does not require chemical staining procedures and the products are immediately added to an EM grid, vitrified, and visualized. To preserve our structures in near atomic resolution with water transforming to a glassy state in lieu of ice crystals, vitrification is the cryo-fixation process [113]. This method in turn delivers samples in a near native state [114, 115], while providing 3D tomographic data and allowing spatial visualization of more multifaceted assemblies. Taking this method into consideration and use, it would be incredible to capture the vesicles templated from angled handled origami rings in 3D.

Although, we have only explored the templating effects using maleimide-PE lipid anchors, it is certainly possible to couple protein anchors to the anti handles as well. We could selectively place content in DNA origami ring-liposomes and can link different anchors onto the DNA ring. Further, we

can precisely choose the position of the anchors. The number of proteins per vesicle can be tightly controlled and this parameter is useful in testing membrane fusion efficiency.

Intracellular trafficking and fusion require a conserved group of membrane-anchored proteins called SNAREs. These proteins zipper into a"trans" structure, forming a coil coil bundle to draw membranes into close proximity for fusion [116]. In the past, it has been presented using a multi-step kinetic model that 3-9 SNARE complexes are required for fusion [117]. Further, using SNARE density approaches, Dr. Erdem Karatekin reported that 5-11 SNARE complexes are required [118]. Lastly, it has also been show that as little as a single SNARE is required for fusion [119]. Despite the numerous papers published on this regard, the golden question still stands: how many SNARE complexes are required for fusion? Certainly the varying experimental parameters such as membrane curvature and lipid composition are contributing to these varying numbers. To overcome many of the previous difficulties in vesicle design and protein reconstitution control, our DNA origami ring can be a tremendously useful machinery. In parallel to our research, our collaborator Dr. Weiming Xu has successfully used our DNA origami rings to template SUVs while rigorously controlling the v-SNAREs. She then proceeded to use flow cell chambers and total internal reflection fluorescence microscopy (TIRF) to monitor single molecule fusion events, which will ultimately answer the critical question, how many pairs of

SNAREs are required for fast membrane fusion and its relation to the fusion pore size. She further addresses the question of how fast a docked vesicle can fuse with only one SNARE complex. For the first time, it is discovered that fast-fusion (in ms) is driven by no more than 2-4 pairs of SNARE complexes on single event level.

In chapter 3, we elucidated the mechanism of formation of our Saturn structures by capturing key intermediates during detergent removal dialysis. This understanding will prove momentous in the future if membranes of other shapes and sizes were to be templated by a non-ring system with varying curvature. In eukaryotic cells, the closed portions within the cytosol are cellular compartments: chloroplasts, peroxisomes, mitochondria, endoplasmic reticulum, and the nucleus all of varying size and shape. In addition to vesicles, microtubules are also accepted as compartments. These all have many roles including creating a physical boundary to separate cargo from the surrounding environment. In doing so, they must contain membrane proteins. These proteins can be extracted and need to be further studied in artificial membrane systems that is distinct in its own physical appearance. In this case, a unique DNA origami structure and its templated membrane will need to be designed and our method allows for those.

Our blue print for life is founded in DNA's basic genetic code. However DNA origami has taken the code to a new level by controlling precisely the

location of materials and dictating the mechanistic pathways. DNA origami, structurally has overcome an abundance of barriers since it was first conceived. We have reached tremendous levels of control in determining the location of functional molecules on DNA origami structures. Of course, without being too greedy, the field will always demand greater spatial positioning and scaffolding opportunities, so that the development of 3D DNA origami can reach levels of function including encapsulation of a guest proteins, enzymes, and metallic nanoparticles. Even more creative is the use of hollow 3D DNA structures as cages to house proteins of interest for crystallization for structure study and for transport of cargo. Or we could attempt to place polymers inside of the shape such as acrylamide or bisacrylamide in a liposome. If this field is married with protein engineering, new classes of artificial extracellular matrices in *ex vivo* cellular scaffolding and in tissue engineering can come to life [120, Aldaye, 2008 #140].

At the nanoscale level, after millions of years of cellular evolution, nature has finally sophisticated and complicated behavior. Structural DNA origami has already transformed into an interdisciplinary research field including scientists from material science, chemistry, computer science, biology, and physics. Into the future, we believe that the potential of this field will sky rocket in new directions far beyond the limits of that described in this thesis.

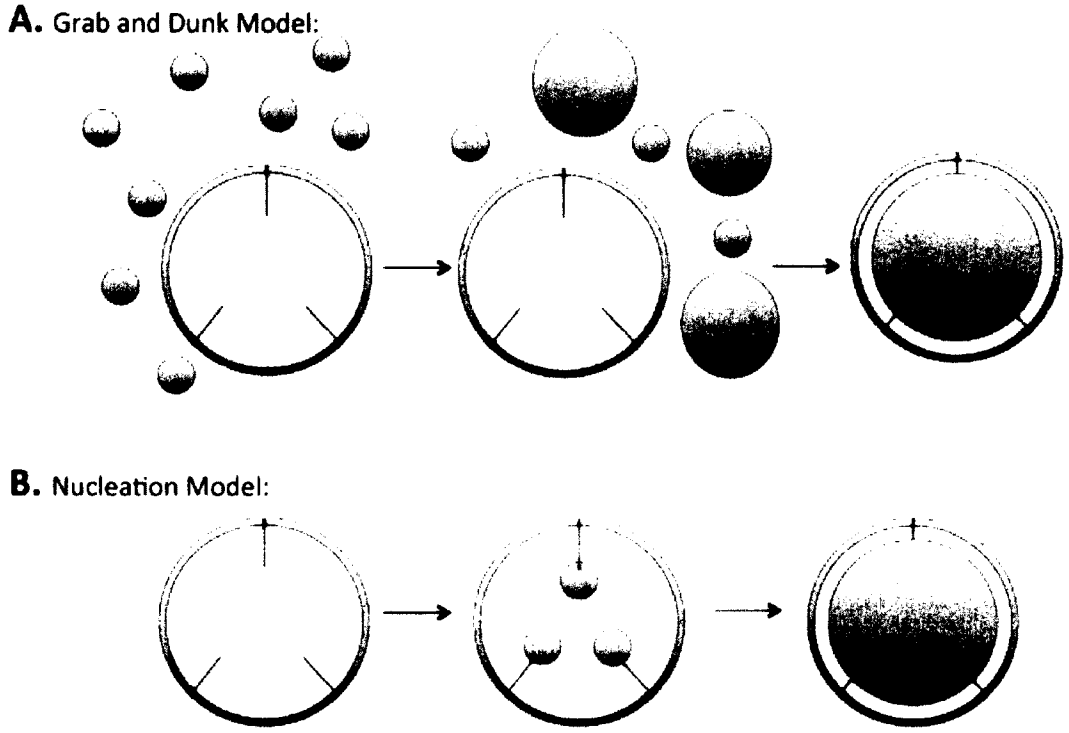


Figure 4.1 – Two proposed models for the mechanism of templated vesicles by our DNA origami rings. (A) The Grab and Drunk Model and (B) The Nucleation Model.

**References:**


1. Hogberg, B., T. Liedl, and W.M. Shih, *Folding DNA origami from a double-stranded source of scaffold.* J Am Chem Soc, 2009. **131**(26): p. 9154-5.
2. Ke, Y., et al., *Multilayer DNA origami packed on a square lattice.* J Am Chem Soc, 2009. **131**(43): p. 15903-8.
3. Whitesides, G.M., J.P. Mathias, and C.T. Seto, *Molecular self-assembly and nanochemistry: a chemical strategy for the synthesis of nanostructures.* Science, 1991. **254**(5036): p. 1312-9.
4. Seeman, N.C., *Nucleic acid junctions and lattices.* J Theor Biol, 1982. **99**(2): p. 237-47.
5. Seeman, N.C., *DNA in a material world.* Nature, 2003. **421**(6921): p. 427-31.
6. Wickner, W. and R. Schekman, *Membrane fusion.* Nat Struct Mol Biol, 2008. **15**(7): p. 658-64.
7. Marsden, H.R. and A. Kros, *Self-Assembly of Coiled Coils in Synthetic Biology: Inspiration and Progress.* Angewandte Chemie-International Edition, 2010. **49**(17): p. 2988-3005.
8. Chernomordik, L.V. and M.M. Kozlov, *Mechanics of membrane fusion.* Nat Struct Mol Biol, 2008. **15**(7): p. 675-83.
9. Marsden, H.R., I. Tomatsu, and A. Kros, *Model systems for membrane fusion.* Chem Soc Rev, 2011. **40**(3): p. 1572-85.
10. Chernomordik, L.V. and M.M. Kozlov, *Protein-lipid interplay in fusion and fission of biological membranes.* Annu Rev Biochem, 2003. **72**: p. 175-207.
11. Lentz, B.R., et al., *Protein machines and lipid assemblies: current views of cell membrane fusion.* Curr Opin Struct Biol, 2000. **10**(5): p. 607-15.
12. Jackson, M.B. and E.R. Chapman, *The fusion pores of Ca2+ -triggered exocytosis.* Nat Struct Mol Biol, 2008. **15**(7): p. 684-9.
13. Chanturiya, A., L.V. Chernomordik, and J. Zimmerberg, *Flickering fusion pores comparable with initial exocytotic pores occur in protein-free phospholipid bilayers.* Proc Natl Acad Sci U S A, 1997. **94**(26): p. 14423-8.
14. Chernomordik, L.V., G.B. Melikyan, and Y.A. Chizmadzhev, *Biomembrane fusion: a new concept derived from model studies using two interacting planar lipid bilayers.* Biochim Biophys Acta, 1987. **906**(3): p. 309-52.
15. Yang, L. and H.W. Huang, *A rhombohedral phase of lipid containing a membrane fusion intermediate structure.* Biophys J, 2003. **84**(3): p. 1808-17.
16. Malinin, V.S., P. Frederik, and B.R. Lentz, *Osmotic and curvature stress affect PEG-induced fusion of lipid vesicles but not mixing of their lipids.* Biophys J, 2002. **82**(4): p. 2090-100.
17. Cohen, F.S., J. Zimmerberg, and A. Finkelstein, *Fusion of phospholipid vesicles with planar phospholipid bilayer membranes. II. Incorporation*

*of a vesicular membrane marker into the planar membrane.* J Gen Physiol, 1980. **75**(3): p. 251-70.
18. Link, E., et al., *Tetanus toxin action: inhibition of neurotransmitter release linked to synaptobrevin proteolysis.* Biochem Biophys Res Commun, 1992. **189**(2): p. 1017-23.
19. Schiavo, G., et al., *Tetanus and botulinum-B neurotoxins block neurotransmitter release by proteolytic cleavage of synaptobrevin.* Nature, 1992. **359**(6398): p. 832-5.
20. Blasi, J., et al., *Botulinum neurotoxin A selectively cleaves the synaptic protein SNAP-25.* Nature, 1993. **365**(6442): p. 160-3.
21. Blasi, J., et al., *Botulinum neurotoxin C1 blocks neurotransmitter release by means of cleaving HPC-1/syntaxin.* EMBO J, 1993. **12**(12): p. 4821-8.
22. Brenner, S., *The genetics of Caenorhabditis elegans.* Genetics, 1974. **77**(1): p. 71-94.
23. Novick, P., C. Field, and R. Schekman, *Identification of 23 complementation groups required for post-translational events in the yeast secretory pathway.* Cell, 1980. **21**(1): p. 205-15.
24. Wilson, D.W., et al., *A fusion protein required for vesicle-mediated transport in both mammalian cells and yeast.* Nature, 1989. **339**(6223): p. 355-9.
25. Sollner, T., et al., *A protein assembly-disassembly pathway in vitro that may correspond to sequential steps of synaptic vesicle docking, activation, and fusion.* Cell, 1993. **75**(3): p. 409-18.
26. Hayashi, T., et al., *Synaptic vesicle membrane fusion complex: action of clostridial neurotoxins on assembly.* EMBO J, 1994. **13**(21): p. 5051-61.
27. Hanson, P.I., et al., *Structure and conformational changes in NSF and its membrane receptor complexes visualized by quick-freeze/deep-etch electron microscopy.* Cell, 1997. **90**(3): p. 523-35.
28. Mayer, A., W. Wickner, and A. Haas, *Sec18p (NSF)-driven release of Sec17p (alpha-SNAP) can precede docking and fusion of yeast vacuoles.* Cell, 1996. **85**(1): p. 83-94.
29. Poirier, M.A., et al., *The synaptic SNARE complex is a parallel four-stranded helical bundle.* Nat Struct Biol, 1998. **5**(9): p. 765-9.
30. Sutton, R.B., et al., *Crystal structure of a SNARE complex involved in synaptic exocytosis at 2.4 A resolution.* Nature, 1998. **395**(6700): p. 347-53.
31. Eytan, G.D., *Use of liposomes for reconstitution of biological functions.* Biochim Biophys Acta, 1982. **694**(2): p. 185-202.
32. Racker, E., *Reconstitution of membrane processes.* Methods Enzymol, 1979. **55**: p. 699-711.
33. Rigaud, J.L., B. Pitard, and D. Levy, *Reconstitution of membrane proteins into liposomes: application to energy-transducing membrane proteins.* Biochim Biophys Acta, 1995. **1231**(3): p. 223-46.
34. Kuhlbrandt, W., *Two-dimensional crystallization of membrane proteins.* Q Rev Biophys, 1992. **25**(1): p. 1-49.
35. Rigaud, J., et al., *Use of detergents in two-dimensional crystallization of*

*membrane proteins.* Biochim Biophys Acta, 2000. **1508**(1-2): p. 112-28.
36. Szoka, F., Jr. and D. Papahadjopoulos, *Comparative properties and methods of preparation of lipid vesicles (liposomes).* Annu Rev Biophys Bioeng, 1980. **9**: p. 467-508.
37. Deamer, D. and A.D. Bangham, *Large volume liposomes by an ether vaporization method.* Biochim Biophys Acta, 1976. **443**(3): p. 629-34.
38. Szoka, F., Jr. and D. Papahadjopoulos, *Procedure for preparation of liposomes with large internal aqueous space and high capture by reverse-phase evaporation.* Proc Natl Acad Sci U S A, 1978. **75**(9): p. 4194-8.
39. Darszon, A., et al., *Incorporation of membrane proteins into large single bilayer vesicles. Application to rhodopsin.* J Cell Biol, 1979. **81**(2): p. 446-52.
40. Rigaud, J.L., A. Bluzat, and S. Buschlen, *Incorporation of bacteriorhodopsin into large unilamellar liposomes by reverse phase evaporation.* Biochem Biophys Res Commun, 1983. **111**(2): p. 373-82.
41. le Maire, M., P. Champeil, and J.V. Moller, *Interaction of membrane proteins and lipids with solubilizing detergents.* Biochim Biophys Acta, 2000. **1508**(1-2): p. 86-111.
42. Lasic, D.D., *The mechanism of vesicle formation.* Biochem J, 1988. **256**(1): p. 1-11.
43. Vinson, P.K., Y. Talmon, and A. Walter, *Vesicle-micelle transition of phosphatidylcholine and octyl glucoside elucidated by cryo-transmission electron microscopy.* Biophys J, 1989. **56**(4): p. 669-81.
44. Walter, A., et al., *Intermediate structures in the cholate-phosphatidylcholine vesicle-micelle transition.* Biophys J, 1991. **60**(6): p. 1315-25.
45. Lambert, O., et al., *A new "gel-like" phase in dodecyl maltoside-lipid mixtures: implications in solubilization and reconstitution studies.* Biophys J, 1998. **74**(2 Pt 1): p. 918-30.
46. Helenius, A., M. Sarvas, and K. Simons, *Asymmetric and symmetric membrane reconstitution by detergent elimination. Studies with Semliki-Forest-virus spike glycoprotein and penicillinase from the membrane of Bacillus licheniformis.* Eur J Biochem, 1981. **116**(1): p. 27-35.
47. Allen, T.M., et al., *Detergent removal during membrane reconstitution.* Biochim Biophys Acta, 1980. **601**(2): p. 328-42.
48. Philippot, J.R., S. Mutaftschiev, and J.P. Liautard, *Extemporaneous preparation of large unilamellar liposomes.* Biochim Biophys Acta, 1985. **821**(1): p. 79-84.
49. Rigaud, J.L. and D. Levy, *Reconstitution of membrane proteins into liposomes.* Methods Enzymol, 2003. **372**: p. 65-86.
50. Levy, D., et al., *A systematic study of liposome and proteoliposome reconstitution involving Bio-Bead-mediated Triton X-100 removal.* Biochim Biophys Acta, 1990. **1025**(2): p. 179-90.

51. Rigaud, J.L., et al., *Bio-Beads: an efficient strategy for two-dimensional crystallization of membrane proteins.* J Struct Biol, 1997. **118**(3): p. 226-35.
52. Abeywardena, M.Y., T.M. Allen, and J.S. Charnock, *Lipid-protein interactions of reconstituted membrane-associated adenosinetriphosphatases. Use of a gel-filtration procedure to examine phospholipid-activity relationships.* Biochim Biophys Acta, 1983. **729**(1): p. 62-74.
53. Racker, E., T.F. Chien, and A. Kandrach, *A cholate-dilution procedure for the reconstitution of the Ca++ pump, 32Pi--ATP exchange, and oxidative phosphorylation.* FEBS Lett, 1975. **57**(1): p. 14-8.
54. Racker, E., et al., *Reconstitution, a way of biochemical research; some new approaches to membrane-bound enzymes.* Arch Biochem Biophys, 1979. **198**(2): p. 470-7.
55. Paternostre, M.T., M. Roux, and J.L. Rigaud, *Mechanisms of membrane protein insertion into liposomes during reconstitution procedures involving the use of detergents. 1. Solubilization of large unilamellar liposomes (prepared by reverse-phase evaporation) by triton X-100, octyl glucoside, and sodium cholate.* Biochemistry, 1988. **27**(8): p. 2668-77.
56. Levy, D., et al., *Phospholipid vesicle solubilization and reconstitution by detergents. Symmetrical analysis of the two processes using octaethylene glycol mono-n-dodecyl ether.* Biochemistry, 1990. **29**(40): p. 9480-8.
57. Rigaud, J.L., M.T. Paternostre, and A. Bluzat, *Mechanisms of membrane protein insertion into liposomes during reconstitution procedures involving the use of detergents. 2. Incorporation of the light-driven proton pump bacteriorhodopsin.* Biochemistry, 1988. **27**(8): p. 2677-88.
58. Cladera, J., et al., *Liposome solubilization and membrane protein reconstitution using Chaps and Chapso.* Eur J Biochem, 1997. **243**(3): p. 798-804.
59. Levy, D., et al., *Reconstitution of the sarcoplasmic reticulum Ca(2+)-ATPase: mechanisms of membrane protein insertion into liposomes during reconstitution procedures involving the use of detergents.* Biochim Biophys Acta, 1992. **1107**(2): p. 283-98.
60. Pitard, B., et al., *ATP synthesis by the F0F1 ATP synthase from thermophilic Bacillus PS3 reconstituted into liposomes with bacteriorhodopsin. 1. Factors defining the optimal reconstitution of ATP synthases with bacteriorhodopsin.* Eur J Biochem, 1996. **235**(3): p. 769-78.
61. Brown, R.E., *Sphingolipid organization in biomembranes: what physical studies of model membranes reveal.* J Cell Sci, 1998. **111 ( Pt 1)**: p. 1-9.
62. Seeman, N.C., *Nanomaterials based on DNA.* Annu Rev Biochem, 2010. **79**: p. 65-87.
63. Qiu, H., J.C. Dewan, and N.C. Seeman, *A DNA decamer with a sticky end:*

*the crystal structure of d-CGACGATCGT.* J Mol Biol, 1997. **267**(4): p. 881-98.
64. Chen, J.H. and N.C. Seeman, *Synthesis from DNA of a molecule with the connectivity of a cube.* Nature, 1991. **350**(6319): p. 631-3.
65. Zhang, Y.W. and N.C. Seeman, *Construction of a DNA-Truncated Octahedron.* Journal of the American Chemical Society, 1994. **116**(5): p. 1661-1669.
66. Liu, Y., et al., *Aptamer-directed self-assembly of protein arrays on a DNA nanostructure.* Angew Chem Int Ed Engl, 2005. **44**(28): p. 4333-8.
67. Lin, C., et al., *DNA tile based self-assembly: building complex nanoarchitectures.* Chemphyschem, 2006. **7**(8): p. 1641-7.
68. Yan, H., et al., *DNA-templated self-assembly of protein arrays and highly conductive nanowires.* Science, 2003. **301**(5641): p. 1882-4.
69. Loweth, C.J., et al., *DNA-based assembly of gold nanocrystals.* Angewandte Chemie-International Edition, 1999. **38**(12): p. 1808-1812.
70. Deng, Z.X., et al., *DNA-encoded self-assembly of gold nanoparticles into one-dimensional arrays.* Angewandte Chemie-International Edition, 2005. **44**(23): p. 3582-3585.
71. Sharma, J., et al., *DNA-tile-directed self-assembly of quantum dots into two-dimensional nanopatterns.* Angewandte Chemie-International Edition, 2008. **47**(28): p. 5157-5159.
72. Rothemund, P.W., *Folding DNA to create nanoscale shapes and patterns.* Nature, 2006. **440**(7082): p. 297-302.
73. Andersen, E.S., et al., *Self-assembly of a nanoscale DNA box with a controllable lid.* Nature, 2009. **459**(7243): p. 73-6.
74. Ke, Y., et al., *Scaffolded DNA origami of a DNA tetrahedron molecular container.* Nano Lett, 2009. **9**(6): p. 2445-7.
75. Kuzuya, A. and M. Komiyama, *Design and construction of a box-shaped 3D-DNA origami.* Chem Commun (Camb), 2009(28): p. 4182-4.
76. Endo, M., et al., *DNA prism structures constructed by folding of multiple rectangular arms.* J Am Chem Soc, 2009. **131**(43): p. 15570-1.
77. Douglas, S.M., et al., *Self-assembly of DNA into nanoscale three-dimensional shapes.* Nature, 2009. **459**(7245): p. 414-8.
78. Dietz, H., S.M. Douglas, and W.M. Shih, *Folding DNA into twisted and curved nanoscale shapes.* Science, 2009. **325**(5941): p. 725-30.
79. Han, D., et al., *DNA origami with complex curvatures in three-dimensional space.* Science, 2011. **332**(6027): p. 342-6.
80. Ke, Y., et al., *Self-assembled water-soluble nucleic acid probe tiles for label-free RNA hybridization assays.* Science, 2008. **319**(5860): p. 180-3.
81. Subramanian, H.K.K., et al., *The Label-Free Unambiguous Detection and Symbolic Display of Single Nucleotide Polymorphisms on DNA Origami.* Nano Letters, 2011. **11**(2): p. 910-913.
82. Chhabra, R., et al., *Spatially addressable multiprotein nanoarrays templated by aptamer-tagged DNA nanoarchitectures.* Journal of the

American Chemical Society, 2007. **129**(34): p. 10304-+.
83. Rinker, S., et al., *Self-assembled DNA nanostructures for distance-dependent multivalent ligand-protein binding.* Nature Nanotechnology, 2008. **3**(7): p. 418-422.
84. Pal, S., et al., *DNA-Origami-Directed Self-Assembly of Discrete Silver-Nanoparticle Architectures.* Angewandte Chemie-International Edition, 2010. **49**(15): p. 2700-2704.
85. Sharma, J., et al., *Toward reliable gold nanoparticle patterning on self-assembled DNA nanoscaffold.* Journal of the American Chemical Society, 2008. **130**(25): p. 7820-+.
86. Ding, B.Q., et al., *Gold Nanoparticle Self-Similar Chain Structure Organized by DNA Origami.* Journal of the American Chemical Society, 2010. **132**(10): p. 3248-+.
87. Stearns, L.A., et al., *Template-Directed Nucleation and Growth of Inorganic Nanoparticles on DNA Scaffolds.* Angewandte Chemie-International Edition, 2009. **48**(45): p. 8494-8496.
88. Zhao, Z., et al., *Encapsulation of Gold Nanoparticles in a DNA Origami Cage.* Angewandte Chemie-International Edition, 2011. **50**(9): p. 2041-2044.
89. Maune, H.T., et al., *Self-assembly of carbon nanotubes into two-dimensional geometries using DNA origami templates.* Nature Nanotechnology, 2010. **5**(1): p. 61-66.
90. Liu, H.J., et al., *DNA-Templated Covalent Coupling of G4 PAMAM Dendrimers.* Journal of the American Chemical Society, 2010. **132**(51): p. 18054-18056.
91. Stephanopoulos, N., et al., *Immobilization and one-dimensional arrangement of virus capsids with nanoscale precision using DNA origami.* Nano Lett, 2010. **10**(7): p. 2714-20.
92. Kuzyk, A., K.T. Laitinen, and P. Torma, *DNA origami as a nanoscale template for protein assembly.* Nanotechnology, 2009. **20**(23): p. 235305.
93. Kuzuya, A., et al., *Precisely programmed and robust 2D streptavidin nanoarrays by using periodical nanometer-scale wells embedded in DNA origami assembly.* Chembiochem, 2009. **10**(11): p. 1811-5.
94. Numajiri, K., et al., *Stepwise and reversible nanopatterning of proteins on a DNA origami scaffold.* Chem Commun (Camb), 2010. **46**(28): p. 5127-9.
95. Shen, W., et al., *NTA directed protein nanopatterning on DNA Origami nanoconstructs.* J Am Chem Soc, 2009. **131**(19): p. 6660-1.
96. Hung, A.M., et al., *Large-area spatially ordered arrays of gold nanoparticles directed by lithographically confined DNA origami.* Nat Nanotechnol, 2010. **5**(2): p. 121-6.
97. Kershner, R.J., et al., *Placement and orientation of individual DNA shapes on lithographically patterned surfaces.* Nat Nanotechnol, 2009. **4**(9): p. 557-61.
98. Ding, B., et al., *Interconnecting gold islands with DNA origami*

*nanotubes.* Nano Lett, 2010. **10**(12): p. 5065-9.
99. Gerdon, A.E., et al., *Controlled delivery of DNA origami on patterned surfaces.* Small, 2009. **5**(17): p. 1942-6.
100. Voigt, N.V., et al., *Single-molecule chemical reactions on DNA origami.* Nat Nanotechnol, 2010. **5**(3): p. 200-3.
101. Winfree, E., et al., *Design and self-assembly of two-dimensional DNA crystals.* Nature, 1998. **394**(6693): p. 539-44.
102. Shen, Z., et al., *Paranemic crossover DNA: a generalized Holliday structure with applications in nanotechnology.* J Am Chem Soc, 2004. **126**(6): p. 1666-74.
103. Aldaye, F.A., A.L. Palmer, and H.F. Sleiman, *Assembling materials with DNA as the guide.* Science, 2008. **321**(5897): p. 1795-9.
104. Pinheiro, A.V., et al., *Challenges and opportunities for structural DNA nanotechnology.* Nat Nanotechnol, 2011. **6**(12): p. 763-72.
105. Torring, T., et al., *DNA origami: a quantum leap for self-assembly of complex structures.* Chem Soc Rev, 2011. **40**(12): p. 5636-46.
106. Rothemund, P.W., et al., *Design and characterization of programmable DNA nanotubes.* J Am Chem Soc, 2004. **126**(50): p. 16344-52.
107. Fu, T.J. and N.C. Seeman, *DNA double-crossover molecules.* Biochemistry, 1993. **32**(13): p. 3211-20.
108. Davies, I.G., J.M. Graham, and B.A. Griffin, *Rapid separation of LDL subclasses by iodixanol gradient ultracentrifugation.* Clin Chem, 2003. **49**(11): p. 1865-72.
109. Graham, J.M., et al., *A novel method for the rapid separation of plasma lipoproteins using self-generating gradients of iodixanol.* Atherosclerosis, 1996. **124**(1): p. 125-35.
110. Sawle, A., et al., *A rapid single-step centrifugation method for determination of HDL, LDL, and VLDL cholesterol, and TG, and identification of predominant LDL subclass.* J Lipid Res, 2002. **43**(2): p. 335-43.
111. Havel, R.J., H.A. Eder, and J.H. Bragdon, *The distribution and chemical composition of ultracentrifugally separated lipoproteins in human serum.* J Clin Invest, 1955. **34**(9): p. 1345-53.
112. Wilcox, H.G., D.C. Davis, and M. Heimberg, *The isolation of lipoproteins from human plasma by ultracentrifugation in zonal rotors.* J Lipid Res, 1971. **12**(2): p. 160-72.
113. Grigorieff, N. and S.C. Harrison, *Near-atomic resolution reconstructions of icosahedral viruses from electron cryo-microscopy.* Curr Opin Struct Biol, 2011. **21**(2): p. 265-73.
114. Koning, R.I. and A.J. Koster, *Cryo-electron tomography in biology and medicine.* Ann Anat, 2009. **191**(5): p. 427-45.
115. Tatischeff, I., et al., *Fast characterisation of cell-derived extracellular vesicles by nanoparticles tracking analysis, cryo-electron microscopy, and Raman tweezers microspectroscopy.* J Extracell Vesicles, 2012. **1**.
116. Jahn, R. and R.H. Scheller, *SNAREs--engines for membrane fusion.* Nat Rev Mol Cell Biol, 2006. **7**(9): p. 631-43.

117. Domanska, M.K., et al., *Single vesicle millisecond fusion kinetics reveals number of SNARE complexes optimal for fast SNARE-mediated membrane fusion.* J Biol Chem, 2009. **284**(46): p. 32158-66.
118. Karatekin, E., et al., *A fast, single-vesicle fusion assay mimics physiological SNARE requirements.* Proc Natl Acad Sci U S A, 2010. **107**(8): p. 3517-21.
119. van den Bogaart, G., et al., *One SNARE complex is sufficient for membrane fusion.* Nat Struct Mol Biol, 2010. **17**(3): p. 358-64.
120. Aldaye, F.A., et al., *A structurally tunable DNA-based extracellular matrix.* J Am Chem Soc, 2010. **132**(42): p. 14727-9.
121. Sudhof, T.C. and J. Rizo, *Synaptice vesicle exocytosis.* Cold Spring Harb Perspect Biol, 2011 **3**(12): p. 1-14.
122. Kuzuya, A. and M. Komiyama, *DNA origami; Fold, stick, and beyond.* Nanoscale, 2009 **2**: p. 310-322.